An Investigation of Medium Effects on the One and Two-Dimensional Electronic Spectroscopy of Chlorophyll a

By Roberta Moca

A thesis submitted in conformity with the requirements for the degree of Master of Research Graduate Department of Chemistry, University of East Anglia (2015)

Abstract

The study of the photosynthetic processes has always had a particular relevance in spectroscopy because of its possible applications in light harvesting and energy storage. Since the light-harvesting pigment-protein complexes have this functional role in nature, many of studies have been focused on understanding photophysical processes occurring in these systems. Our work aims to study the spectroscopic properties of the best known pigment involved in the photosynthesis, Chlorophyll a, and their changes with different solvents. The study of the pigment was conducted by linear spectroscopic studies for water-solvent mixtures, while by the nonlinear technique 2D spectroscopy was applied for pure solvent. The theory and technique of 2D spectroscopy is described. The properties of solvents strongly influence the environment felt by the molecule and its capability of aggregate formation. The solvent properties that were found to be most relevant for our study were viscosity, H-bonding formation and polarity. While the first two were shown to be responsible for a persistent inhomogeneity in the 2D spectra, the kinetics of aggregate formation in water solvent mixtures were found to be influenced by the polarity and the capability of H bonding formation.

1. INTRODUCTION

This work aims to give a preliminary study of Chlorophyll aggregation through the use of linear steady state and nonlinear ultrafast spectroscopic methods. Chlorophyll has long been studied for its central role in photosynthesis, oxygen transport and biological oxidation and reduction. Here it will be studied in simpler solution phase systems, with the aim of giving us some insight into light harvesting processes occurring in photosynthesis. To achieve deep knowledge about electronic structure and dynamics, electronic spectroscopic methods are the most widely applied experimental tools.

In order to investigate the dynamics of chemical processes, it is essential to probe the system with a time-resolved spectroscopic method with a time resolution greater than the rate of the process examined (1). Dynamics with a time resolution below 10^{-11}s cannot be measured with any conventional detection electronics due to the finite time response of the detector. This problem has led to the use of spectroscopic techniques with multiple ultrashort laser pulses with variable interpulse delays, controlled by variation of the optical path length, to investigate the fastest molecular dynamics. The best known examples are flash photolysis and related pump – probe techniques. This approach allows a time resolution depending only on the laser pulse durations instead of the temporal resolution of the detecting device. In this work we go beyond the capabilities of simple pump-probe methods to exploit the additional capabilities of the recently developed two-dimensional electronic spectroscopy (2DES) (2) (3).

Such multidimensional giving have the advantage of adding information to that available from single dimensional (e.g. pump-probe) measurements, by recording a correlation map that correlates the detection frequency with the excitation frequency. This concept was first developed for nuclear magnetic resonance (NMR) experiments (4) . That apparatus was built involving electromagnetic pulses in the radiofrequency region, allowing the method to probe phenomena within the times-scales of milliseconds. In 1990 new technologies were developed to generate stable ultrafast laser pulses in the visible and IR regions. This allowed the extension of multidimensional spectroscopy to probe much faster phenomena within the timescale of femtoseconds. The methods include the ability to use 2D techniques to probe vibrational (2DIR) (5) and electronic (2DES) (6) transitions. Between these two techniques, however, 2DES has been a greater experimental challenge, as the interferometric nature of the experiment required mechanical stability better than one-tenth of a wavelength (i.e. tens of nanometers in the visible region).

2DES spectroscopy is a pump and probe technique using three pulses instead of two to get information about the system (in a similar fashion to 2D NMR). Since our studies will be conducted using this technique, it seems appropriate to mention what are the advantages that make this technique different to other pump - probe techniques. In a standard pump and probe method, the system is excited by an intense pump pulse and then interrogated with a less intense probe pulse at different time delays. 2DES spectroscopy with its map of emission as a function of excitation frequency creates a connection for each signal in the map between the value of the excitation and detection frequency; as in 2D NMR this reveals the existence of couplings between states, as cross peaks, and the pathway of relaxation over time, rather than just the rate of attaining the end point measured in pump-probe experiments. In fact, 2DES includes all the information available from more established third-order techniques such as the photo echo, transient grating, absorption and pump - probe signals. All these data can be obtained by a cut through or an integral over part of the 2DES map. Thus 2DES will be applied here to provide a new insight into the spectroscopy of chlorophyll a, and prepares the way for developing an understanding of the couplings which underlie the complex behavior in light harvesting systems.

This introduction is divided in two main parts. Section 1.1 starts by introducing the general optical properties of porphyrins, then moves to the particular molecule studied (chlorophyll a, Chl a) describing its structure and how this influences aggregation. Since the optical properties arise from the intrinsic electronic structure of the molecule, the MO model by Gouterman has been introduced to describe the π-electron system. However, we will also be interested in the spectroscopy of Chl a dimers and higher aggregates, so the optical properties of aggregates are described with a brief introduction of the exciton coupling theory (7). The last part of the introduction is devoted to illustrating the potential of 2DES spectroscopy, giving special attention to the relation between spectral features and the system dynamics.

1.1 RING AND ORBITAL STRUCTURE OF PORPHYRINS

Chlorophyll is closely related to the porphyrin ring system so, in order to better understand its properties, it is important to introduce the parent compound. The reason for this relation is the macrocycle structure that these two molecules have in common, which is responsible for their optical properties. The macrocycle has a planar structure with 20 carbons surrounding a central core of four nitrogen atoms. The configuration of the ring, with alternated single and double bonds between carbon atoms, allows an overlap of π orbitals between adjacent carbons making the electrons delocalized around the whole macrocyclic. Since planarity of the ring and the delocalization of π-electrons are criteria for aromaticity, porphyrins and its derivative macrocycles follow the Huckel's rule and have 4n+2 π-electrons delocalized over the ring.

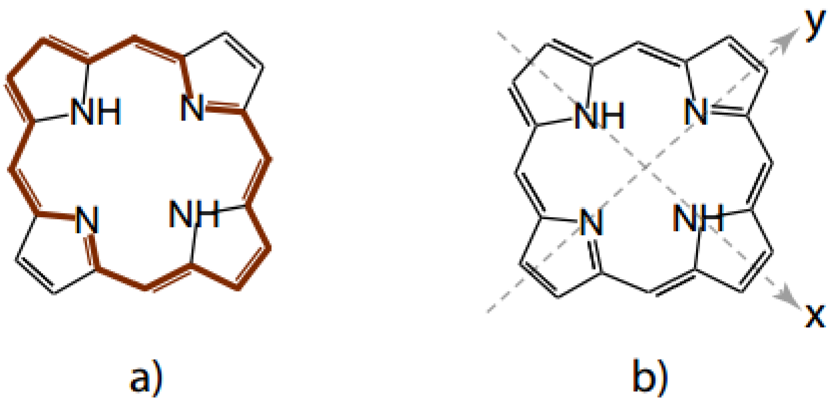

Figure 1 (8) *porphyrin macrocycle a) One delocalization pathway (In Brown) of the 18π electrons in a part of the ring called* (9) *annulene that usually occurs in porphyrins and chlorins. b) The two orthogonal symmetry axes denoted as x and y.*

The delocalization pathway highlighted in Figure1a is called annulene (9) and it shows the part of the ring over which the electrons delocalize. This consists of an 18π electron pathway and it is also found in related derivatives such as chlorins and bacteriochlorins. Recently, it was suggested that the electrons involved in the delocalization are not only included in one annulene structure but the total delocatization is given by a linear combination of all possible pathways (4n+2) (10).

The optical properties of porphyrin molecules can be explained by the four-orbital model developed by Gouterman (11) (12). Even though Gouterman's four orbitals model has some discrepancies with the more recent theory (13) (14), it gives a realistic picture of the oscillator strengths and transition energies. The model takes in account only four orbitals; the two highest occupied molecular orbitals HOMO-1, HOMO and the two lowest unoccupied molecular orbitals or LUMO and LUMO+1. These four orbitals are presented in Figure 2 where the electronic delocalization and symmetry for the porphine model are also specified.

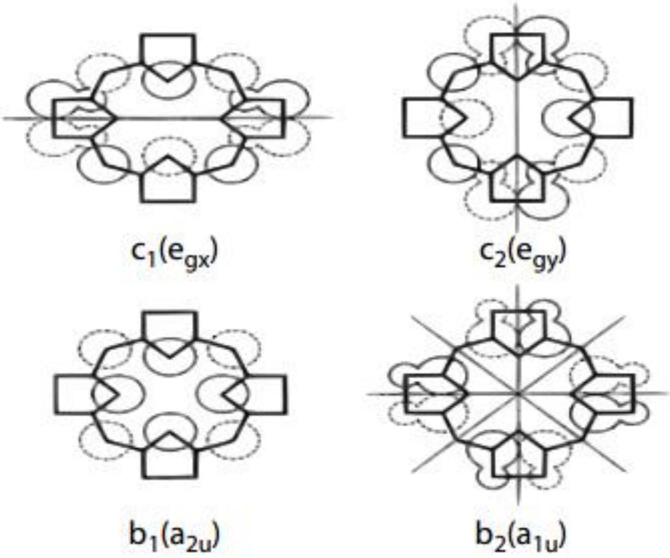

Figure 2 (15) *The picture above shows the electronic structures of the HOMO and LUMO orbitals with their corresponding symmetries. The difference of sign in the orbitals is indicated by solid or dashed line.*

Molecules that belong to the symmetry group of D_{4h}, such as metallo porphyrins, have transitions with equivalent dipoles in the *x* and *y* directions with an E_u symmetry (11). As a result of this, transitions Q_x ,Q_y and B_x, B_y are equivalent and the additional bands seen on the spectra are vibrational peaks due to the different equilibrium position between the ground state and the excited state. When the molecular symmetry becomes lower than D_{4h}, components Q_x ,Q_y and B_x, B_y become non degenerate and the bands appear split in the electronic spectra (11) (8). A decrease in symmetry in the molecule causes a change in symmetry of the HOMO and LUMO orbitals, that now belong to the b_1,b_2 and c_1,c_2 types respectively. The two LUMO orbitals have a symmetry on the *x* or *y* axes. As can be seen from the Figure 3, the symmetry of the macrocycle strongly influences the degeneracy and the energy of the orbitals (11).

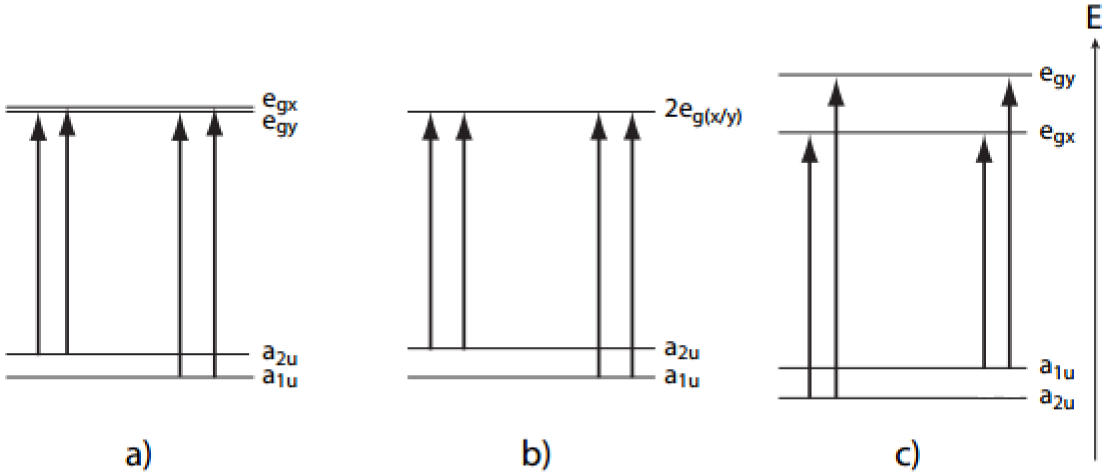

FIGURE 3 (8) *IN THE PICTURE ABOVE, HOMO AND LUMO ENERGY LEVELS ARE SHOWN FOR FREE-BASE PORPHINE (A) METALLOPORPHYRIN (B) AND CHLORON MACROCYCLE (C), RESPECTIVELY. THE ALLOWED TRANSITIONS ARE INDICATED BY ARROWS AND COME FROM THE OCCUPIED TO UNOCCUPIED ORNITALS* (16) (17).

Free bases porphine, for instance, has LUMO orbitals almost degenerate because of the lower symmetry group to which they belong (D_{2h})(Figure 3(a)). When a metal is coordinated with the ring, the symmetry of the molecule increases to D_{4h} leading to degenerate LUMO orbitals and a shift to lower energies of a_{1u} (Figure 3 (b)). The reason for this is the effect that the metal has on the orbitals that lead to the transitions. In fact, it is conjugated to the pπ orbitals with the π electrons of the ring. The metal only interacts with the a_{2u} becoming more electropositive and increasing the orbital energy. As a result there is a degeneracy of the HOMO orbitals, a red shift in the spectrum and an increase in intensity of the visible band (8) . In addition, in chlorin the removal of carbons 7 and 8 from the conjugation (see *Figure 7 for the enumeration)* affects the orbitals b_3 and c_1 that have delocalized the electron density on these positions. This lower electron delocalization and raises the energy of those orbitals (Figure 3 (c)).

1.2 OPTICAL PROPERTIES

Spectra of Chlorophylls have two strong absorption bands one located in the blue-violet and the other in the red region of the spectrum. The one in the blue-violet region is called the Soret band or B-band, whereas the other in the red region is the Q band. Both the absorption bands arise from a $\pi \rightarrow \pi^*$ transitions where π^* denotes the excited state. Moreover, transitions to the HOMO from orbitals lower than LUMO of the type $n \rightarrow \pi^*$ can also occur. This last kind of transition involves non-bonding nitrogen orbitals of pyrrole and π^* orbitals of the ring (8). However, these are more typical in Bacterioclorophyll than Chlorophylls. Porphyrins have a strong absorption in the blue region and a weak absorption in the red region. The reduction of symmetry due to the introduction of the isocyclic ring in Bchl leads to changes in the spectra such as a doubled absorption in the red region and a weak red shift (17). These effects become even more pronounced in the Chla and Chlb cases where the double bond between C-17 and C-18 carbons is reduced. Moreover, the additional reduction on the 7, 8 double bond in BChls makes the absorption sharper in the visible and in near IR region (12) (Figure 4).

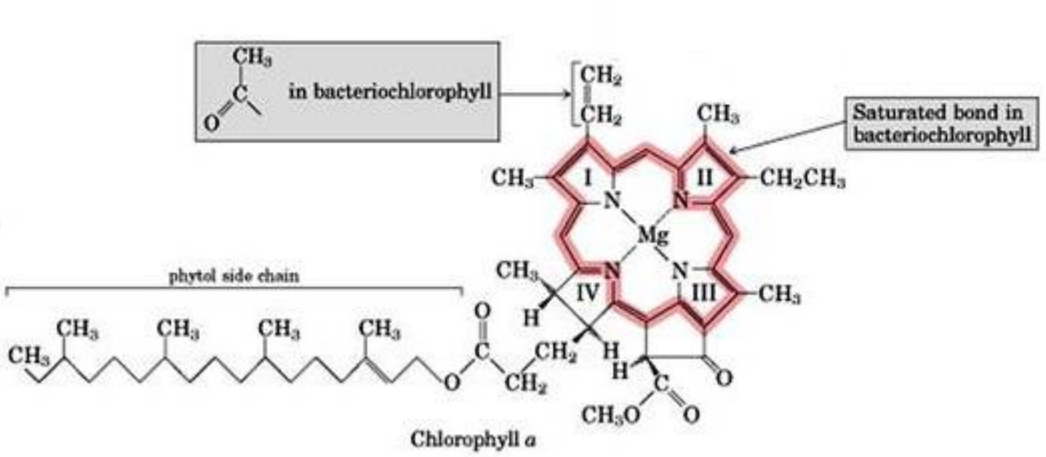

Figure 4; The figure shows the Chlorophyll a molecule comparing its structure with that of Bacteriochlorophyll. The conjugation pathway is indicated by the red color.

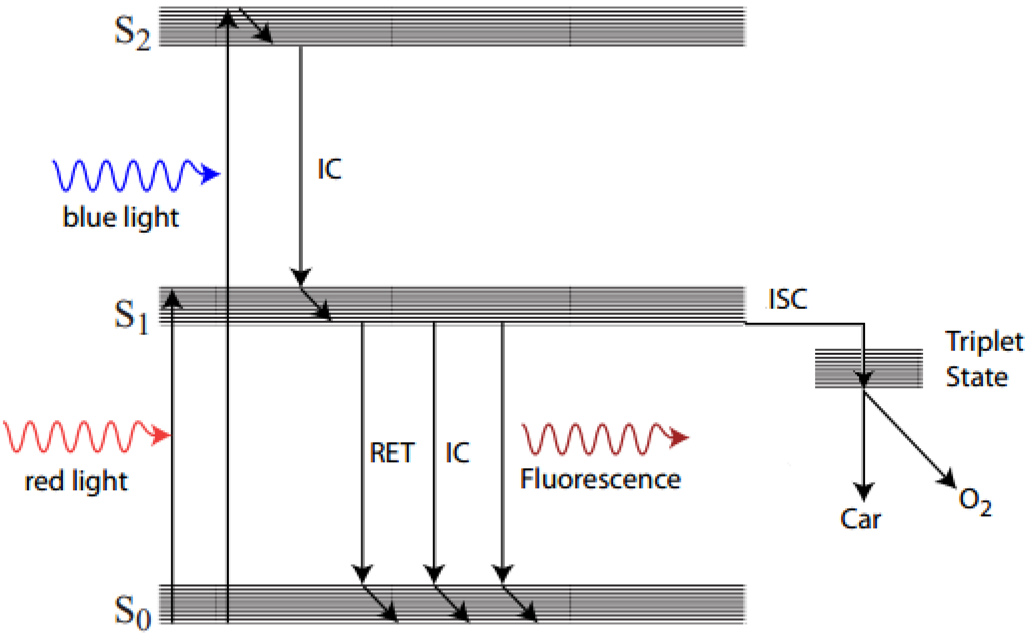

FIGURE5 (8) *THE FIGURE SHOWS THE JABLONSKI DIAGRAM FOR THE CHLOROPHYLL CASE. THE DIAGONAL ARROWS INDICATE VIBRATIONAL RELAXATION AND COOLING. THE ENERGY IN THE TRIPLET STATE CAN BE DAMAGING IN PHOTOSYNTHETIC SYSTEMS VIA TRANSFER TO GENERATE SINGLET OXYGEN. THIS IS COMBATTED BY COMPETING TRANSFER TO CAROTENOIDS (CAR), WHOSE ROLE IS DISSIPATING THAT ENERGY.*

The figure above shows the energy level structure for Chlorophyll and its possible ways to absorb and emit energy. The two dominant transitions are $S_0 \rightarrow S_2$ and $S_0 \rightarrow S_1$ that refer to the Soret and Q band, respectively. The system can dissipate energy through non radiative processes that involve states with the same multiplicity such as vibrational relaxation (VR, no change of electronic state) and internal conversion (IC, relaxation to a lower state of the same multiplicity) or move into a triplet state via intersystem crossing (ISC). This triplet state can produce oxygen in a reactive (singlet) form by energy transfer. Chlorophyll molecules in the S_1 state can return to the ground state through fluorescence or transferring energy to another molecule by fluorescence resonant energy transfer (FRET). The transition most relevant in the photosynthesis process is the one between S_0-S_1 levels, because it is responsible for light harvesting in the photosynthetic systems PSII (680nm) and PSI (700nm) (8).

1.3 CHLOROPHYLL STRUCTURE

As a porphyrins’ family member, Chlorophylls are characterized by an aromatic heterocyclic ring formed by four pyrrole molecules connected together with methine bridges (=C-).

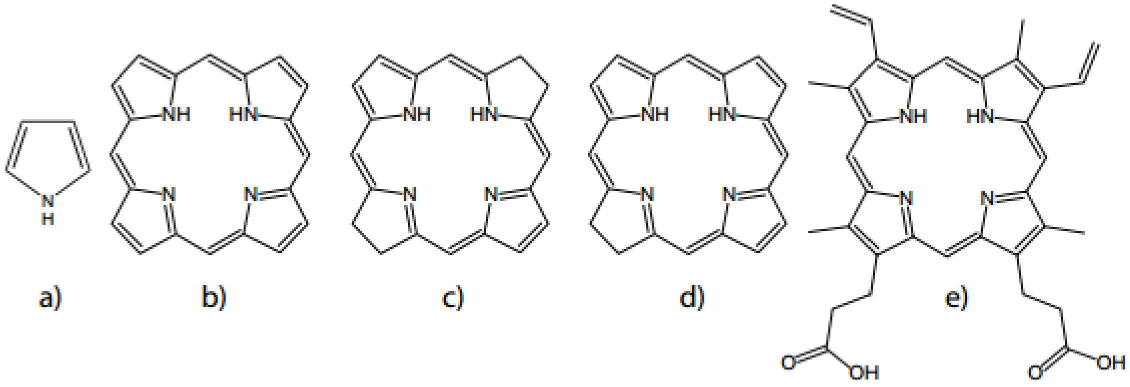

FIGURE 6 (8) THE BASIC UNIT OF THE PORPHYRIN’S RING ; THE PYRROLE A) AND THE DIFFERENCES BETWEEN THE DIFFERENT MEMBERS OF THE PORPHYRINS’ FAMILY; B) PORPHYRIN, C) CHLORIN, D) BACTERIOCHLORIN, E) PROTOPORPHYRIN IX.

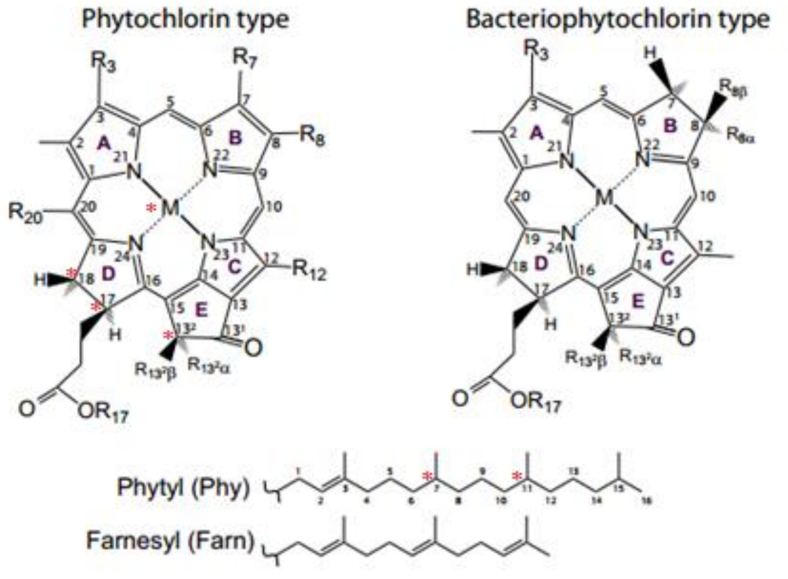

FIGURE 7 (8)THE FIGURE ABOVE ENUMERATES THE BASIC STRUCTURE OF THE PHYTOCHLORINE AND THE BACTERIOPHYTOCHOLRIN RING WHICH CORRESPOND WITH CHLOROPHYLL A AND THE BACTERIOCHLOROPHYLL ,RESPECTIVELY. ON THE BOTTOM OF THE FIGURE THERE ARE THE TWO MOST COMMON “TAILS” CONNECTED ON THE R-17 POSITION.

The chlorin ring is formed when the double bond between C-17 and C-18 is saturated. Furthermore, the saturation of the porphyrin ring between C-7 and C-8 leads to the bacteriochlorin macrocycle. All the chlorophylls found in nature have the basic ring structure reported in figure 6. The organic molecule haem, for example, is a protoporphyrin IX derivative and has a crucial role in oxygen binding in the blood giving its distinctive red color. Chlorophyll molecules are formed from a chlorin ring which has an additional isocyclic ring fused into the porphine structure which gives the prefix “phyto” to the name. In addition, chlorophylls are generally complexed with a Mg at the ion centre of the ring and with an alcohol esterified to the C-17 propionic acid chain. The molecule has also six asymmetric centers, two of them contained in the phytol chain at position C-7 and C-11 and four contained in the heteroaromatic ring in positions C-13, C-17, C-18 and in the central metal (signed as * in figure 7).

1.3.1 THE PERIPHERAL SUBSTITUENTS

Since the central atom and the esterifying alcohol do not change, most of differences between Chls are in the peripheral substituents. Different substituents around the macrocycle influence aggregation and optical proprieties (8). The group C=O at C-13 becomes coplanar to the macrocycle after the cyclization. The additional inflexibility of the macrocycle leads to a red shift of the absorption spectra and to a reduction in the probability of ISC in the excited state. H-bonding that involves the 13 C=O group has been recognized an important factor for aggregation and for interaction with proteins (16).

1.3.2 THE CENTRAL METAL ION

Chlorophylls are well known for their capability to complex with metals (18). The nature of the metal has a strong impact on the excited state kinetics, as well as, on the biological function. The maximizing of excited state life time due to the incorporation of Mg ion as a central metal leads to a low yield of intersystem crossing to the triplet state. Open d-shell metals and heavy metals have not been selected in the evolution process as the central metal because of the high probability of inter system crossing they induce (8). Other metals not selected are those that form unstable complexes, like K, Na, Li and Ca and trivalent metals that introduce an extra charge. As a result, in nature Mg^{++}, Zn^{++} and $2H^{+}$ are the only possible forms in which chlorophyll can be found (8) (19). However, magnesium was selected for the photosynthesis process probably because of its lower mass, that makes the ISC less probable. Nevertheless, Mg-Chls and Zn-Chls show similar behaviour in their complexes (20) (21).

1.3.3 ESTERIFICATION

The esterified alcohol chain is another important substituent, located at C-17 (shown in fig 7) which strongly influences Chlorophyll’s properties. The most common chains for chlorophylls are phytyl and farnesyl and they are illustrated in fig 7. Even though they have a strong influence on the interaction with the environment, esterified alcohol chains do not influence the electronic structure of the molecule, because they lack conjugation with the π orbitals. The phytyl chain is hydrophobic and this is responsible for the lack of solubility of Chlorophyll a (and others Chls containing the phytyl chain) in water. It has also a considerable influence on the aggregation properties of Chlorophyll and in particular in micellar systems (22). The alcohol substituent, in addition, is responsible for the orientation and the distance between chlorophylls in a complex, and this is an important aspect in vivo for photosynthetic systems in the energy transfer process.

1.4 AGGREGATION

In nature, Chlorophylls can be found as monomers or in aggregate form or in protein-pigment complexes. In complexes, proteins ensure the correct distance and orientation between chromophores since if their packing is too dense the light harvesting is compromised by concentration quenching (8). An example of aggregate forms of chlorophylls is in the green photosynthetic bacteria that live in low light environments. They are the most efficient example of natural antenna system formed by self-assembly. Recently, scientists were able to reproduce these tubular structure aggregates in vitro with BChls or ZnChl (23). Non-covalent interactions between the pigments lead to molecules coming together to form supramolecular assemblies. The Mg metal, coordinated inside the ring, plays the most important role in aggregation. It is an electrophilic center of the molecule which is rarely four coordinate because of the nature of "hard" acids. This leads it to interact easily with Lewis bases. As a result of this, the metal is always pentacoordinated with solvent electron donor or, in case of nonpolar solvents, with another Chl pigment. The central atom is involved in the interaction with the apo-protein in vivo (17). The ligand interaction is also responsible for the changes in the electron density of the macro cycle which influences the molecular properties (24). Hydrogen bonding is the second supramolecular interaction in terms of strength, and it is characterized by a strong directionality. In such cases the carbonyl group C=O and the central metal act as H-bond acceptor groups while the 3-OH can have both acceptor and donor functions. Several structures have been characterized for Chl pigments which involve different final structures (8) (25) (26). Here we are going to report the most representative in order to make a clear picture about how hydrogen bonds influence the structure of the aggregate (see the following figures 8, 9 and 10).

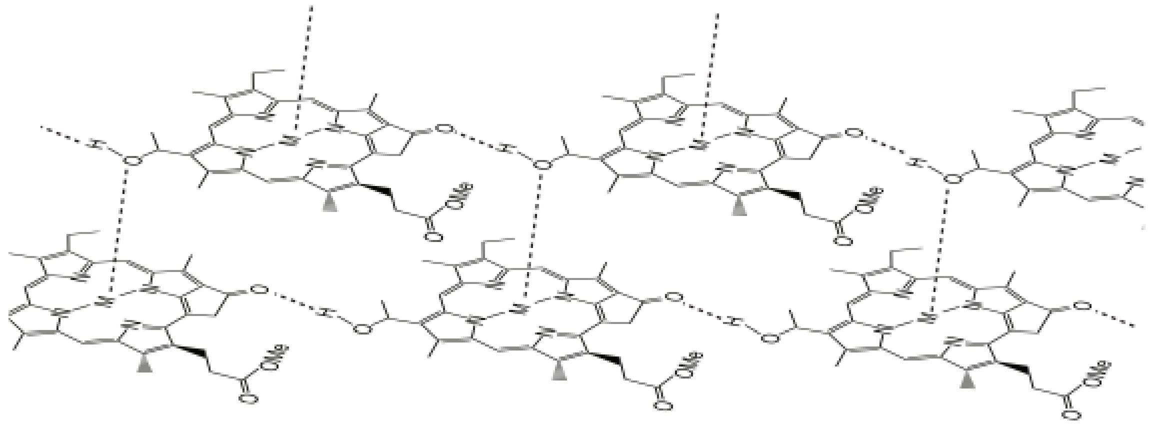

Figure 8 (8) *the figure shows Chlorophylls oriented parallel by the H-bond network. The replacement of the phytyl chain with a methyl group leads to formation of stacks. The 3-OH group donates its electrons to the central metal and it is also coordinated with the carboxyl group that is an hydrogen bond acceptor.*

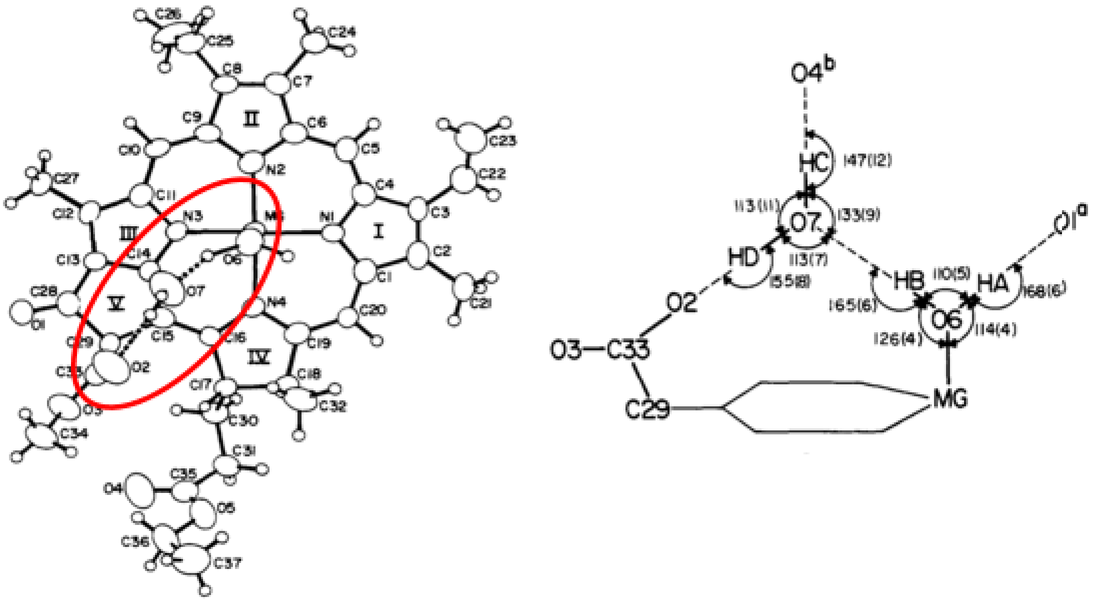

Figure 9 (25) *the figure shows ethyl-chlorophyllide molecule (a chlorophyll derivative) with the structure suggested by X-ray. While one of the water molecules is coordinated with the metal, the second acts as a bridge between the first molecule and the carboxyl group.*

Chlorophylls have a strong tendency to aggregate in aqueous solvent. The presence of water plays an important role in the chlorophyll aggregation because the solute can become part of the H-bond network.

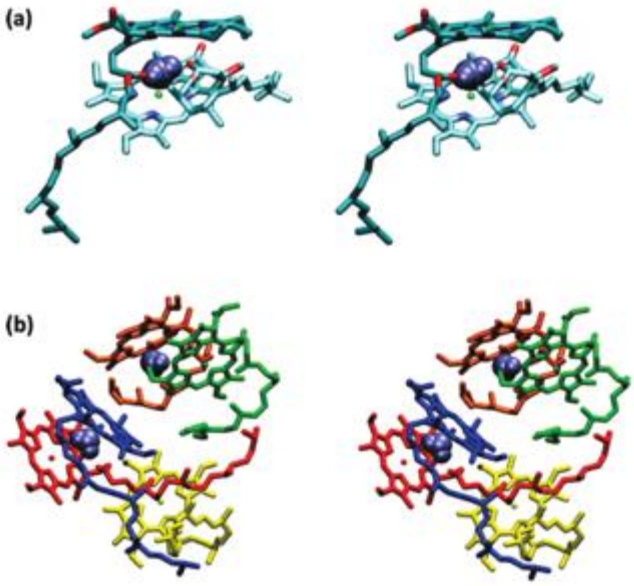

Figure 10 (26) *the figure above comes from a theoretical calculation of chlorophyll in water. a) The dimer has a water molecule in a “sandwich” conformation between two chlorophyll molecules. The water is coordinated with the metal in one molecule and it forms an H-bond with the carboxy group of the IV ring in the other. b) In the globular aggregate, water plays a similar role with the same kind of coordination between pigments.* (26)

Finally, the aromatic macrocycle with its π-π interactions also leads to a pronounced tendency towards aggregation. This interaction comes from intermolecular overlaps of π orbitals that also play a substantial role in pigment-protein complexes (27) (28). Compared to the monomer, chlorophyll aggregates exhibit a lower fluorescence and a shorter excited state lifetime (27). In some cases the diminution of florescence can be explained by energy transfer and concentration quenching. The excitonic theory developed by Davydov (29) shows that aggregation leads to an increase probability of ISC and then, in certain cases, to a greater population of the triplet state (30). Some of these properties are discussed further in the next sections

1.4.1 THEORY OF OPTICAL PROPERTIES OF AGGREGATES

Aggregation generally brings about a shift of the absorption spectra of planar aromatic molecules that can be qualitatively explained through the exciton model introduced by Kasha et al. (30). In this model, molecules interact with each other mainly by Columbic interactions in a way which depends on their orientation. This interaction will be briefly illustrated by making some consideration of the basic force behind the dipole-dipole coupling. This will be illustrated with the dimer and the linear aggregate case, for the two types of aggregate J and H. The following discussion is based on the thesis of Dr. Julius-Maximilians's (31).

1.4.1.1 DIPOLE-DIPOLE INTERACTION

Looking at the transition dipole moment, its potential can be described as a charge density distributions expressed by a multipole expansion (32). The first term of this expansion corresponds to the dipole-dipole interaction. The potential $\phi(\vec{r})$ of a dipole $\vec{\mu}$ located at a distance $\vec{r}$ can be then express as

$$\phi(\vec{r}) = \frac{1}{4\pi\varepsilon_0}\frac{1}{|\vec{r}-\vec{r}|^2}\frac{\vec{\mu}\,(\vec{r}-\overrightarrow{r\prime})}{|\vec{r}-\overrightarrow{r\prime}|} \qquad . \qquad (1$$

Here $\vec{\mu}$ is the dipole moment and $\left(\vec{r}-\overrightarrow{r'}\right)$ expresses the distance between the center of the dipole and the point at which the potential is monitored. The electric field associated with the dipole potential, can be expressed as:

$$\vec{E}_{\mu}(\vec{r}) = -\nabla\phi(\vec{\boldsymbol{r}}) = -\frac{1}{4\pi\varepsilon_0}\frac{1}{|\vec{\boldsymbol{r}}-\vec{\boldsymbol{r}}|^3}\left(\vec{\mu} - \frac{\mathbf{3}\left(\vec{\mu}(\vec{\boldsymbol{r}}-\overrightarrow{\boldsymbol{r\prime}})(\vec{\boldsymbol{r}}-\overrightarrow{\boldsymbol{r\prime}})\right)}{|\vec{\boldsymbol{r}}-\overrightarrow{\boldsymbol{r\prime}}|^2}\right) \qquad (2$$

Considering now a second transition dipole moment, $\overrightarrow{\mu}_2$, it will feel the field of $\vec{\mu}_1$ with an interaction energy V (often referred to as dipole-dipole coupling).

$$V = -\vec{\mu}_2\vec{E}_{\mu}(\vec{r}_2) = \frac{1}{4\pi\varepsilon_0}\frac{1}{|\vec{r}_2-\vec{r}_1|^3}\left(\vec{\mu}_1\vec{\mu}_2 - \frac{3\left(\vec{\mu}_1(\vec{r}_2-\vec{r}_1)\right)\vec{\mu}_2(\vec{r}_2-\vec{r}_1)}{|\vec{r}_2-\vec{r}_1|^2}\right) \qquad (3$$

This potential can be rewritten as a function of the center-to-center distance vector $\vec{R}_{12} = \vec{r}_2 - \vec{r}_1$, the inter-dipole angle α and the angle θ_1 as follow (angles and the distance vector are illustrated in figure 11).

$$V = \frac{1}{4\pi\varepsilon_0}\left(\frac{\mu_1\mu_2 \cos\alpha}{R_{12}^3} - \frac{3\mu_1\mu_2 \cos\theta_1 \cos(\theta_1+\alpha)}{R_{12}^5}\right) \tag*{(4}$$

Where the angle θ_1 is identified by $\theta_2 = \theta_1 - \alpha$. As shown in Figure 11, the resulting interaction for a fixed distance R_{12} changes according to angles θ_1 and α. The interaction energy spans the range between $V_{min} = -\frac{2}{4\pi\varepsilon_0}\left(\frac{\mu_1\mu_2}{R_{12}^3}\right) \leq V \leq \frac{2}{4\pi\varepsilon_0}\left(\frac{\mu_1\mu_2}{R_{12}^3}\right) = V_{max}$ with the lowest energy corresponding to the in-line arrangement of two parallel dipoles and the highest energy resulting from an antiparallel orientation. The dipole-dipole coupling turns out to be zero for two limiting cases. The first corresponds to the perpendicular orientation between the two dipoles with one of them perpendicular to R_{12}. The other occurs for parallel dipoles ($\alpha = 0$) with the angle θ_1 equal to the magic angle that is 54.7°. From the inclination of θ_1, we can distinguish two cases that will be important later on for the spectroscopic quantification of aggregates; for an arrangement with $\theta_1 > 54.7$ we refer to the H-type, while one with $\theta_1 < 54.7$ defines the J-Type.

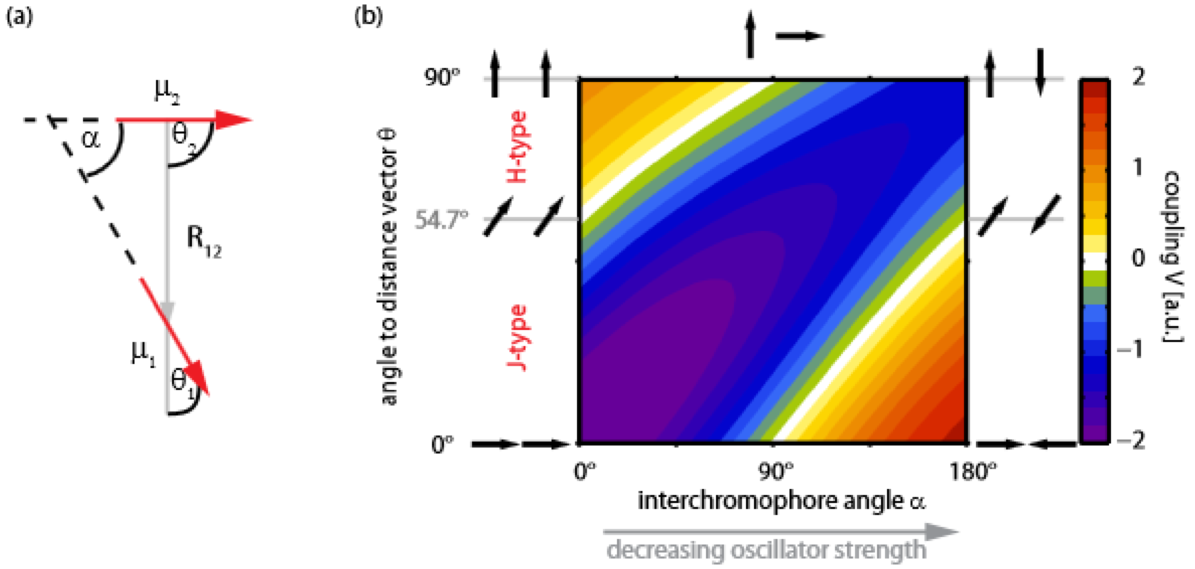

FIGURE 11 (31) *A) THE ANGLES DEFINED BETWEEN TWO DIPOLES. B) THE 2D GRAPH SHOWS HOW THE INTERACTION POTENTIAL BETWEEN TWO DIPOLES AT A FIXED DISTANCE CHANGES BY VARYING THE ANGLE DISTANCE VECTOR IN RELATION TO THE INTERCHROMOPHORE ANGLE.*

Taking the modulus of the coupling strength $|V|$, for a fixed distance it can be noticed that it is smaller for the H type (θ_1 = 90) than the J (θ_1 = 0) (i.e. from the top to the bottom on the left of Fig 11 (b)). For the J type arrangement the net transition dipole moment has its maximum in $|V|$ modulus for the lowest energy and it vanishes for α = 90°. On the contrary, the H-case has the tendency to have a stronger coupling for the least favorable arrangement (upper left corner figure 11) and a potential equal to zero for the antiparallel arrangement.

1.4.1.2 EXCITON COUPLING THEORY

In this section we introduce the exciton theory for a better understanding of the general properties of different aggregates and how the molecular orientation is responsible for different shifts in the absorbance spectra. For this purpose, an introduction to the basic Hamiltonian will be made for general considerations of electronic states. After this two examples will be given to explain the spectral properties.

The Hamiltonian describing *N* interacting chromophores can be written as:

$$\hat{H} = \sum_{i=1}^{N} \left(\hat{H}_i + \frac{1}{2} \sum_{i=j, j \neq i}^{N} \hat{V}_{ij} \right) \qquad (5$$

Where H_i represents the energy of the *N* molecules in isolated conditions, while the second term is the sum of the electronic couplings (expressed by dipole-dipole interactions) between the molecule j and i. While the numerical diagonalization of the Hamiltonian can be done for simple systems, the analytical solution of the Schrodinger equation can be obtained only for certain ideal cases. Before discussing these ideal cases, some considerations regarding the eigenstates in coupled systems are required. First, we can assume that the number of eigenstates found for a coupled system of *N* molecules is the same as for an uncoupled system. In a system of *N* molecules with two levels system, for instance, we expect to calculate 2*N* eigenstates. Second, in a system where there are *N* molecules excited, there has to be a manifold of $\frac{N}{m!(N-m)!}$ states that describe a system which shares a number of m excitations in their ensemble. These states are commonly denominated as m-exciton bands and are subject to the selection rule $\Delta \mathrm{m} = \pm 1$

under the dipole approximation. Therefore, for cases where coupling is smaller than the electronic transition energy $V \ll \hbar\nu$, the energy of mth exciton band can be approximated as E$\sim m\hbar\nu$ .The last assumption is the sharing of the ground state between all the coupled chromophores. Its value is approximated as a product of all the individual ground state molecules. For the simplest case of coupled system, the dimer, the analytical solutions are:

$$E_{1/2} = E_{\pm} = \frac{1}{2}\left(e_1 + e_2 \pm \sqrt{\Delta e^2 + |V|^2}\right) \qquad (6$$

Where Δe is the difference between the energy levels e_1 and e_2 of two monomers. The corresponding one-electron eigenstates are written as a linear combination of product states in which only one of the two molecules is excited

$$\Psi_+ = \cos\theta_{mix}\,|1\rangle - \sin\theta_{mix}\,|2\rangle \qquad (7$$

$$\Psi_- = \sin\theta_{mix}\,|1\rangle + \cos\theta_{mix}\,|2\rangle \qquad (8$$

In the equations above, $|1\rangle$ and $|2\rangle$ are the product states and θ_{mix} is the mixing angle equal to $\theta_{mix} = \frac{1}{2}\arctan\left(\frac{V}{\Delta e}\right)$. In the particular case of an homodimer ($e_1 = e_2$ and $\mu_1 = \mu_2$) the mixing angle varies between $\pm\frac{\pi}{4}$ leading to a full delocalization of the one-exciton state over both monomers. When the coupling is smaller than the energy difference, $V \ll \Delta e$, the one-exciton state maintains the feature of the uncoupled situation.

The transition dipole moment between the ground state and either of the excited states $\langle 0|\vec{\mu}|\Psi_{\pm}\rangle$ can be express by:

$$\overrightarrow{M}_+ = \cos\theta_{mix}\,\vec{\mu}_1 - \sin\theta_{mix}\,\vec{\mu}_2 \qquad (9$$

$$\overrightarrow{M}_- = \sin\theta_{mix}\,\vec{\mu}_1 + \cos\theta_{mix}\,\vec{\mu}_2 \qquad (10$$

In figure 12, for the case of two in-line dipoles, the potential V is negative and the mixing angle is equal to $-\frac{\pi}{4}$. In the homodimer case the exciton state Ψ_- carries the oscillator strength of the transition, while Ψ_+ stays dark. This leads to a red shift in the absorption spectra that is typical of the supramolecular organizations called J aggregates. On the contrary, in the case of parallel dipoles the upper transition is the one allowed, leading to a shift in the blue region typical of a complex of molecules called H aggregates. These two cases become less extreme for heterodimers because the dark state is no longer completely forbidden.

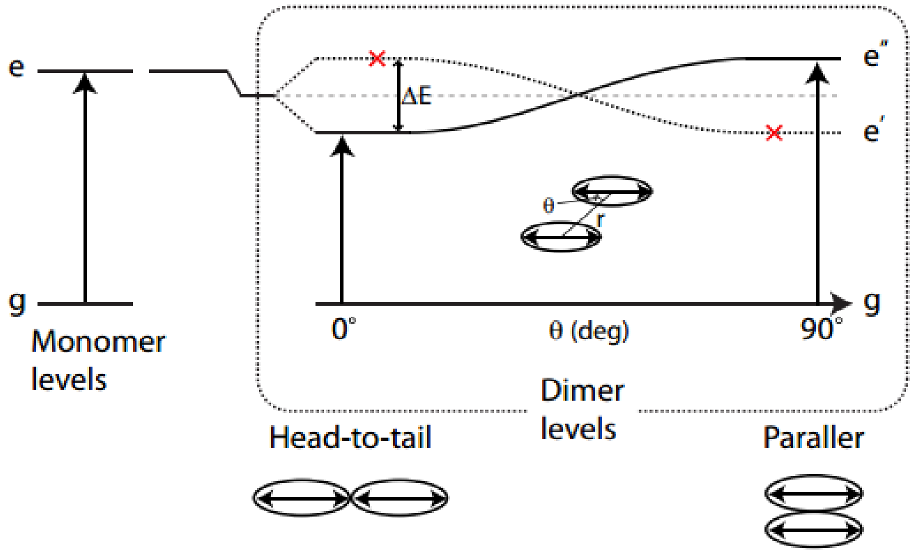

FIGURE 12 (8) REPRESENTATION OF EXCITON ENERGY BANDS FOR A HOMODIMER WITH PARALLEL TRANSITION DIPOLES. THE PICTURE REPRESENTS THE TRANSITION BETWEEN THE TWO LIMITING CASES OF AGGREGATES; THE J AND H TYPE. WHEN THE DIMER SYSTEM LIES IN THE HEAD-TO-TAIL CONFIGURATION, THE DIPOLE-DIPOLE POTENTIAL ACHIEVES ITS LOWEST VALUE LEADING TO A MIXING ANGLE WITH A VALUE OF-$\frac{\pi}{4}$*.THIS ACCORDING TO EQ 9 AND 10 MAKES THE LOWER LEVEL THE ONE THAT CARRY ON THE TRANSITION (J-CASE). ON THE CONTRARY, AN ANGLE BETWEEN THE TWO DIPOLES CALLED THE MAGIC ANGLE GIVES POSITIVE VALUES OF V OBTAINING ITS MAXIMUM FOR THE PARALLEL ALIGNMENT. HERE , THE MIXING ANGLE WITH ITS VALUE OF* $+\frac{\pi}{4}$ *MAKES THE UPPER LEVEL THE ONE RESPONSIBLE FOR THE TRANSITION (H-CASE)).*

Next, we consider the case of exciton coupling involving more than two chromophores by describing the ideal case of a linear aggregate. In this model, N identical two level molecules are equidistant and parallel to each other. Given that the dipole-dipole interaction varies as ${}^{1}/_{r^3}$, it is a good approximation to only consider interactions between neighbors.

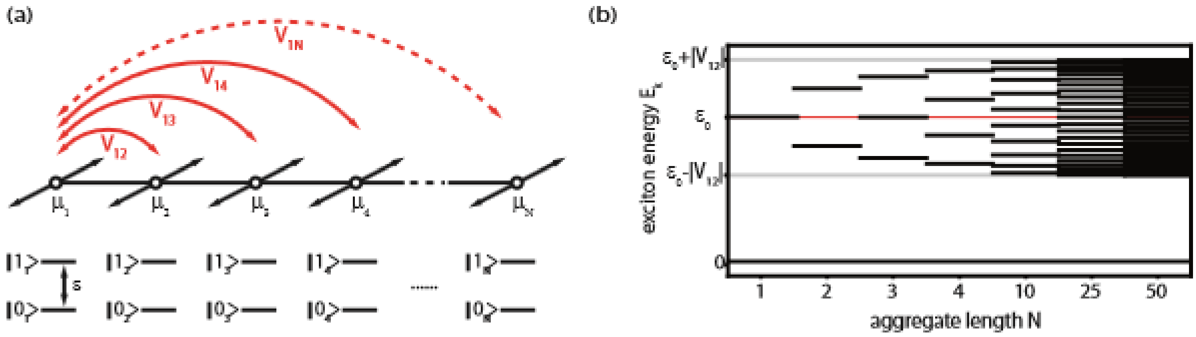

FIGURE 13 (31) *A) REPRESENTATION OF AN IDEAL LINEAR AGGREGATE WITH N MOLECULES INTERACTING WITH PARALLEL TRANSITION DIPOLES . B) SCHEME SHOWING THE EXCITON ENERGIES FOR DIFFERENT AGGREGATE LENGTH N .*

The analytical solution of eigenstates is possible for this linear system (33) and, as for the dimer case, it is written as a linear combination of $|n\rangle$ states where all the molecules are in the ground state making exception of the molecule *n* (34) .

$$\Psi_k^1 = \sqrt{\frac{2}{N+1}} \sum_{n=1}^{N} sin\left(\frac{n\pi k}{N+1}\right) |n\rangle \qquad K = 1 \ldots N \qquad (11$$

The eigenvalues from the Schrödinger equation are;

$$E_k^1 = \omega_o + V\, cos\left(\frac{\pi k}{N+1}\right) \qquad (12$$

Looking at the equation 12, it can be seen that the Δe leads to 2V for a number of molecules becomes infinite, while it achieves only the value of V in the homodimer case (figure 13 b). The cos(1/N) dependence also shows that for the case N =9 the spread of energy levels almost achieves its maximum (95%) (see picture 13 (b)). The transition dipole moment is defined in this case as follow;

$$M_{0k}^{1}\begin{cases}\cot\left(\frac{\pi k}{2N+1}\right) & \text{k odd}\\ 0 & \text{k even}\end{cases}$$

(13

In this model, the one-exciton state with $k = 1$ is the transition that dominates in the absorption having 81% percent of the total oscillator strength for an infinite linear aggregate. The predominance of the one exciton state implies that an aggregate spectrum corresponds mainly to one absorption transition. This becomes clearer, considering the wave functions for values of k even or large odd k (equation 13) and looking as their dipoles add destructively. The absorbance shift in the spectra depends, as in the dimer case, on the interaction energy V leading to a distinction between the J and H cases. For the J-aggregates, the negative potential $V < 0$ makes the state of $k = 1$ correspond to the lowest energy level, leading to the characteristic bathochromic shift. On the contrary, the positive potential $V > 0$ in the H-aggregates generates a hypsochromic shift for the same reasons. Clearly an increase of the spectral shift is expected for larger aggregates, but the shift provides only limited information about the number of the molecules involved in the aggregate. This is because, as we have seen, the cos(1/N) dependence reaches almost the maximum spectral shift for 9 coupled monomeric units, so N > 9 may not be detected.

1.2 WHAT 2DES CAN DO

In the last five years (35), 2DES has become an important tool for probing molecular systems, because it provides extra information that is not accessible with traditional 1D nonlinear techniques, such as pump-probe spectroscopy. This section, without claiming for completeness, aims to illustrate some of the unique capabilities of 2DES. Some of the pictures and part of the discussion are based from the thesis of Alexandra Nemeth (36).

1.2.1 Analysis of homogenous and inhomogeneous line-shape

2DES spectroscopy is a method ideally suited to distinguish directly between homogeneous and inhomogeneous contributions to the line-shape, a property it shares with photon echo techniques. In the 1D frequency domain representation, the spectral broadening of an electronic transition hides information about intra and intermolecular interactions. According to traditional theories of spectral line-shape, the broadening effect is represented by contributions from the two limits of homogeneous and inhomogeneous linewidths.

The homogeneous contribution is a dynamic broadening generated by rapid variations in the amplitude, phase or orientation of dipoles in the molecules probed. All these effects contribute to an exponential decay of the dephasing time, T_2, which is related to the spectral linewidth. A Lorentzian line-shape is thus indicative of a pure homogeneous broadening. Inhomogeneous contributions, on the other hand, reflect a static distribution of frequencies due to the different local environments felt by the molecule in the sample. The probability of population of a particular environment is not the same for all the molecules of the sample, with a randon distribution giving rise to a distribution of frequencies represented by a Gaussian lineshape.

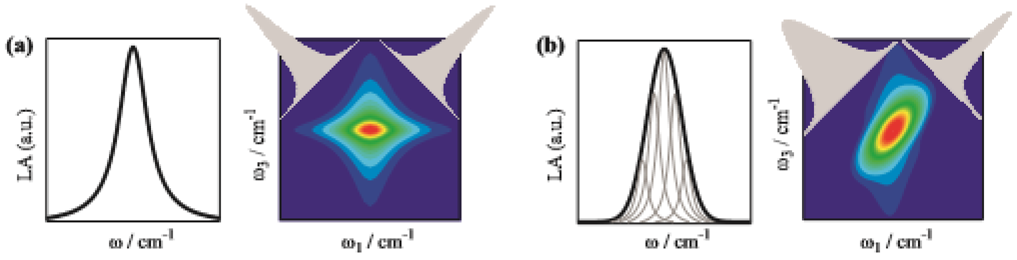

Figure 14 the figure shows (37) the homogeneous case (left) and the inhomogeneous case (right) compared with the linear spectra. As can be noted, the homogeneous case shows Lorentzian distributions on the diagonal and on the anti diagonal of the 2DES

SPECTRA. ON THE CONTRARY, IN THE INHOMOGENEOUS CASE THE DIAGONAL CUT IS MORE ELONGATED WITH A GAUSSIAN DISTRIBUTION.

Linear absorption spectra do not allow one to distinguish homogeneous and inhomogeneous contributions. The 2DES spectra however, show clearly the differences between these two, by looking at the cut on the diagonal and anti diagonal of the 2D plot (Figure 14). In the homogeneous case the cuts taken along the diagonal and the anti-diagonal yield Lorentzian line-shape of the same width. As the inhomogeneous contribution increases, the peak broadens along the diagonal axis while the anti-diagonal width stays the same. In this case, the degree of ellipticity of the peak can be taken as an indicator of inhomogeneity present in the system under investigation. Most significantly 2DES recorded for different population times yield different distributions which indicate dynamics spectral diffusion, which scales between the homogeneous and inhomogeneous limits; we return to this point in the Results section.

1.2.1.1. PROBING SPECTRAL DIFFUSION IN 2DES SPECTRA

In the 2DES spectra, the spectral diffusion is manifested by the change in the shape of the response with increasing population time T (the timings in 2DES are described below). The system is initially inhomogeneous because molecules probed feel different local environments, but as the population time becomes longer the molecules will have time to stochastically sample all the local environments leading to the loss of the initial correlation with the transition frequency (38). As the result of this, 2DES spectra show a decay of the initial asymmetry in the elliptical distribution with increasing population time; that is a direct measure of the rate of spectral diffusion (Figure 15).

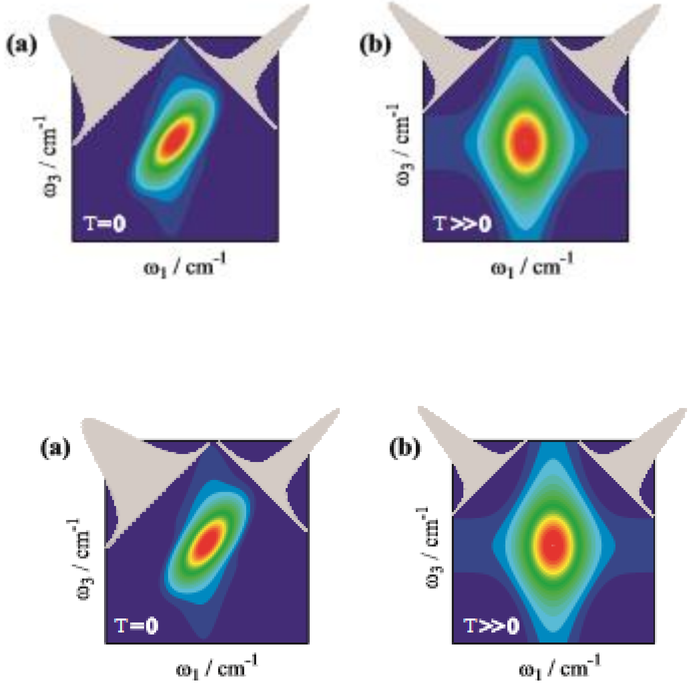

Figure 15 (37) *The two calculated 2DES spectra show a two levels system for different population times T. The evolution of the peak along the diagonal reveals the spectral diffusion changing its distribution from Gaussian to Lorentzian.*

If the frequency evolves rapidly relative to the inverse of the distribution frequencies Δ^{-1}, the system samples all possible sites rapidly and is homogeneously broadened. Otherwise, if the system changes slowly during this time it is inhomogeneous. The time correlation function $C_{eg}(t) = \langle \omega_{eg}(t)\omega_{eg}(0) \rangle$ is used to qualify spectral diffusion behavior. It can be approximated by the evolution in the ellipticity of the 2DES response. This is illustrated in Figure 16.

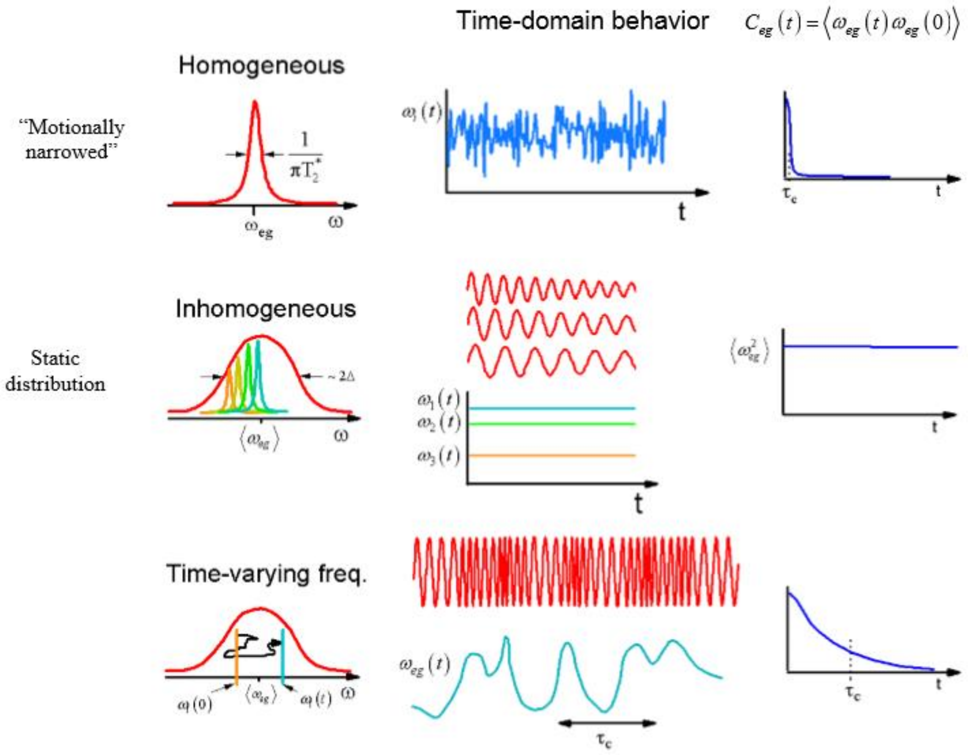

FIGURE 16 (39)*THE FIGURE SHOW THE HOMOGENOUS, INHOMOGENEOUS AND INTERMEDIATE CASE. IN THE HOMOGENEOUS CASE THE TRANSITION FREQUENCY ω CHANGES RAPIDLY IN THE TIME DOMAIN SO ITS CORRELATION FUNCTION DECAY IS FAST. IN THE INHOMOGENEOUS CASE WE DESCRIBE A STATIC DISTRIBUTION WHERE EACH MOLECULE FEELS A DIFFERENT ENVIRONMENTS AND THUS OSCILLATES WITH A FREQUENCY SLIGHTLY DIFFERENT BETWEEN FROM THE OTHERS. THE CORRELATION FUNCTION IN THIS CASE IS DESCRIBED AS AN AVERAGE OF FREQUENCIES OF THE SAMPLE AND FOR THIS REASON THE GRAPH IS DESCRIBED BY A LINE. THE FINAL CASE SHOW THE INTERMEDIATE SYSTEM WITH ITS EXCHANGES BETWEEN STATIC AND DYNAMIC CASE. AS A RESULT OF THIS, THE EVOLUTION OF THE FREQUENCY AND THE CORRELATION FUNCTION ARE INTERMEDIATE BETWEEN THE HOMOGENEOUS AND INHOMOGENEOUS CASE.*

1.2.2. ELECTRONIC COUPLING

Electronic coupling is a phenomenon present in many chemical systems, for instance, molecular aggregates (discussed above), conducting polymers and photosynthetic complexes. 2DES spectroscopy offers the advantage of identifying electronic coupling by the presence or absence of cross-peaks. For two uncoupled nondegenerate two level systems the 2DES spectra show two peaks along the diagonal. The absence of off diagonal signals means there is no coupling. When an electronic coupling exists, cross-peaks are present from T = 0. Thus, 2DES spectra will show four peaks two lying along the diagonal and two off diagonal. The peaks along the diagonal represent the transitions from the ground state to each individual singlet-excited state, while the off-diagonal peaks originate from excitation at one frequency and detection at the other transition, due to their common ground state (40). The intensity is proportional to the square of the transition dipole moments i.e. $\propto |\mu_i|^2\left|\mu_j\right|^2$ in the cross-peaks and to $|\mu_i|^4$ for diagonal peaks.

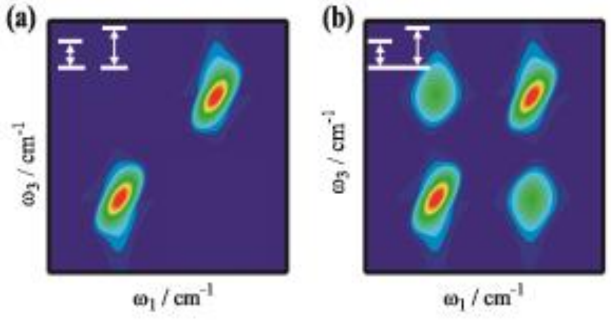

FIGURE 17 (37) *THE 2DES SPECTRA REPRESENT THE UNCOUPLED (A) AND COUPLED (B) CASE FOR A TWO LEVEL SYSTEM. AS CAN BE NOTED, THE COUPLED CASE IS CHARACTERIZE BY THE APPEARANCE OF CROSS PEAKS FOR T=0.*

1.2.3 STUDY THE PATHWAYS OF ENERGY TRANSFER.

Cross-peaks can be also generated by energy transfer processes in the excited state manifold due to a weak coupling between electronic levels; excitation of the donor results in emission from the acceptor, giving rise to the cross peak. The evolution of the cross-peaks for increasing waiting time T allows understanding the pathways and timescales of these energy transfer processes. Whereas cross peaks evolving at frequencies $\omega_1 > \omega_3$ are responsible for downhill transfer steps, the evolution of the peaks in the upper half of the triangle $\omega_1 < \omega_3$ shows the evolution of uphill energy transfer. Energy transfer processes have been monitored in a number of natural (41) (42) and artificial (36) (43) light harvesting processes making it an important and useful phenomenon to study by 2DES; an example is given in Figure 18.

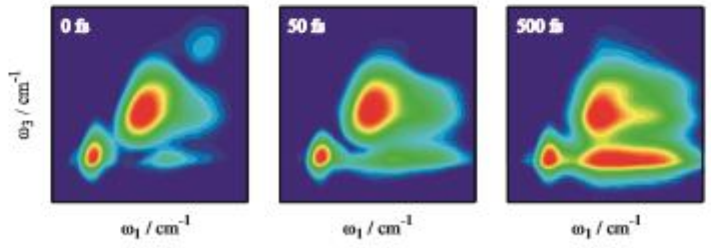

FIGURE 18 (36) *EXAMPLE OF 2DES SPECTRA FOR DIFFERENT WAITING TIMES THAT REVEALS THE PATHWAYS OF ENERGY TRANSFER IN THE SYSTEM CARBOCYANINE DYE C8O3.*

1.2.4 CHARACTERIZATION OF VIBRONIC COHERENCES.

The short width of femtosecond pulses in the time domain used in 2DES spectroscopy allows the excitation to cover a broad part of the spectral domain and therefore to excite coherently a number of vibrational levels. 2DES allows to one observe the vibrational wave packets through oscillations of signal intensity during the population time and as line-shape changes (44) (45). When there are excited high frequency vibrations, the 2DES spectra show distinct diagonal and cross-peaks (46) (47) (48), whereas low frequency vibrations present only a single overlapped peak, but oscillations are still resolved (48) (49) (50).

1.2.5 REVEAL ELECTRONIC COHERENCE.

Recently, theoretical and experimental studies have proposed that quantum coherence might be important to increase the efficiency of energy transfer processes in photosynthetic complexes. In a simple model of two coupled oscillators (such as in the homodimer described above, the system oscillates under electronic coherence with a period given by the energy gap between the two states involved, which in turn reflects the structure. It is sometimes challenging to distinguish electronic and vibronic coherences, though study of the rephrasing and non-rephasing response helps (see below).

2. THEORETICAL BACKGROUND

This section aims to give the basic background behind the experiment and the analysis of the 2DES results given in the following chapters. The first part are based closely on the books "Principles of Nonlinear Optical Spectroscopy: A Practical Approach" and "Concepts and Methods of 2D Infrared Spectroscopy" (51) (52) (39). Based on these we give an introduction to the density matrix formalism and its relation to the macroscopic third order polarization measured in 2DES. Then, the focus moves to Feynman diagrams and the resultant rules for drawing then and relating them to vibronic and electronic coherences. Finally, a brief explanation of heterodyne detection, used in our apparatus, is given in section 2.5.

The second part gives the background used to interpret the results obtained from the measurements of the Bchla monomer in different solvents by 2DES. It is a theoretical description of the line shape function (53) used to interpret the observed spectral diffusion (Chapter 4).

2.1 DENSITY MATRIX

In Liouville Space, the system is described by the density matrix instead of the wavefunction Ψ formalism:

$$\rho(t) = |\Psi(t)\rangle\langle(t)\Psi| \qquad (14$$

Assuming the existence of a complete orthonormal set of eigenstates, the ket and the bra side are written as:

$$|\Psi\rangle = \sum_n c_n\, |n\rangle \qquad (15$$

$$\langle\Psi| = \sum_n c_n^* \langle n| \qquad (16$$

The complete density matrix then reads after some manipulation as:

$$\rho \equiv |\Psi(t)\rangle\langle(t)\Psi| = \sum_{n,m} c_n c_m^* \, |n\rangle\langle m| = \sum_{n,m} \rho_{nm} \; |n\rangle\langle m| \qquad (17$$

Where ρ_{nm} is an element of the density matrix expressed in the matrix formalism.

For describing a system that evolves in time, the time derivative of the density matrix is used:

$$\frac{d}{dt}\rho = \frac{d}{dt}(|\Psi\rangle\langle\Psi|) = \left(\frac{d}{dt}|\Psi\rangle\right).\langle\Psi| + |\Psi\rangle.\left(\frac{d}{dt}\langle\Psi|\right) \qquad (18$$

Knowing that the Schrodinger equation describes the time evolution of the wave function, we can use it in eq 18 (39)

$$\frac{d}{dt}\rho = \frac{i}{\hbar}\hat{H}|\Psi\rangle\langle\Psi| + \frac{i}{\hbar}|\Psi\rangle\langle\Psi| = -\frac{i}{\hbar}\hat{H}\rho + \frac{i}{\hbar}\hat{H}\rho = -\frac{i}{\hbar}\left[\hat{H},\rho\right] \qquad (19$$

We obtain, in this way, the Liouville‑von Neumann equation which describes the time evolution of the density matrix acting on the Hamiltonian from the left and the right side; the [⋯] represents the commutator (39). Comparing eq 19 to the Schrodinger equation, it may be noted that they are equivalent for a pure state.

$$\frac{1}{dt}|\Psi\rangle = -\frac{1}{\hbar}H|\Psi\rangle \leftrightarrow \frac{1}{dt}\rho = -\frac{i}{\hbar}\left[\hat{H},\rho\right] \qquad (20$$

Thus, the density matrix does not add any new meaning at present. However, in condensed-phase systems, molecules are seen as statistical ensembles. The wave function cannot be written as a statistical average of the system because the statistical weights are used to express the linear combination of eigenstates for a pure state. The statistical average of the different thermal distribution in the sample are then described by the density matrix formalism. Defining the constant p_s as the probability of a system to be in a state $|\Psi_s\rangle$, the density matrix of an ensemble is expressed as;

$$\rho(t) = \sum_s p_s\, |\Psi\rangle\langle\Psi| \qquad (21$$

With each $p_s \geq 0$ and $\sum_s p_s = 1$ (i.e. the normalization condition).

Before continuing our discussion, we have to prove that using the density matrix formalism we describe the system as we would using the wave function. In order to do that, we derive the formulas for the expectation value of any given operator and the time evolution of the system. The expectation value of an operator for a mixture of pure states is given by the sum of expectation values for each system weighted for the probability of the pure state. For the pure state $|\Psi^j\rangle$, an operator $\langle\hat{A}\rangle$ can be described as

$$\langle\hat{A}\rangle = \langle\Psi^j|\hat{A}|\Psi^j\rangle = \sum_n \sum_m (\rho)_{n,m} A_{mn} \qquad (22$$

Where ρ is explicitly denoted as the density matrix of the pure state j. Being the sum over m the matrix product between ρ^j and A, equation 22 becomes:

$$\langle\hat{A}\rangle^j = \sum_n \left(\rho^j A\right)_{nn} \qquad (23$$

This expectation value, however, is not the full expectation value but accounts only for the j^th^ component of the system. As previously said, this is obtained by the sum over all the possible values weighed for their probability p^j.

$$\langle\hat{A}\rangle = \sum_{j=1}^{N} p^j \sum_n \left(\rho^j A\right)_{nn} = \sum_n \left(\left(\sum_{j=1}^{N} p^j \rho^j\right) A\right)_{nn} = \sum_n (\rho A)_{nn} = T\mathit{R}(\rho A) \qquad (24$$

This equation allows us to compute the expectation value for any given operator, referring only to the density matrix. The other requirement for a full quantum mechanical description of the system is the treatment of the time evolution. This arises from the Schrodinger equation in the wave function formalism (52). To obtain the equivalent for the density matrix, we start by writing a single density matrix element in the basis representation (as defined in eq 17)

$$\rho_{n,m} = \sum_s \rho_s \, c_m^{s*} c_n^s = \langle c_m^{s*} c_n^s \rangle \qquad (25$$

For the time dependence, it is enough to take the time derivative using the chain rule (52).

$$\dot{\rho} = \sum_s \frac{d\rho_s}{dt} c_n c_m^* + \sum_s p_s \left(\frac{dc_n}{dt} c_m^* + c_n \frac{dc_m^*}{dt} \right) = \sum_s \frac{dp_s}{dt} c_n c_m^* - \frac{i}{\hbar} \left[\hat{H} \, , \rho \right]_{nm}$$

$$(26$$

The equation obtained describes the time evolution of a quantum system in the density matrix formalism. The equation contains two terms. The second term is quantum mechanical and is related to the Liouville-von Neumann equation, 19, while the first term is responsible for dephasing and population relaxation. In 2DES spectra this term is the one responsible for the disappearance (damping) of oscillations for long population times.

2.2 SYSTEM-FIELD INTERACTION

The interaction between the electric field and the molecular system can be seen most readily by treating the electromagnetic field with a classical approximation, while treating the system quantum-mechanically. Assuming the system to be a point dipole (52), the system field interaction can be written (54).

$$\hat{H}_{st} = -E(r,t)V \qquad (27$$

Where V is the operator describing the dipole-dipole interaction, previously described in paragraph 1.4.1.1, and E is the time-space dependent electric field. It is described as a sum of all the incoming fields.

$$E(r,t) = \sum_j (E_j(t)e^{-i\omega t+ik_jr} + E_j^* e^{i\omega_j t-ik_jr}) \qquad (28$$

In equation 28, $E_j(t)$ denotes the temporal field envelope and $*$ indicates its complex conjugate. Assuming a weak electric field, the perturbation due to the system-field interaction can be seen as a perturbation to an equilibrium density matrix $\rho(0)$.

The third order of the polarization P measured by our nonlinear optical experiment can be derived using the density matrix formalism discussed above. In this paragraph we are going to do that by looking at how a quantum mechanical system interacts with an external electric field. We start with the Liouville-van Neumann equation inserting the Hamiltonian containing the static and the perturbation contribution.

$$\dot{\rho} = -\frac{i}{\hbar}[H,\rho] = -\frac{i}{\hbar}[H_0,\rho] - \frac{i}{\hbar}[H_{st}(t),\rho] \qquad (29$$

To solve the equation 29 it is convenient to switch to the Liouville space notation (31), to treat the density matrix as a vector and thus simplify the discussion;

$$\dot{\rho}(t) = -\frac{i}{\hbar}L\rho + L_{st}(t)\rho \qquad (30$$

The density matrix can then be expanded in a series as (55)

$$\rho(t) = \rho^{(0)}(t) + \rho^{(1)}(t) + \rho^{(2)}(t) + \rho^{(3)}(t) + \cdots \qquad (31$$

By combining these two equation, equation 30 can be solved and the solution for an *n*-th order term is obtained.

$$\rho^{(n)}(t) = \left(\frac{1}{\hbar}\right)^{n} \int_0^\infty dt_n \int_0^\infty dt_{n-1} \dots \int_0^\infty dt_1\, E(r, t - t_n) E(r, t - t_n - t_{n-1}) \dots$$
$$\times\, \mathrm{E}(r, t - t_n - t_{n-1} - \cdots - t_1) G(t_n) \mathcal{V} G(t_{n-1}) \mathcal{V} \dots G(t_1) \rho(-\infty)$$

(32

The time scale in this equation in expressed as the time interval between pulse interactions (see below for the time sequences used in our experiments).

In 32 *G*(*t*) is the Liouville space Green function and describes how the system behaves between two interactions induced by the electric field.

$$G(t) = \theta e^{-\frac{i}{\hbar} L_o t}$$

(33

$\mathcal{V}$ is the superoperator of the transition dipole moment in the Liouville space and it is related to the density matrix by the equation

$$\mathcal{V}\rho = [V, \rho]$$

(34

As we have demonstrated in paragraph 2.1, the expectation value of the polarization can be calculated using the density matrix formalism

$$\langle P(\vec{r}, t) \rangle = Tr\{V \rho(t)\} = \langle\langle V | \rho \rangle\rangle$$

(35

We can use this equation to write the *n*th-order polarization as a convolution between the *n* electric fields and the *n*th-order nonlinear response function, for a set of time variables:

$$P^{(n)}(t) = \left(-\frac{i}{\hbar}\right)^n \int_0^\infty dt_n \int_0^\infty dt_{n-1} \dots \int_0^\infty dt_1\, E(t-t_n)\, E(t-t_n-t_{n-1}) \dots E(t- \ t_n - \cdots - t_1\ ) S(t_n, t_{n-1}, \dots, t_1) \qquad (36$$

The information relevant for the molecular system is contained in the response function $S(t_n, t_{n-1}, \dots, t_1)$ which can be expressed using the definition of the dipole operator and the invariance of the trace $\langle \dots \rangle$ to cyclic permutation (51). In this way the third order nonlinear response function, is expressed as a function of the dipole moment μ and the density matrix of the unperturbed system, $\rho\,(\infty)$. Stepping back to the Hilbert space representation it assumes the form (31)

$$S(t_n, \dots, t_1) = \left(-\frac{i}{\hbar}\right)^n \langle \mu(t_n + \cdots t_1)[\mu(t_{n-1} + \cdots + t_1), \dots [\mu(0), \rho(-\infty)] \dots]\,\rangle \quad (37$$

The response function only exists in the range of the positive time t_n and the interactions at times 0, t_1, … and $t_{n-1}+\dots+t_1$ are responsible for the generation of off diagonal non-equilibrium elements in the density matrix, leading to light emission. Writing the commutator explicitly, we obtain 2^n terms each of which describe a different sequence of interactions acting on the ket or on the bra side of the density matrix (which may be represented by on the left or on the right side of the Feynman diagram respectively – see below). Between the terms obtained from this permutation there are pairs of terms that are the complex conjugate of each other. As a result of this, expanding the commutator for a 3rd order nonlinear response we get terms referring to parts of the response function called “rephasing” and “non-rephasing”. As mentioned above the difference between these can be useful in assigning oscillations in 2DES.

$$
\begin{aligned}
&\langle \mu(t_3+t_2+t_1)\,[\mu(t_2+t_1),[\mu(t_1),[\mu(0),\rho(-\infty)]]]\rangle = \\
&= \langle \mu(t_3+t_2+t_1)\mu(t_2+t_1)\mu(t_1)\mu(0)\rho(-\infty)\rangle && \Rightarrow R_4 \\
&- \langle \mu(t_3+t_2+t_1)\mu(t_2+t_1)\mu(t_1)\rho(-\infty)\mu(0)\rangle && \Rightarrow R_1^* \\
&- \langle \mu(t_3+t_2+t_1)\mu(t_2+t_1)\mu(0)\rho(-\infty)\mu(t_1)\rangle && \Rightarrow R_2^* \\
&+ \langle \mu(t_3+t_2+t_1)\mu(t_2+t_1)\rho(-\infty)\mu(0)\mu(t_1)\rangle && \Rightarrow R_3 \\
&- \langle \mu(t_3+t_2+t_1)\mu(t_1)\mu(0)\rho(-\infty)\mu(t_2+t_1)\rangle && \Rightarrow R_3^* \\
&+ \langle \mu(t_3+t_2+t_1)\mu(t_1)\rho(-\infty)\mu(0)\mu(t_2+t_1)\rangle && \Rightarrow R_2 \\
&+ \langle \mu(t_3+t_2+t_1)\mu(0)\rho(-\infty)\mu(t_1)\mu(t_2+t_1)\rangle && \Rightarrow R_1 \\
&- \langle \mu(t_3+t_2+t_1)\rho(-\infty)\mu(0)\mu(t_1)\mu(t_2+t_1)\rangle && \Rightarrow R_4^*
\end{aligned}
$$

(38

As equation 38 shows,R_1^* R_2^* $R_3^*$and $R_4^*$are the complex conjugate of R_1 , R_2, $R_3$and R_4. The terms belonging to the rephasing response are ; R_1, R_3, R_1^* , while the non rephasing terms are R_1,R_2 and R_2^*. Basically, each of these terms corresponds to a sequence of interactions that can be drawn graphically using the double-side Feynman diagrams. In the next paragraphs, I will illustrate the basic rules of drawing Feynman diagrams and their use in 2DES interpretation.

2.3 FEYNMAN DIAGRAM RULES

The drawing of Feynman diagrams derives from taking separately each term of the commutator expansion (equation 38) to create the corresponding diagram, using specific rules. Two vertical lines represent the time evolution of the ket (left line) and bra (right line) of the density matrix, with time running from the bottom to the top. The interactions between the density matrix and the electric field are indicated by arrows acting either on the bra or ket side pointing towards or away from the system corresponding to an absorption or an emission. The ket and bra side of the diagram are the complex conjugate of each other and the last emission is always from the ket side, by convention. There is a conceptual distinction, however, between the last interaction and the others as the first interactions are responsible for the perturbation of the system and the last one originates from the n^{th} order molecular polarization.

$$P^{(n)} = \langle \mu\rho^{(n)}(t)\rangle$$

(39

This difference is generally indicated using a dashed arrow in the Feynman diagram (Figure 19).

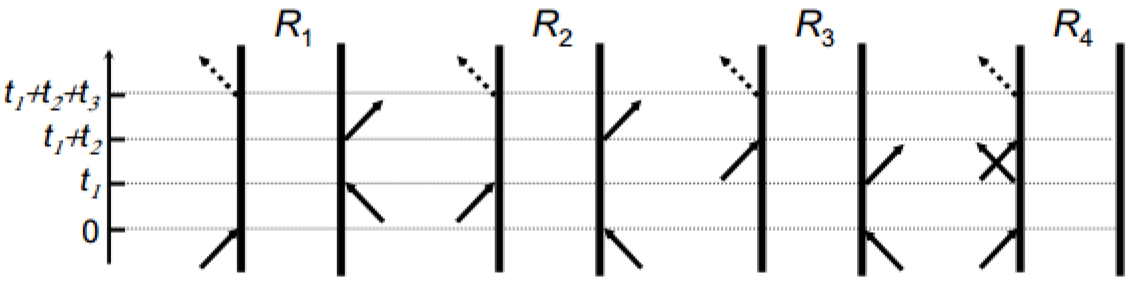

FIGURE 19 (52)*THE FIGURE SHOWS SOME EXAMPLES OF FEYNMAN DIAGRAMS. AS CAN BE SEEN FROM THE PICTURE, THE TIME IS DISPLAYED ON THE LEFT OF THE DIAGRAM AND THE INTERACTIONS BETWEEN THE LIGHT AND THE SYSTEM ARE INDICATED BY ARROWS POINTING TOWARD OR AWAY FROM THE SYSTEM. THE LAST ARROW REPRESENTS THE SIGNAL RECORDED AND IT IS DASHED BECAUSE IN CONTRAST TO THE OTHERS IT DOES NOT COME FROM AN INTERACTION BETWEEN THE LIGHT AND THE SYSTEM BUT FROM AN EMISSION.*

In figure 19 an arrow pointing to the right represents an electric field with $e^{-i\omega t+ikr}$ while the interactions pointing to the left side represent an electric field with $e^{+i\omega t-ikr}$. This takes account the rule that the final effect of the electric field interaction must end in a population state. The use of the rule $(-1)^n$ with n indicating the number of interactions on the bra side determines the diagram's sign. The last interaction detected has a frequency and wave vector which are the sum of the input frequency and wave vectors.

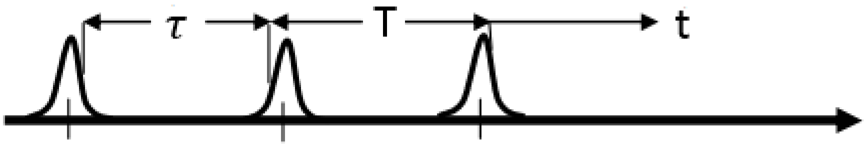

FIGURE 20 THE FIGURE ABOVE SHOWS THE ORDER IN WITH WHICH PULSES INTERACT WITH THE SYSTEM IN OUR EXPERIMENTS. THE RANGE OF TIMES IS LABELLED ACCORDING WITH THE PREVIOUS FORMULAS AND THE FOLLOWING DESCRIPTION

Once the Feynman diagrams rules are clear, we can start drawing them. For a third order nonlinear process, there are eight Feynman diagrams possible. Only six of them, however, are usually contemplated because the other two are not measureable from our apparatus. The molecular system starts out in equilibrium, i.e., ground state with $\rho = |0\rangle\langle 0|$. After that the first pulse hits the system at time $t = 0$, (Figure 20) an off-diagonal element ρ_{10} is generated producing a state of coherence in the system. The system starts to oscillate with a frequency of ω_{01} over time τ with dephasing with T_2.

$$\rho_{10} \propto i\mu_{01} e^{-i\omega_{01}\tau} e^{-\frac{\tau}{T_2}} \qquad (40$$

At time $t = \tau$ a second pulse hits the system leading to a population state. During this span of time the system experiences population relaxation expressed by the term e^{-T/T_1}.

$$\rho_{11} \propto i\mu_{01}^2 e^{-i\omega_{01}\tau} e^{-\tau/T_2} e^{-T/T_1} \qquad (41$$

The last pulse hits the system at time $t = \tau + T$ switching the system back to a coherence state, which then propagates and dephases during time period t.

$$\rho_{10} \propto i\mu_{01}^3 e^{-i\omega_{01}\tau} e^{-\tau/T_2} e^{-T/T_1} e^{-i\omega_{01}t} e^{-t/T_2} \qquad (42$$

Finally at time $t_d = \tau + T + t$, the third order non-linear response function that is responsible for the third order macroscopic polarization is recorded as the third order electric field.

The signal obtained is proportional to $Tr[\mu_{01}\rho]$.

$$R_1(t_1, t_2, t_3) \propto i\mu_{01}^4 e^{-i\omega_{01}\tau} e^{-\frac{\tau}{T_2}} e^{-\frac{T}{T_1}} e^{-i\omega_{01}t} e^{-\frac{t}{T_2}} \qquad (43$$

Following this procedure it is possible to write down all the others Feynman diagrams. The sequence of coherence for R_3 and R_4 are the same as those of R_2 and R_1, respectively.

The detection of the third-order response function can differ enormously depending the way in which the measurement is conducted and the information is extracted. In our case, the 2DES experiment was built with a beam geometry known as *box-CARS* in which all the input laser pulses have different wavevectors and the third-order response function is detected in the phase matched direction. In order to switch the detection between rephasing and non-rephasing signals, the time order of the 1st and 2nd pulses is inverted. The rephasing diagrams R^*_2, R_4 and R_1 are all emitted in the $-\vec{k}_1 + \vec{k}_2 + \vec{k}_3$ direction and cannot be separated further by phase matching. The same can be said for the non-rephrasing diagram R_2,R_3 and R^*_1 that are emitted in the $+\vec{k}_1 - \vec{k}_2 + \vec{k}_3$ .direction. For systems involving only one excited state, the diagrams R^*_1 and R^*_2 are neglected from equations 44 and 45 because their pathways involve two excited levels.

$$R_{reph} = R_2^* + R_4 + R_1$$ (44

$$R_{non-reph} = R_1^* + R_2 + R_3$$ (45

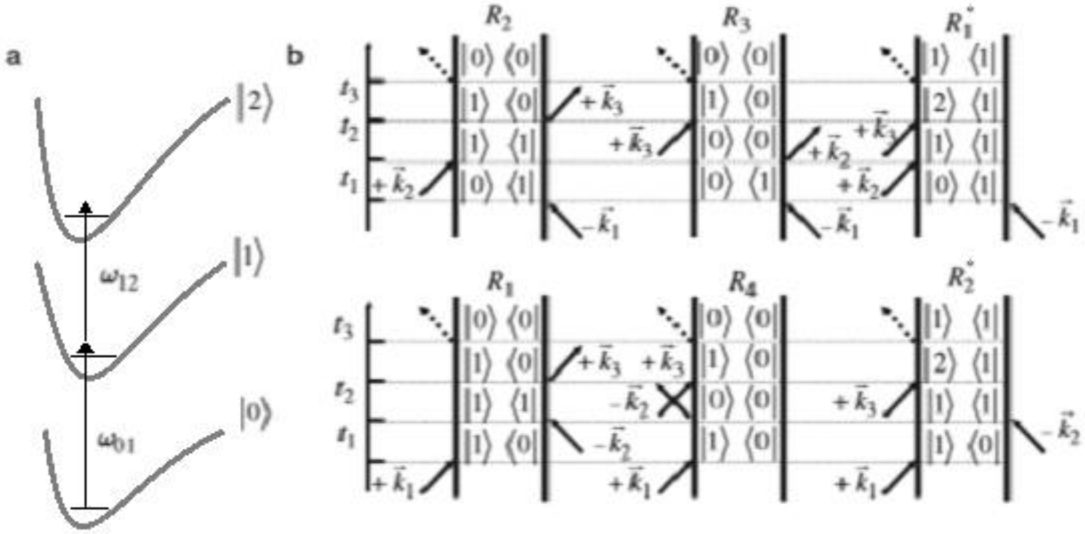

Figure 21 In the figure are shown on the top and bottom row the rephasing and non-rephasing diagrams respectively for a third-order nonlinear spectroscopy. (39)

2.4 HETERODYNE DETECTION

The heterodyne or interferometric detection method is a widely used way in which to record the signal in 2D apparatus. The measurement requires the recording of the signal spatially overlapped with a local oscillator (LO). In the frequency domain, the measurement is thus of the square modulus of the sum of the two fields.

$$I(\tau_0, T_0, \omega_t) = \left|E_{LO}(\omega_t)e^{i\omega_t \Delta t} + E_{sig}\left(\tau_{0,}T_0, \omega_t\right)\right|^2 = \ |E_{LO}(\omega_t)|^2 + E^*_{sig}\left(\tau_{0,}T_0, \omega_t\right)E_{LO}(\omega_t)e^{i\omega_t \Delta t} + E_{sig}(\tau_0, T_0, \omega_t)E^*_{LO}(\omega_t)e^{-i\omega_t \Delta t} + \left|E_{sig}(\tau_0, T_0, \omega_t)\right|^2 \qquad (46$$

The first and last homodyne terms are not relevant for the measurement for different reasons; the $|E_{LO}(\omega_t)|^2$ term can be measured and easily subtracted, while the $\left|E_{sig}(\tau_0, T_0, \omega_t)\right|^2$ term has an amplitude too low compared to other components, and can be ignored (56). The two other terms are the interferometric signal and can be written as;

$$2Re\left[E_{sig}(\tau_0, T_0, \omega_0)E_{LO}(\omega_t)\right] cos\left(\Delta\Phi(\omega_t)\right) \qquad (47$$

Equation 47 contains the relative phase between the two fields. Using a reference field (52), we can obtain the total characterization of the field and so separate the real from the imaginary part. The use of the heterodyne signal instead of the homodyne one leads to some important advantages in the measurement. First, as mentioned above, the possibility of separating the emitted field into its imaginary and real parts. Second, the simultaneous propagation of two electric fields enhances the low amplitude of the signal by mixing its contribution with the stronger LO electric field.

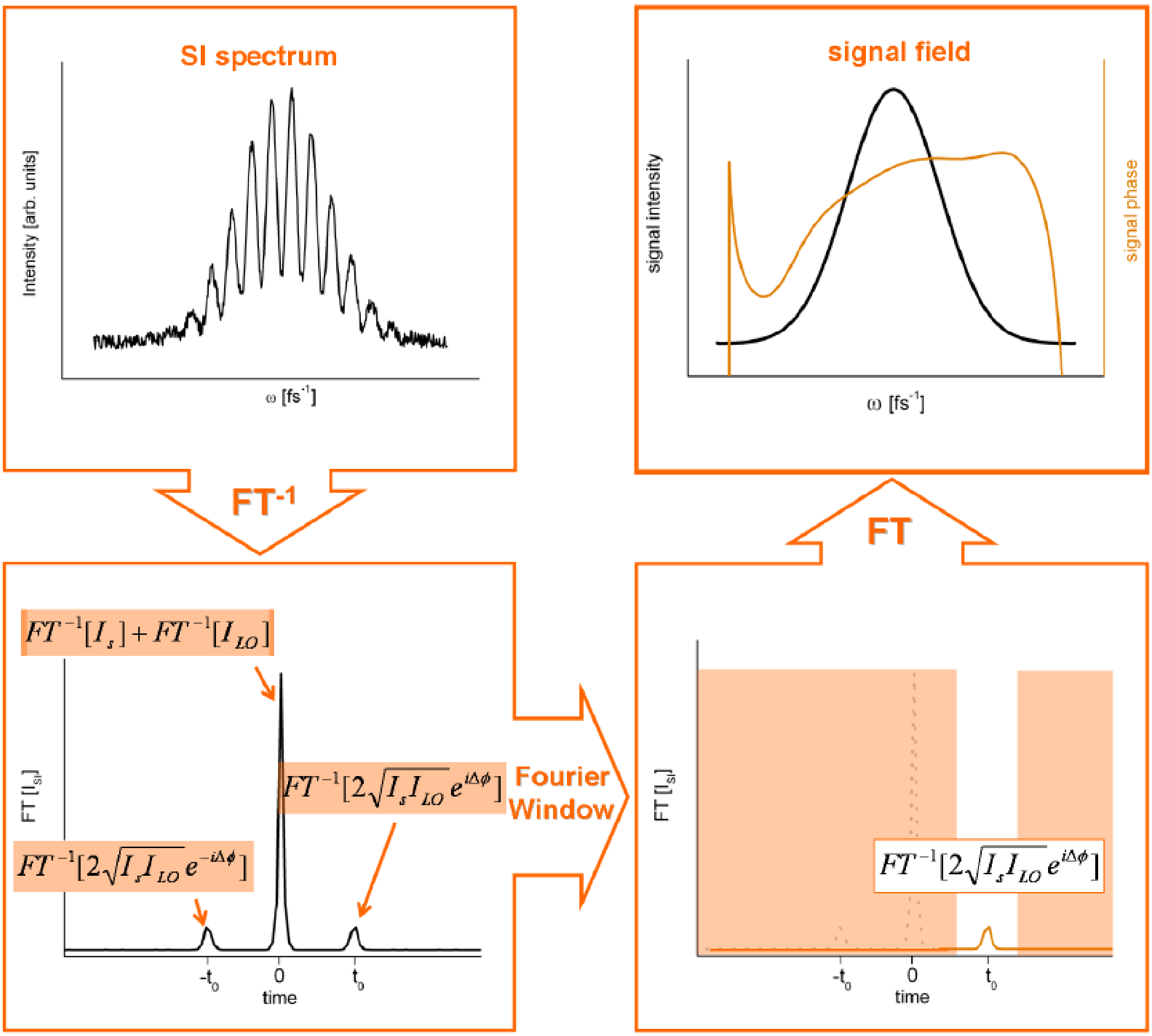

Figure 22 The figure above shows how the heterodyne signal is elaborated through the Fourier transform process. In the time domain, the homodyne values lie at time equal to zero, while the two heterodyne terms are distant from time zero for a value equal to Δt (see equation 46). The Fourier window separates one of the heterodyne contributions from the others terms. The real and the imaginary part are then obtained by Fourier transforming back the heterodyne contribute isolated.

2.5 LINE SHAPE FUNCTION

In principle many interactions contribute to the electronic response function. In order to simplify the system considered, we focus on a two-level electronic system. Moreover, the Born-Oppenheimer approximation is made so the electronic and nuclear degrees of freedom are considered separated. We also allow that the equilibrium nuclear position is different between the excited and the ground state (57) (58) (Figure 23).

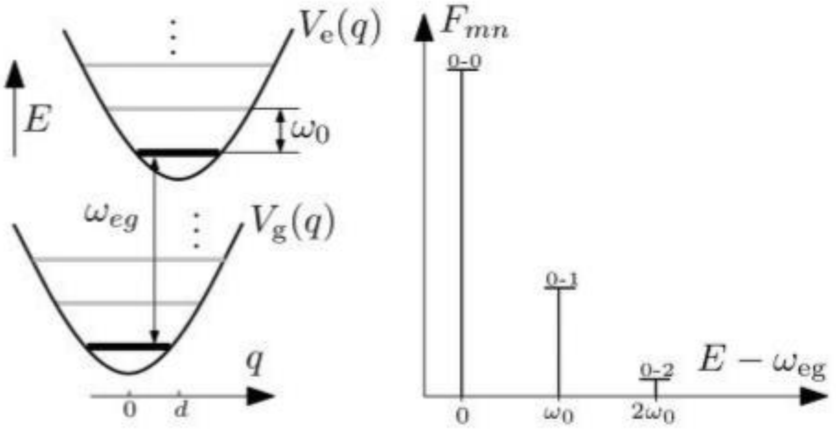

FIGURE 23. THE FIGURE SHOWS THE MODEL USED FOR THE LINE SHAPE DISCUSSION. THE SYSTEM INVOLVES TWO HARMONIC OSCILLATORS WITH SHIFTED EQUILIBRIUM (LEFT). ON THE RIGHT, A GRAPH ILLUSTRATES THE FRANCK- CONDON OVERLAP CORRESPONDING TO DIFFERENT TRANSITIONS FROM THE GROUND V=0 TO DIFFERENT VIBRATIONAL LEVELS OF THE EXCITED STATE. THE FIGURE AND PART OF THE FOLLOWING DISCUSSION ARE FROM THE ARTICLE OF VYTAUTAS ET AL. (53)

In this system, the electronic excitation is a Franck Condon transition. Once the molecule arrives in the excited state, the system is not at equilibrium (i.e. a displaced oscillator) and it needs to relax by dissipation of energy. The one dimensional electronic potentials of the ground and the excited state are described in the harmonic approximation by , $V_g(q) = \hbar\omega_0\, q^2/2$ and $V_e(q) = \omega_{eg} + \hbar\omega_o(q-d)^2/2$, respectively. Here ω_0, expresses the vibrational frequency, ω_{eg} the energy gap between the ground and the excited state and d the dimensionless displacement parameter that is responsible for the strength of the electron coupling. In fact, d is inversely proportional to the Huang-Rhys factor used to quantify the coupling strength (53). In this case, the corresponding energy is $E_m = \hbar\omega_0(m + 1/2)$ for an infinite set of wave functions$|\Psi\rangle$. The absorption spectrum for this ideal case results from transitions between these levels weighted by the Franck Condon factor.

$$k_{abs}^{FC}(\omega) \propto \omega \sum_{m,n=0}^{\infty} e^{-\frac{m\omega_0}{k_B T}} |F_{mn}|^2 x\, Re \int_0^{\infty} dte^{i(\omega-\omega_{eg})t-i\omega_0(n-m)t-\Upsilon t} \qquad \text{(48}$$

Where Υ is a phenomenological parameter responsible for the line-broadening and F_{mn} is the Franck Condon factor that expresses the overlap between the wave functions of the two vibrational levels in the transition.

In order to understand the spectral broadening, however , it is important to add more details to the phenomenological parameter ϒ. On including the medium (or bath) in the model the excited state energy has fluctuations due to the interaction with the low-frequency bath modes. The most convenient way to describe the fluctuations induced by the bath is the correlation function.

$$C(t) = Tr_B\{Q_e(t)Q_e(0)\rho_{eq}\} \qquad \text{(49}$$

Where ρ_{eq} is the density operator of the bath and $Q_e(t)$represents the collective coordinates of bath fluctuations. Fourier transforming the correlation function, we obtain two real functions, in the frequency domain (53).

$$C(\omega) = \int_{-\infty}^{\infty} dte^{i\omega t}\, C(t) \equiv C'(\omega) + C''(\omega) \qquad \text{(50}$$

$where\ C'(\omega)$ and $C''(\omega)$ are even and odd functions of ω. The C'' is temperature independent and is more commonly called the spectral density. The relation between these two functions is express by the fluctuation- dissipation theorem;

$$C'(\omega) = \coth(\beta\hbar\omega/2)C''(\omega) \qquad \text{(51}$$

Now, that we have defined the system and its correlation function, it is possible to calculate the shape of the electronic transition bands via the line shape functions. The absorption coefficient is then expressed by the equation;

$$k_{abs}^{C}(\omega) \propto \omega Re \int_{0}^{\infty} dt e^{i(\omega-\omega_0)t-g(t)} \qquad (52$$

Where $g(t)$ is the line shape function expressed by an integral including the correlation function of the system-bath fluctuation.

$$g(t) \equiv -\frac{1}{2\pi}\int_{-\infty}^{\infty} d\omega \frac{c(\omega)}{\omega^2}[exp(-i\omega t) + i\omega t - 1] \qquad (53$$

The correlation function can be expressed as a distribution of vibrational frequencies coupled with the bath so introducing the density of Huang-Rhys, $\{s_\alpha\} \rightarrow s(\omega)d\omega$, as a parameter that takes into account the vibronic frequency, we can indicate what are the dominant vibrational normal-modes in the transition at frequency ω_0.

$$C''(\omega) = \pi\hbar^2\omega^2[s(\omega) - s(-\omega)] \qquad (54$$

For a system-bath coupling described by a Lorentzian distribution, the spectral density obtained is then

$$C''_L(\omega) = \lambda\mu \frac{2\omega\omega_0\Upsilon}{\left(\omega^2-\omega_0^2-\Upsilon^2\right)^2+4\omega^2\Upsilon^2} \qquad (55$$

While in the Gaussian distribution

$$C''_G = \lambda\mu \frac{\sqrt{\pi}}{\sqrt{2}\Upsilon}\left[e^{-\frac{(\omega-\omega_O)^2}{2\Upsilon^2}} - e^{-\frac{(\omega-\omega_O)^2}{2\Upsilon^2}}\right] \qquad (56$$

where λ is called the reorganization energy, Υ the damping parameter and ω_0 the vibrational frequency. The reorganization energy expresses how strongly the system is coupled with the bath modes while Υ gives an indication about how rapidly the correlation function decays with time.

Equation 55 recognizes two different cases depending on relative values of Υ and ω_0; the underdamped and the overdamped. The underdamped case occurs when $\Upsilon<\omega$ and typically describes intramolecular interactions. It is related to the overlapping between the wave functions of the ground state and the excited state and shows fluctuations in the line shape function for transitions different from 0-0, i.e. it reflects vibronic interactions. In our work, the underdamped case was largely neglecting because the study in Chapter 4 was focused on intermolecular (solvent-solute) interactions described by the overdamped limit $\Upsilon>\omega$. This assumption was reasonable because our experimental measurements showed mainly the spectral diffusion. The overdamped regime assumes the bath acts as a continuum of low frequency modes interacting with the molecular system in its excited state (59). In this case the correlation function can be described by an exponential decay whose Fourier transform is the even part, $C'(\omega)$, of the total quantum correlation function. In the high temperature limit, the spectral density can then be obtained by using equation 51.

$$C''(\omega) = \frac{2\lambda\Upsilon\omega}{\omega^2+\Upsilon^2} \qquad (57$$

For a better fitting of some systems, the spectral density can be described by a Gaussian distribution for an overdamped limit. In this case equation 56 becomes;

$$C''_G(\omega) = \frac{2\lambda\omega}{\sqrt{2\pi}\omega_g} exp\left(-\frac{\omega^2}{2\omega^2}\right) \qquad (58$$

2.5.1 The Use of line shape function in 2DES simulation

The program used to simulate the 2DES spectra was obtained by using the relation 53 that links the line shape function to the correlation function. Line shape functions $g(t)$ can then be written for different time ranges and used to express the terms of the rephrasing and non-rephrasing response (60) (51).

$$\begin{aligned}
R_1(t_3,t_2,t_1) &= -\left(\frac{i}{\hbar}\right)^3 \mu^4 e^{-i\omega(t_1+t_3)} e^{-g(t_1)-g(t_2)-g(t_3)+g(t_1+t_2)+g(t_2+t_3)-g(t_1+t_2+t_3)} \\
R_2(t_3,t_2,t_1) &= -\left(\frac{i}{\hbar}\right)^3 \mu^4 e^{-i\omega(t_3-t_1)} e^{-g(t_1)+g(t_2)-g(t_3)-g(t_1+t_2)-g(t_2+t_3)+g(t_1+t_2+t_3)} \\
R_3(t_3,t_2,t_1) &= -\left(\frac{i}{\hbar}\right)^3 \mu^4 e^{-i\omega(t_3-t_1)} e^{-g(t_1)+g(t_2)-g(t_3)-g(t_1+t_2)-g(t_2+t_3)+g(t_1+t_2+t_3)} \\
R_4(t_3,t_2,t_1) &= -\left(\frac{i}{\hbar}\right)^3 \mu^4 e^{-i\omega(t_1+t_3)} e^{-g(t_1)-g(t_2)-g(t_3)+g(t_1+t_2)+g(t_2+t_3)-g(t_1+t_2+t_3)}
\end{aligned}$$

(59

For a two level system, rephasing and non-rephasing terms are summed as in equation 44 and 45 in the time domain. The response function obtained is proportional to the third order polarization and so to the measured signal. The third order response signal is then calculated including the response function by the equation:

$$S^{(3)}(\omega_1,t_2,\omega_3) = \int_{-\infty}^{\infty} dt_1 \int_{-\infty}^{\infty} dt_3\, R^{(3)}\left(t_{1,}t_2,t_3\right) exp(i\omega_1 t_1) exp(i\omega_3 t_3)$$

(60

This allows us to simulate the measured 2DES.

3. EXPERIMENTAL

3.1 LASER SYSTEM

Our laser setup is based on a commercial amplified laser system and a commercial noncollinear parametric amplifier (NOPA). The amplifier is a regenerative Ti:Sapphire system (Spectra Physics Spitfire ACE pumped by an Evolution laser and seeded by MAITAI oscillator) and generates pulses of 120 fs centered at 800 nm with energy of 500 µJ at a rate of 10 kHz. Almost all of the power from the amplified is used to pump the NOPA system (TOPAS White, Light Conversion). The pulses that come out from the NOPA have a width of 15 fs and can be tuned with their central wavelength in the range from 490 nm to 750 nm. In addition to the internal compressor in the NOPA there is also a second prism compressor that helps to remove chirp from the pulses. The NOPA output a typical power at 550 nm of 400 mW (40 µJ per pulse at 10 kHz). A neutral density filter is used to reduce the power to avoid optical damage to the sample . The power entering into the 2D setup is then fixed at around 4 mW. The pulse fluctuation of the NOPA system is typically below 0.5% rms for the central wavelength of the spectrum.

3.2 DESCRIPTION OF THE EXPERIMENTAL SETUP

At UEA we implemented a 2DES scheme based on a setup originally proposed by Brixner which utilizes beam splitters rather than a diffractive optic (Figure 24). The main problem in any 2DES experimental setup is to maintain the phase stability of the laser pulses during the measurement. Small vibrations of optical elements generate small fluctuations in the beam's pathway and so induce phase fluctuations. To overcome this problem, the experimental setup was designed in a pairwise manner so that path length fluctuations become anticorrelated and compensate each other (61). On entering the experimental setup, the laser beam is split by the first beam slitter (BS1) into two phase coherent beams at different heights. The two beams are separated by 2.5 cm and are kept as close as possible to the optical table in order to avoid phase errors due to large angular oscillations. The upper and the lower beams are then further split generating beams c and LO and beams a and b, respectively. After the first beam splitter the upper beam goes through the first delay stage, responsible for generating the population delay.

In the initial alignment the delay is set at 2.5 cm in order to compensated the extra distance traveled by the lower beam and thus to make the arrival of the two pulses at the sample time coincident. The second beam splitter BS2 then divides the two pulses a second time, leading to four phase coherent beams in a “box” geometry where each of them is separated from the other by 2,5 cm. The beams a and c are steered towards the second delay stage, and the beams b and LO have to travel an extra distance to compensate the extra path taken by those two beams. The four pulses hit a spherical mirror (SM) that focuses them to a common spatial position. Eventually, the folding mirror, FM, sends the beams out of the optical setup towards the sample. There are two choppers in the setup which remove both the pump-probe contributions and any scattered light contributions which exist in the same direction as the LO beam. To achieve this chopper C1 modulates beam b, the chopper C2 modulates beam c. The sample is positioned where the pulses meet spatially and temporally. After the sample, all the beams except for the local oscillator are blocked. The local oscillator is collimated and directed into the spectrometer. This spectrophotometer contains a highly dispersive prism which spatially disperses the wavelengths that are then sent through a lens onto a CCD camera

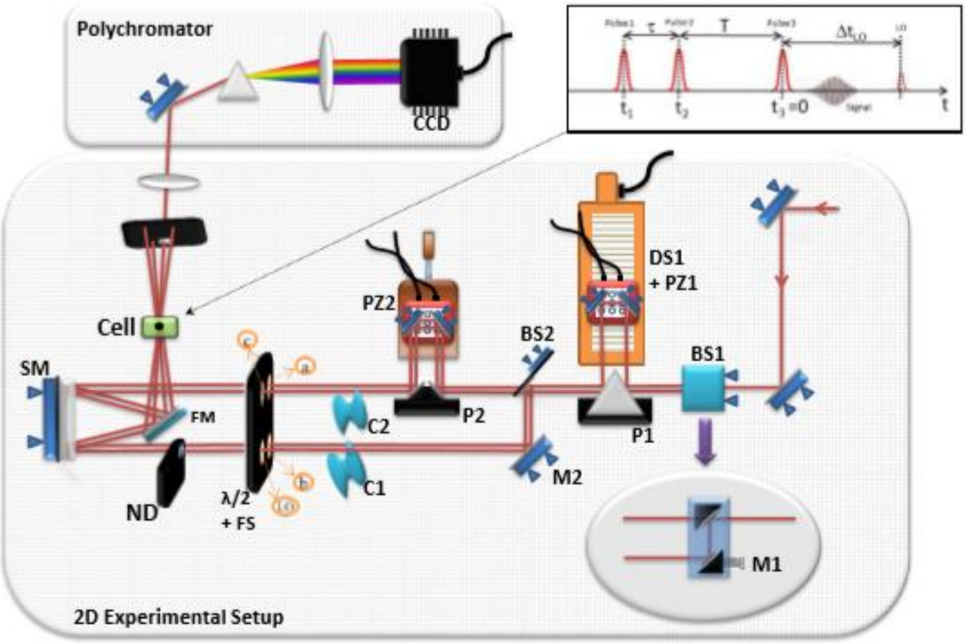

FIGURE 24 (62) *IN THE TOP ON THE RIGHT, THE PULSES SEQUENCE THAT GENERATES THE SIGNAL IS ILLUSTRATED WITH THE COHERENCE T, POPULATION T AND DETECTION ΔT_LO TIME DELAYS INDICATED. THE PICTURE ALSO SHOWS THE EXPERIMENTAL SETUP PRESENT IN OUR LABORATORY. AS CAN BE SEEN, THE LASER ENTERS IN THE SYSTEM ON THE TOP RIGHT AND IT IS DIRECTED INTO THE*

OPTICAL SYSTEM. THE DELAY DS1 MOVES PULSES LO AND C AND IT IS RESPONSIBLE FOR THE POPULATION DELAY, WHEREAS PZ2 MOVES PULSES A AND C AND IS RESPONSIBLE FOR THE COHERENCE DELAY

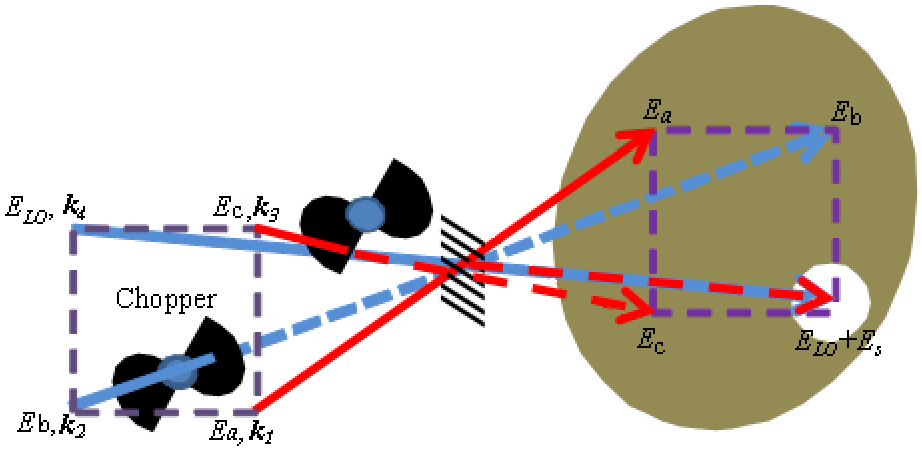

FIGURE 25 (62)THE PICTURE SHOWS THE BOX GEOMETRY PRESENT IN THE EXPERIMENTAL SETUP AFTER AND BEFORE PULSES HIT THE SAMPLE.

3.3 DELAY STAGE MOVEMENT SEQUENCES

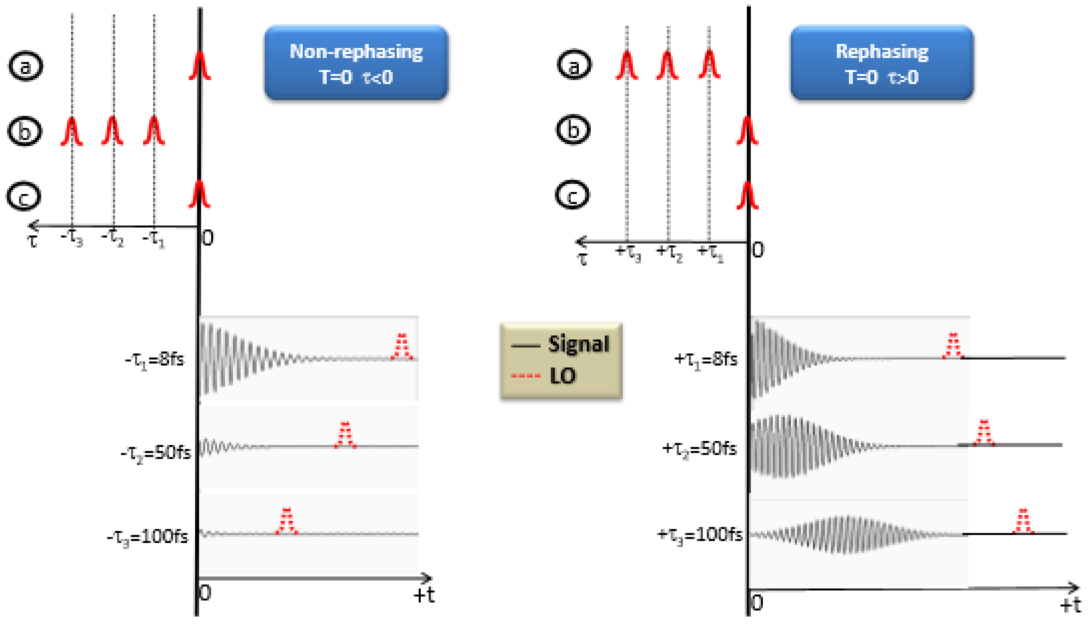

FIGURE 26 (62) PULSE ARRIVAL TIME ORDERING SCHEME FOR REPHASING AND NON-REPHASING CASES.

For the initial alignment, pulses a, b, and c are overlapped with a fixed delay relative to LO, which arrives later by around 400 fs. The LO delay is illustrated in figure 26 for both rephasing and non-rephasing cases, depicting the LO pulse by a dashed line. The population time, *T*, is defined as the time interval between pulse a or b and pulse c. More generally it can be written as $T = t_c - t_n$, where *n* is the second to arrive between a and b. The coherence time is defined as $\tau = t_b - t_a$. In the rephasing case, the pulse order is a, b, c and according to its definition, τ has a positive value (Figure 26, right). On the other hand, τ is negative when the pulses order is b, a, c and the non-rephasing signal is being generated in the LO direction. This convention of monitoring time, however, still works for the detection timescale *t*, so in Figure 26 the coherence timescales were drawn to evaluate the early or the late arrival of pulses on the time scale *t* with a convention that time increases from the left to the right. To start the measurement the first step occurs in setting the population delay by moving delay DS1 that control the relative delay between the pairs of beams (a, b) and (c, LO) (see figure 24). Once the population time is settled, the measurement is performed by scanning over the coherence time, moving the relative delay between the pairs of pulses (a, b) with the delay stage PZ2. During the detection of the coherence time (delay between a and b), the delay between c and LO is also altered. In this way the delay between signal emission and the LO remains constant over the coherence time scan (62). For a scan of negative coherence times, the PZ2 delay is moved so that pulse b is the first to arrive. In the positive coherence time case, things are slightly more complicated. Now, to ensure the pulse order (a,b,c), we need to move PZ2 backwards. This will alter the delay between pulses c and b and therefore the population time. Thus, to ensure that pulse b will be the second to arrive, the delay stage PZ1 has also to be moved forward by the same amount that PZ2 is moved backwards (63). These delay stage movements guarantee the measurement of the signal in the rotating frame approximation (39). This can be clarified by looking at the equation that describes the signal phase:

$$I_{sig} \sim e^{-i(\Delta\varphi_{a,b}-\Delta\varphi_{c,LO})} e^{-i\omega(\tau-t)} = e^{-i\Delta\varphi_{a,b}} e^{i(\Delta\varphi_{c,Lo}-\omega\tau)} e^{i\omega t} \qquad \textit{(61}$$

Where $\Delta\varphi_{a,b} = \varphi_a - \varphi_b$ and $\Delta\varphi_{c,LO} = \varphi_c - \varphi_{LO}$. The LO phase can be also written as $\Delta\varphi_{c,LO} = \omega t_{LO}$. When the coherence delay changes by a positive amount $\tau' = \tau + \Delta\tau$, this lead to an opposite movement of the LO $t'_{LO} = t_{LO} - \Delta\tau$. Then, from equation (62) It is clear that the phase change generated from the coherence delay is exactly cancelled by the corresponding one of the LO.

$$I_{sig} \sim e^{-i(\Delta\varphi_{a,b}-\Delta\varphi_{c,LO})} e^{-i\omega(\tau'-t')} = I_{sig} \sim e^{-i(\Delta\varphi_{a,b}-\Delta\varphi_{c,LO})} e^{-i\omega(\tau+\Delta\tau-t-\Delta\tau)=} = I_{sig} \sim e^{-i(\Delta\varphi_{a,b}-\Delta\varphi_{c,LO})} e^{-i\omega(\tau-t)} \qquad (62$$

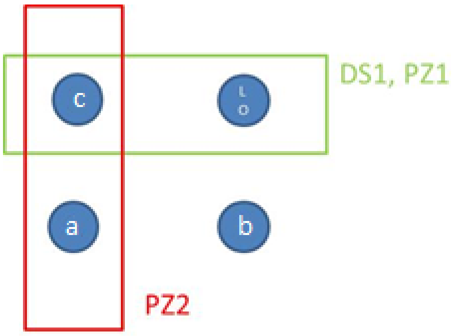

FIGURE 27 IN THE FIGURE IT IS SHOWN HOW THE TWO DELAYS PZ2 AND PZ1 MOVE THE PULSES.

3.4 PHASE STABILITY OF THE SETUP

Choosing a phase matched direction, the total phase for a heterodyne detected 2DES signal can be calculated. Taking, for instance, the rephasing direction $k_s = -k_a + k_b + k_c$ the overall phase fluctuation can be written as follows:

$$\Delta\varphi_s = -\varphi_a + \varphi_b + \varphi_c - \varphi_{LO} + \varphi_{sig} = (\varphi_b - \varphi_a) + (\varphi_c - \varphi_{LO}) + \varphi_{sig} \qquad (63$$

Where φ_{sig} is the phase produced by the interactions with the laser fields (64). Each beam produces a phase fluctuation so that the overall phase fluctuation can be written as follow:

$$\delta(\Delta\varphi_s) = (\delta\varphi_b - \delta\varphi_a) + (\delta\varphi_c - \delta\varphi_{LO}) \qquad (64$$

For the phase fluctuation of each beam, all the optical elements that are in its pathway contribute. Hence, looking at the picture Figure 24 we can write the equations for each beams showing explicitly all the phase contributions from the different optical elements (64). The first phase term, for instance, can be written as:

$$\delta\varphi_a = \delta\varphi_{BS1} + \delta\varphi_{M1} + \delta\varphi_{BS2L} + \delta\varphi_{PZ2+P2} + \delta\varphi_{SM} + \delta\varphi_{FM} \quad (65$$

Taking the respective differences of the above terms in eq (64) it results in:

$$\delta\varphi_b - \delta\varphi_a = \delta\varphi_{M2} - \delta\varphi_{PZ2+P2} \quad (66$$

$$\delta\varphi_c - \delta\varphi_{LO} = \delta\varphi_{PZ2+P2} - \delta\varphi_{M2} \quad (67$$

We can see that the fluctuations are anti-correlated, so the total phase fluctuation resulting from the sum of term (66) and term (67) is zero. The formula above does not consider single beam fluctuations due to air currents, which affects differently the different beam paths, and can become significant in some cases; for this reason the system is well protected from the environment. Even though the phase difference of the different beam pairs may fluctuate significantly, the anti-correlation ensures that the overall phase of the measured signal is significantly more stable (65).

3.5 PUMP-PROBE MEASUREMENT AND SCATTERED LIGHT REMOVAL

One problem influencing the 2DES measurement signal/noise is the light scattering contributions in the direction of the detection. In fact, the light scattering of pulses a,b, and c is phase coherent with the LO and the signal, leading to an additional unwanted interferometric detection (56). Beyond that, the use of the LO beam with a delay of around 400 fs from the other beams generates pump-probe contributions to the signal where the LO acts as a probe. In some setups, lock-in detection (66) and shutters (67) were proposed as solutions to overcome this problem, but both present some disadvantages. The use of shutters, for example, slows down the acquisition of the signal and does not allow for shot to shot subtraction. Our experimental setup is a good compromise between these two cases, using choppers acting as shutters has the advantage of synchronizing them with the detector and laser. The chopper system comprises two choppers, C1 and C2, that modulate beams b and c respectively. To explain the chopper sequences, we will refer to Figure 28.

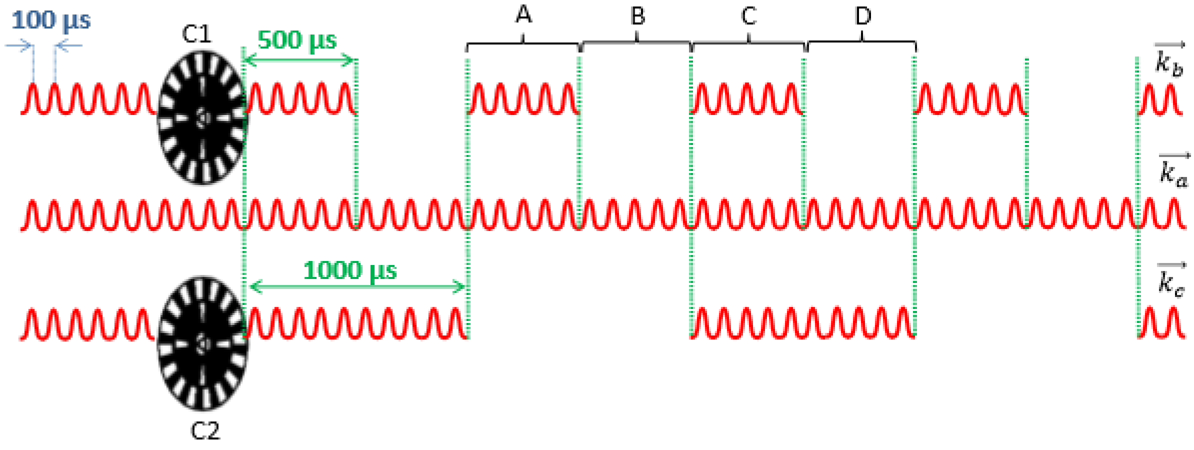

FIGURE 28 (62) *THE PICTURE ILLUSTRATES THE SAMPLE ILLUMINATIONS DUE TO DIFFERENT CHOPPER SEQUENCES USED. CHOPPER C1 ACTS ON BEAM B WITH A FREQUENCY OF 1 KHZ AND CHOPPER C2 ACTS ON BEAM C WITH A FREQUENCY OF 500 HZ.*

The fastest chopper is C1, is chosen to be at 1 kHz allowing transmission of bundles of 5 laser shots and to block the next 5 from the 10 kHz NOPA (62). Even though the chopper has the capability to operate at 5kHz, the presence of turbulence and the problem of partially blocking of the beams requires the lower rate. The partial blocking of the beams, however, is still persisting as a problem in the lower rate for the first and the last shot of the 5. Because the camera could be synchronized with the chopper, the problem was solved by recording only the three shots in the middle of the 5. Whereas the chopper C1 is synchronized with the laser at 1/10 of its rate making a cycle every 1 ms, the chopper C2 is slower with a frequency of 1/20 of the laser rate covering a cycle every 2ms. As a result of this, there are 4 beam configurations incident on the sample repeated over the time. For every couple of blocked-unblocked events of the beams b, Beam c will be once blocked (A and B cases) and once unblocked (C and D cases). The CCD camera is synchronized with the laser frequency and acquires the cases A, B, C and D separately. A software manipulated routine subtracts the different cases in the following order to manipulate these contributions.

$$\alpha = A - B = |S_a + S_b + E_{Lo}|^2 - |S_a + E_{LO}|^2 = |S_b|^2 + 2Re\{S_a S_b^*\} + 2Re\{S_b E_{LO}^*\}$$

(68

$$\beta = C - D = |S_a + S_b + S_c + E_s + E_{LO}|^2 - |S_a + S_c + E_{Lo}|^2 =$$

$$= |E_s|^2 + |S_b|^2 + 2Re\{S_a S_b^*\} + 2Re\{S_b E_{LO}^*\} + 2Re\{S_a E_S^*\} + 2Re\{S_b E_S^*\} + 2Re\{S_c E_S^*\}$$

$$+Re\{S_b S_c^*\} + 2Re\{E_S E_{LO}^*\}$$

(69

$$\alpha - \beta = |E_S|^2 + 2Re\{S_a E_S^*\} + 2Re\{S_b E_s^*\} + 2Re\{S_c E_s^*\} + 2Re\{S_b S_c^*\} + 2Re\{E_s E_{LO}^*\}$$

(70

The last term of the equation (70) is the signal heterodyned by the local oscillator, and it is what the our system would actually detect. Nevertheless, the other terms of the equation (70) because of their coherence with the LO are also detected but give a negligible contributions. The first three terms of equation (70) are related to pump-probe contributions between an nth pulse (a, b or c) and the LO beam and to the scattering of that beam in the direction of detection. Taking, for instance, the S$_a$ term and breaking it down into its two terms: $S_a = E_{Sa} + \delta E_a$ it can be seen that the two contributions are the electric field of the pulse a acting as a pump and the Rayleigh scattering of the same beam, both emitting along the LO direction. The term $2Re\{S_b S_c^*\}$ does not propagate its pump-probe contributions on the direction of detection, but it still contributes to the signal by Rayleigh scattering. Finally, the first term describes the homodyne signal and it significantly contributes to the signal. To avoid this main disturbing contribution, we apply during the spectra interferometry procedure a Fourier window to the signal's inverse Fourier transform (Figure 22). This results in having the signal separated in different contributions in the time domain (67) . The homodyne signal, which doesn't interfere with other beams, will be found at time *t* = 0, whereas the heterodyne signal generated by the interference between the homodyne and the LO will be found centered at *t* = LO. In addition to the selection between the homodyne and heterodyne signal, the Fourier windowing process also removes the light scattering contributions not centered in the correct delay time. It should be pointed out that some of the contributions in equation (70) located around *t* = LO persist for some population and coherence times, and cannot be removed by Fourier windowing process. However, these contributions are so small that their presence is negligible. After having considered the different terms of equation (70), it is important to stress again the improvement in the measurement introduced by the use of the second chopper. In fact, the term deleted by the subtraction; $Re\{S_b E^*_{LO}\}$ is a pump-probe term between pulse b and LO, and it is very significant for samples with strong transient absorption (62) . Another interesting advantage of the two chopper setup is that it allows the acquisition of the pump-probe and the LO signal during the measurement of 2DES spectra, and thus under very similar conditions (as opposed to in a separate later measurement). In order to understand better the recording process, it is important to refer back to figure 28. For the case B, beams b and c are blocked and the LO can be measured independently with a negligible light spattering produced by pulse a in its direction. The pump-probe signal is obtained by computing equation (68) that subtracts the LO contribute from the case which has the beam c un-blocked. Experimentally, it occurs with the motion of the DS1 delay, which has the function of making the relative motion between LO and pulse a. After the pump-probe measurement, the LO returns to its original position (~400 fs forward from the other beams) and a 2DES measurement can start by scanning the different coherence times. In a typical measurement, 100 coherence times and averaging over 1000 laser shots for each delay takes about 3 minutes. Therefore 20 2DES maps requires around 1 hour of measurement time.

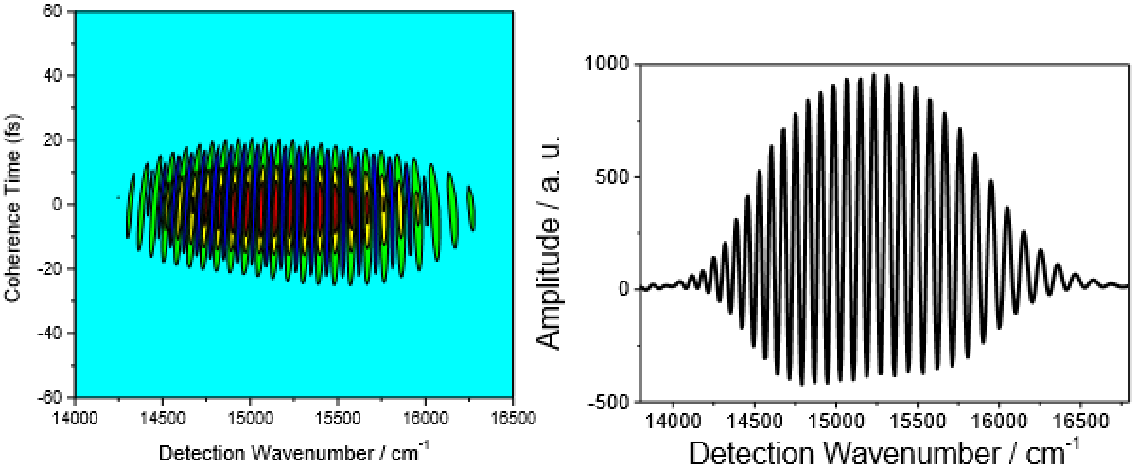

FIGURE 29 (62) THE FIRST PICTURE SHOWS A TYPICAL INTERFEROGRAM MEASUREMENT ACQUIRED BY THE 2DES SETUP. THE SECOND FIGURE IS THE HORIZONTAL CUT OF THE INTERFEROGRAM ALONG THE COHERENCE TIME T = 0.

4. RESULTS

In this chapter will be illustrated the main experimental results obtained concerning Chl a, first obtained with conventional spectroscopy and then with the newly developed spectrometer. The chapter will thus be divided in two parts. In the first part, we will discuss the results obtained for Chl a in the solvents of acetone and acetonitrile in presence of variable amounts of water, which will be discussed in terms of aggregate formation and self-quenching. In the second part we will analyze the solvent effect on the 2DES of the monomer Chl a using the data obtained by 2DES spectroscopy, and investigated through analysis of the response assuming the molecular system behaving as a Brownian oscillator (see section 2.5).

4.1 CHLOROPHYLL A CHEMICAL PHYSICAL CHARACTERIZATION

Here we mainly focus on linear spectroscopic studies in order to characterize a system to be analyzed later on with the 2DES spectroscopy. The main aim of this first part was to establish the condition necessary to make a system of chlorophyll aggregates reproducibly, producing low light scattering which is important to obtain good 2DES spectra. This would have allowed us to study the coupling, energy transfer and photophysics of aggregates of different sizes. This is relevant to light harvesting by plants in the photosynthetic process. The ideal condition would have been to find a way to have a relevant and controlled concentration of the Chl a dimer in solution. Unfortunately, this result wasn’t achieved because the system was found to be very unstable and highly dependent on the concentration of Chl a and the composition of the solvent. This has made impossible the proper characterization of Chl a complexes in solutions at the high concentration necessary for good 2DES measurements. In fact, in order to pursue a good chemical characterization the solutions were made in a concentration range appropriate for linear spectroscopy in a 1 cm cell (e.g. [Chla] ~ 2 µM). In contrast, the 2DES measurements require a 1 mm pathlength with a concentration of chlorophyll around 100 µM. However, we have identified a number of interesting and potentially significant results in these complicated multi-component solutions, and these form the topic of this section. The 2DES of Chl a – monomers in different solvents are investigated in section 4.2.

The criteria chosen for selecting the solvent studied were several. In the first instance a preliminary bibliographic research was done to find solvents mixtures that showed aggregate formation in the red region (68) (69). The solvents selected were acetone and acetonitrile because of their availability and because the kinetic of aggregation occur in the presence of water in the right range to be analyzed by linear spectroscopy.

4.1.1 CHLOROPHYLL A IN ACETONE-WATER MIXTURE

4.1.1.1 ABSORBANCE SPECTRA

Acetone is a moderately polar solvent that interacts with the chlorophyll pigment by the coordination of one molecule of solvent by its lone pair to the metal orbital (69) (70) (71). Being aprotic, it is not involved in the formation of H bonds leading to the absence of this interaction. The addition of a significant amount of water (70% by vol) leads to the appearance over a period of several hours of an aggregate absorbing at 749 nm (figure 30). Even though acetone is more basic then water (69), theoretical studies (71) suggest that the substitution of acetone by water in the complex with the metal is thermodynamically more favorable. The two solutions studied were made at a low concentration of Chl a 2µM.

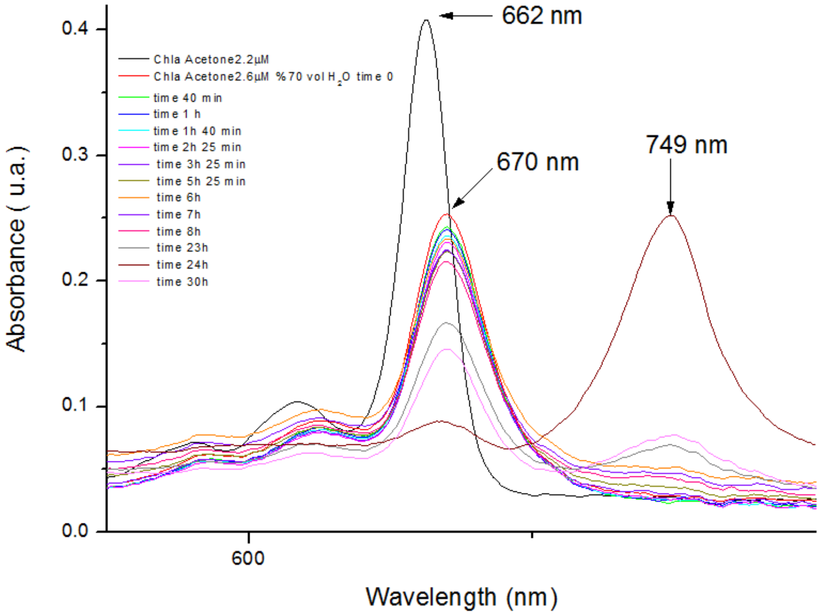

FIGURE 30 SOLUTION OF CHLOROPHYLL IN ACETONE (DARK LINE) COMPARED WITH THE MIXTURE ACETONE 70%VOL WATER EVOLVING IN TIME.

The effect of added water is that of a strong red shift of the Q_y(0-0) band from 662 nm in the pure solution to 670 nm in the mixture immediately after mixing (i.e. within a tens of seconds timescale). Agostiniano et al attributed this to an equilibrium between the monomer and a dimer hidden behind this band that becomes more favorable for the dimer at percentages of water greater that 40% (72).

$$2\text{ChlaS}\ (662\text{nm}) + 2\ H_2O \leftrightarrow (\text{Chla}2H_2O)_2\ (678\text{nm}) + 2S \qquad (1)$$

S = acetone and acetonitrile

This assumption is reasonable considering that this band becomes broader and more red shifted with increasing the percentage of water. According with these studies, the dimer absorbing at 678 nm could represent a good opportunity to study a dimer similar to the one occurring naturally in photosynthetic systems; P680 (73). However, after some hours, the mixture starts to show a high background of light scattering accompanied by the appearance of absorption at 749 nm that clearly appears after 10h. This 749 nm absorption may reflect the formation of Chl a oligomers (73) (68).

Looking at the dependence of the absorbance peaks at 670 and 749 over time (Figure 31), we notice that while the band at 670 nm is decreasing, the band at 749 is increasing. This means that species absorbing at 670 nm are contributing in the formation of the aggregate at 749 nm. However, the graph does not exhibit this unambiguously because of the high background due to scatter and the very slow kinetics, which prevented the reaction being followed to completion.

$$(\text{Chla}2H_2O)_2\ (678\text{nm}) \leftrightarrow (\text{Chla}\ 2H_2O)_n\ (749\ \text{nm}) \qquad \text{with } n>>2 \qquad (2)$$

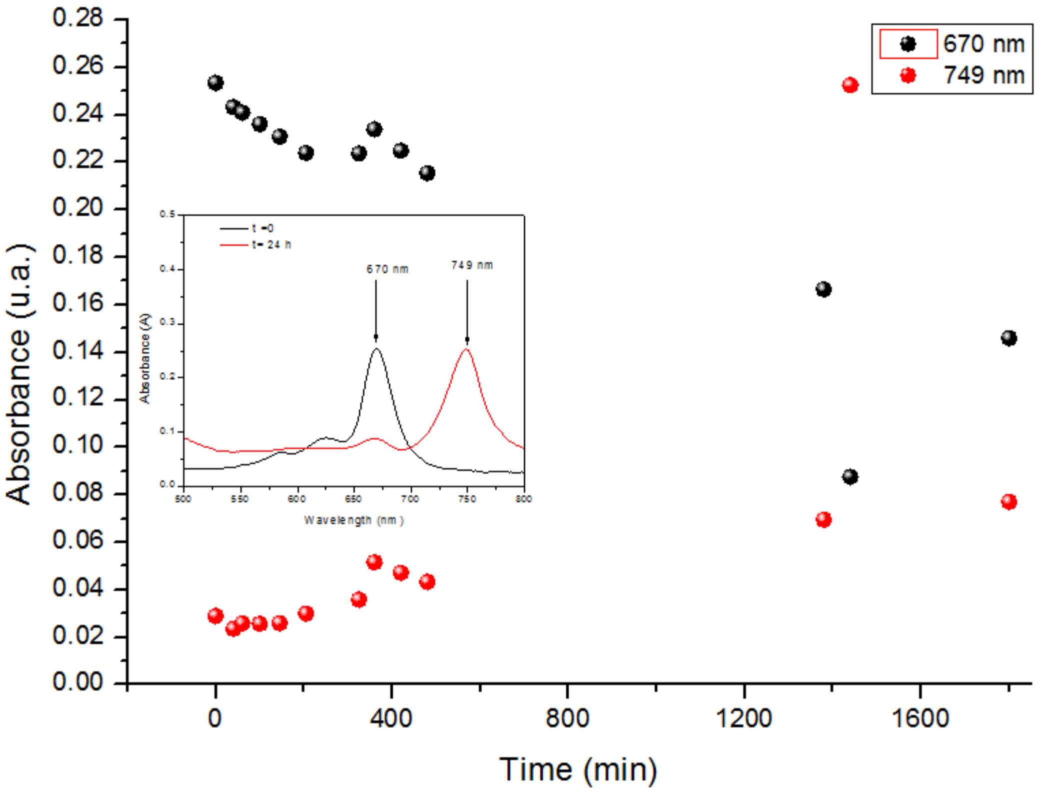

FIGURE 31 INTENSITY OF THE MAIN PEAKS AT 670 NM AND 749 AS A FUNCTION OF TIME.

4.1.1.2 FLUORESCENCE SPECTRA

The addition of 70% water in the Chl a acetone solution immediately generates a strong quenching of fluorescence. The solvent composition dependence will be discussed further in section 4.1.3. We also note that the very weak fluorescence spectra in the Acetone-70%water mixture have distinct time dependence. It was observed (Figure 32) that a blue shift of the more intense band occurred from 678 nm to 673 nm with a doubling of its intensity. In addition, the band at 718 nm decreases by 40% of its initial intensity over 24 hours.

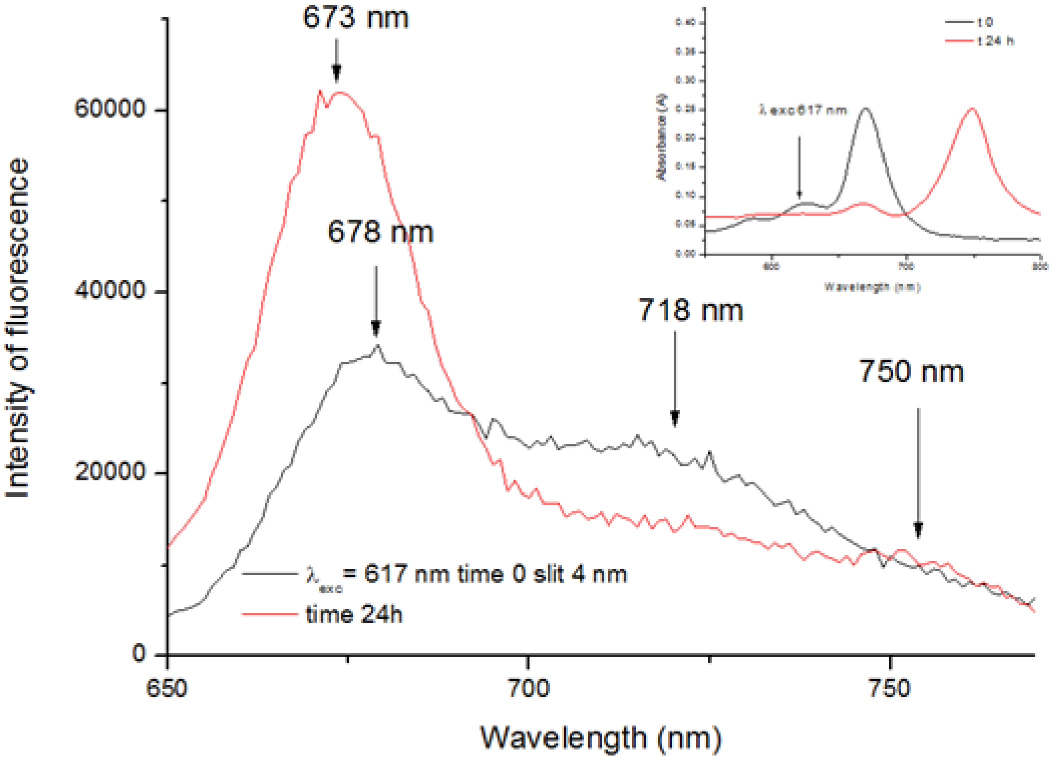

Figure 32 Evolution of fluorescence spectra at the beginning and at the end of the measurement. The inset shows absorbance spectra for time = 0 and time = 24 h and the excitation wavelength.

.

In figures 33,34 and 35, we compare the normalized absorbance and fluorescence spectra of the mixture and monomer (pure acetone) at different times.

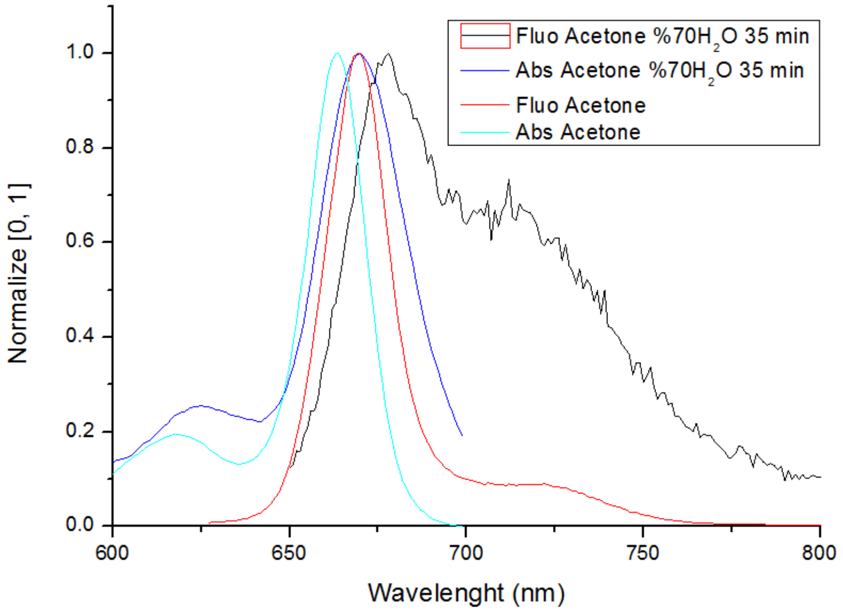

FIGURE 33 FLUORESCENCE AND ABSORPTION SPECTRA OF THE MIXTURE AND THE PURE SOLVENT AFTER 35 MIN.

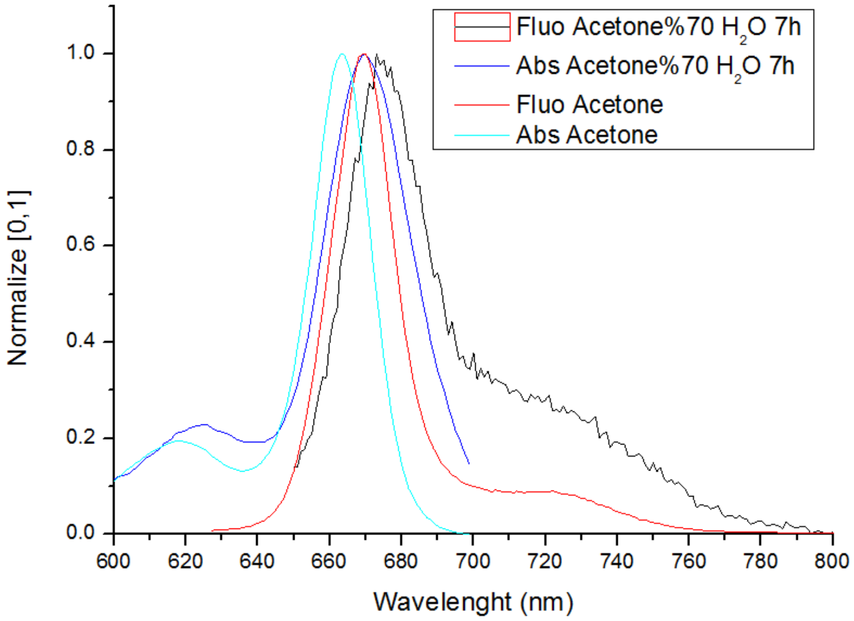

FIGURE 34 FLUORESCENCE AND ABSORPTION SPECTRA OF THE MIXTURE AND THE PURE SOLVENT AFTER 7 H.

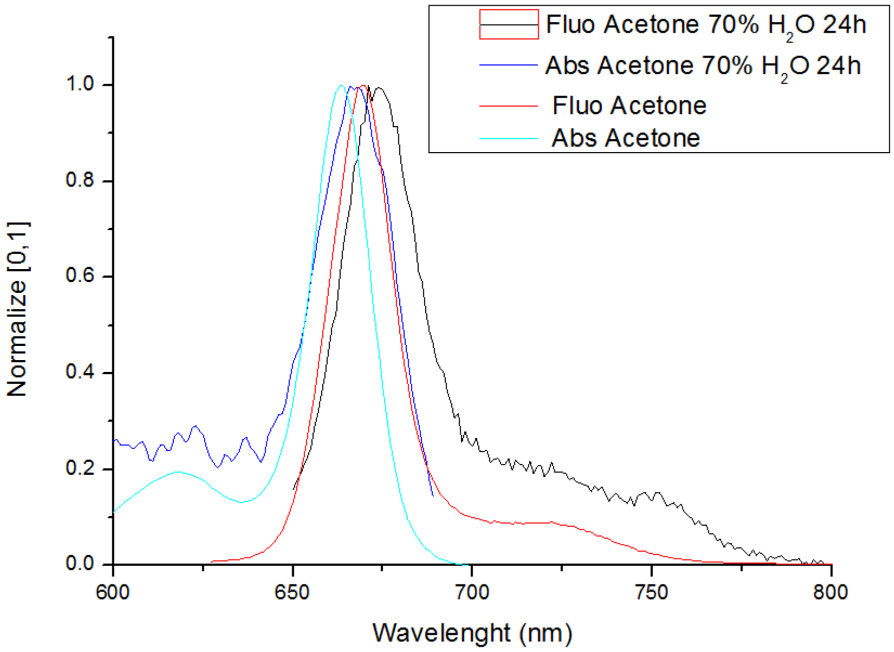

FIGURE 35 SPECTRA RESULTING AT THE END OF THE MONITORING (24 H).

The fluorescence spectrum of the mixture after 24 hours in figure 35 looks very similar to the one of the Chl a. in pure acetone, although very much weaker. This might suggest that the initial fluorescence spectra are a convolution of the monomer and the dimer and then, at longer times, dimers start to nucleate and grow, the only fluorescent species remaining is the very low concentration of monomers. All the measurements of fluorescence were made exciting at 617 nm where only the monomer is present. It is possible that initially there is an energy transfer process of a FRET type having the monomer as donor and the dimer as acceptor (73). This hypothesis is reasonable because of the high presence of dimer at this percentage of water.

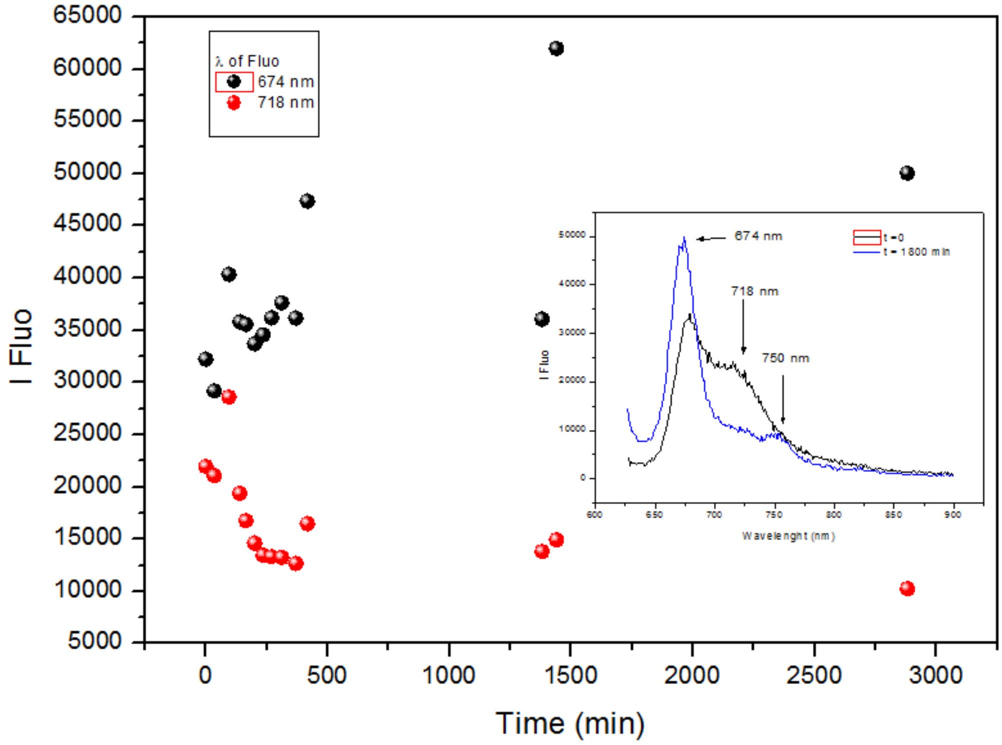

FIGURE 36 THE FIGURE SHOWS HOW THE INTENSITY OF THE MAIN FLUORESCENCE PEAKS AT 674 NM AND 718 NM CHANGE OVER TIME.

Figure 36 shows the decreasing in intensity of the peak at 718 nm as a function of time while the monomer like peak at 674 nm is increasing. As said before, the consumption of the dimer in the aggregation process can be reflected in the disappearing of the 718 nm band. After the consumption of the dimer, the monomer remains in the solution and is not quenched, by FRET, consistent with the rise of monomer like emission at 674 nm.

4.1.2 CHLOROPHYLL A IN ACETONITRILE:WATER MIXTURE

4.1.2.1 ABSORBANCE SPECTRA

As for acetone, acetonitrile belongs to the family of aprotic solvents and thus is not able to generate H-bonds in the solution. It acts as a ligand coordinating one molecule to the metal centre (69) (71) in pure solution. However, the molecule is replaced by a water molecule as in acetone. Consequently this system shows the same dimerization equilibrium discussed in the preceding sections. The experiment of Chl a in acetonitrile solution was performed for mixtures at 70% of water at concentration of 2 μM and 110 μM. Unfortunately, the experiment done at concentration of 2μM was not reproducible in term of time dependent data. However, some common features are present in these experiments such as a band appearing at 710 nm previously reported in literature for high concentrations of water (74) and the presence of an oligomer appearing at 750 nm. Contrary to the acetone-water mixture, the kinetic of the aggregation are much faster, showing the appearance of the aggregate in the red region only 20 minute after mixing. The oligomer (750 nm) achieves its maximum absorbance after 2h and 20 min and the process is even faster for elevated concentrations becoming complete after 1h and 40 min for the 110 μM mixture. This indicates that the reaction has a concentration dependence that has to be taken into account for a future planning of an 2DES spectroscopy experiment. Comparing the pure Chl a acetonitrile solution with the mixture, a shift of the Q_y band is observed from 662nm to 673 nm that can be explained with the presence of both the monomer and the dimer in solution. Contrary to the acetone mixture, the maximum band at around 673 nm in the mixed solvent changes as a function of time; this might indicate the faster consumption of the dimer in the aggregation process (Figure 37). Another important feature is the presence of an isosbestic point at about 717 nm that was also seen in the acetone case; this suggests a simple dimer to aggregate transformation.

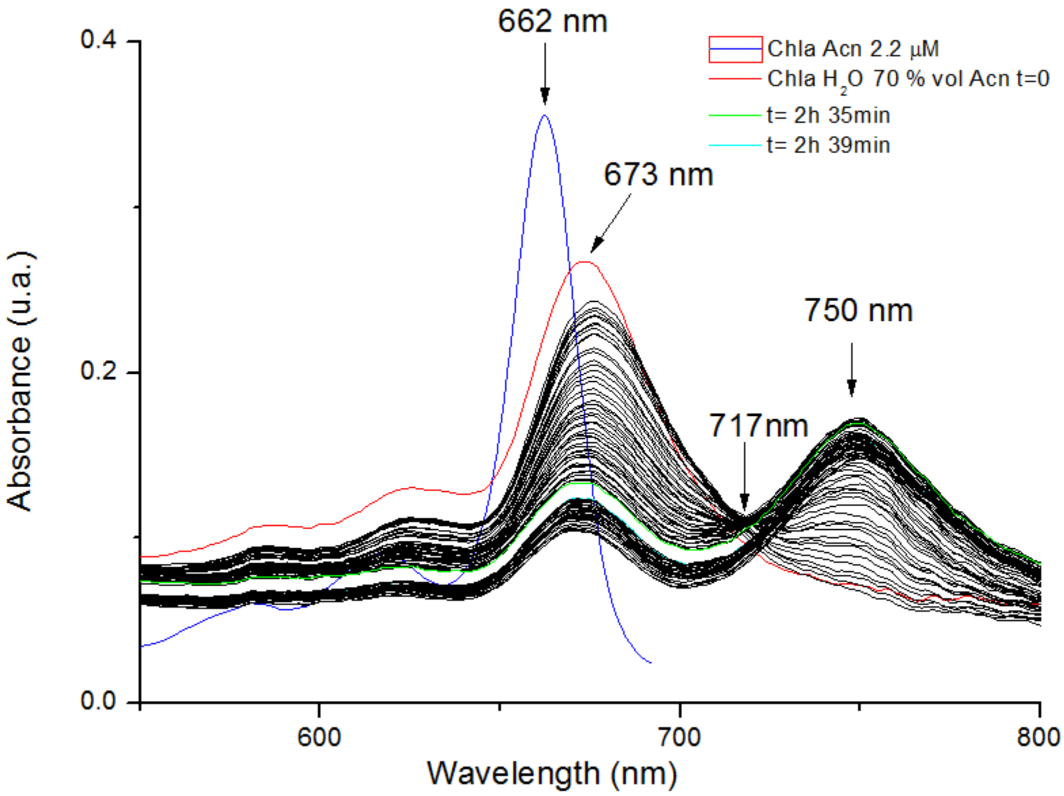

Figure 37 The picture shows the solution of Chla [2.2µM] in acetone pure (blue line) and the evolution of the acetone-water mixture recorded at different times. The spectrum immediately after mixing is the red line, while the spectrum of the maximum absorbance aggregate is in green. The figure illustrates also the isosbestic point at 717 nm.

Monitoring the amplitude at 670 nm and 749 nm as a function of time, it has been showed that the two amplitudes follow the same trend until the maximum oligomer absorbance is achieved (see figure 38 and equilibrium 2). The system behaves differently after the first 150 minutes with a decrease in absorbance from both the bands monitored. This might be explained with the precipitation of the oligomer at 750nm that moves the equilibrium on the right (68).

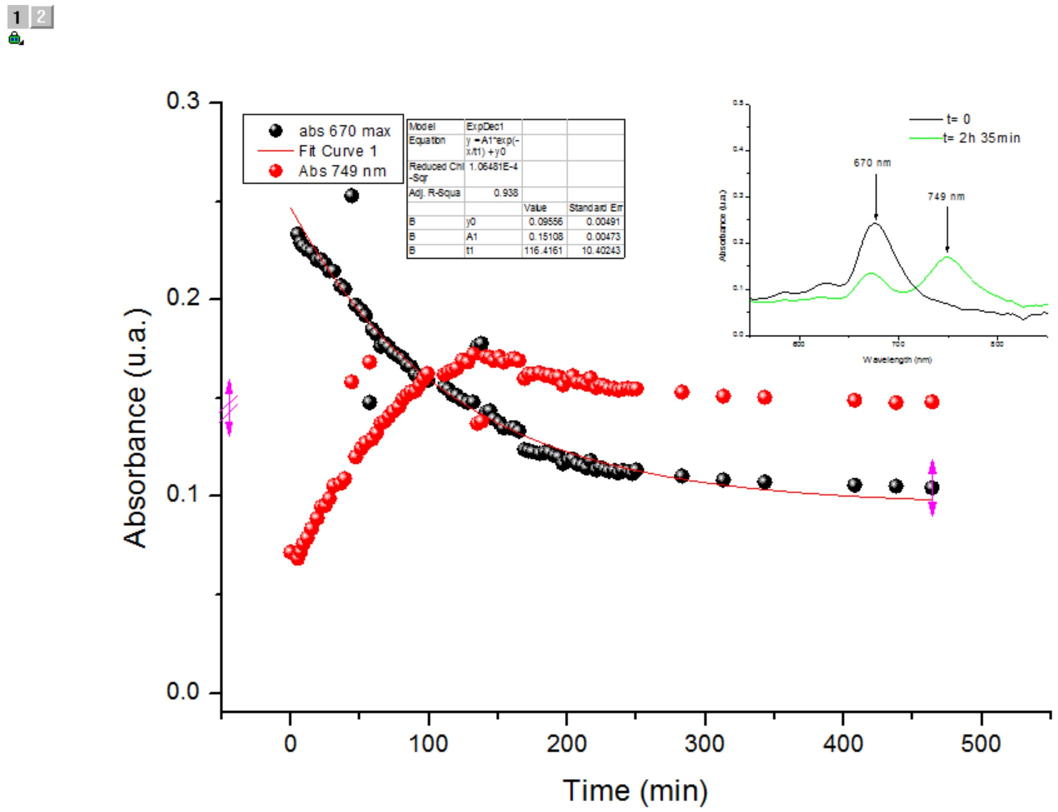

Model	ExpDec1		
Equation	y = A1*exp(-x/t1) + y0		
Reduced Chi-Sqr	1.06481E-4		
Adj. R-Squa	0.938		
		Value	Standard Err
B	y0	0.09556	0.00491
B	A1	0.15108	0.00473
B	t1	116.4161	10.40243

Figure 38 In the inset, the two absorbance spectra indicate the absorbance wavelengths monitored as a function of time for the hydrated monomer and the oligomer. In the main picture the intensities at different times are shown. They follow the same trend for the first 150 minutes.

Comparing acetone and acetonitrile, we can argue that the systems have a similar behaviour that differs only in the rate of the aggregate formation. The reason for that can be found looking through the different forces that drive the aggregation. This process has been defined as a solvent-structure induced process (69) (68) that it is driven mainly by H-bond and dipole-dipole interactions. The two systems compared differ only for the organic solvent and so it has to have an important role in modifying the forces that drive the aggregation. Vladkova and Agostiniano and their co-workers (68) (69) have discussed the solvent influence looking to several parameters and identifying the polarity and the electrophilicity as promoters of aggregations. The capability of orienting molecules and H-bond formation is quantified by the polarity and the electrophilicity, respectively. Since these parameters are larger in acetonitrile than acetone, the self assembly is faster in the acetonitrile case.

4.1.2.2 FLUORESCENCE SPECTRA

Fluorescence spectra of the acetonitrile mixture show clearly that the main fluorescent species is the monomer emitting at 673 nm .The resonant energy transfer process monomer → dimer appears less relevant in this system. In fact, as can be seen in the figures 40, 41 and 42 the fluorescence band which is emitted by the mixture is blue shifted compared with the main absorbing species and overlaps the fluorescence emitted by the monomer in pure acetonitrile. The fluorescence spectra of the acetonitrile mixture also undergo an evolution in time (Figure 39) but it is weaker than the one occurring for the acetone system. The shift was assigned to FRET quenching between monomer and dimer in the acetone system. Evidently this is a smaller effect in acetonitrile, which may reflect the lower concentration of dimers due to faster aggregation.

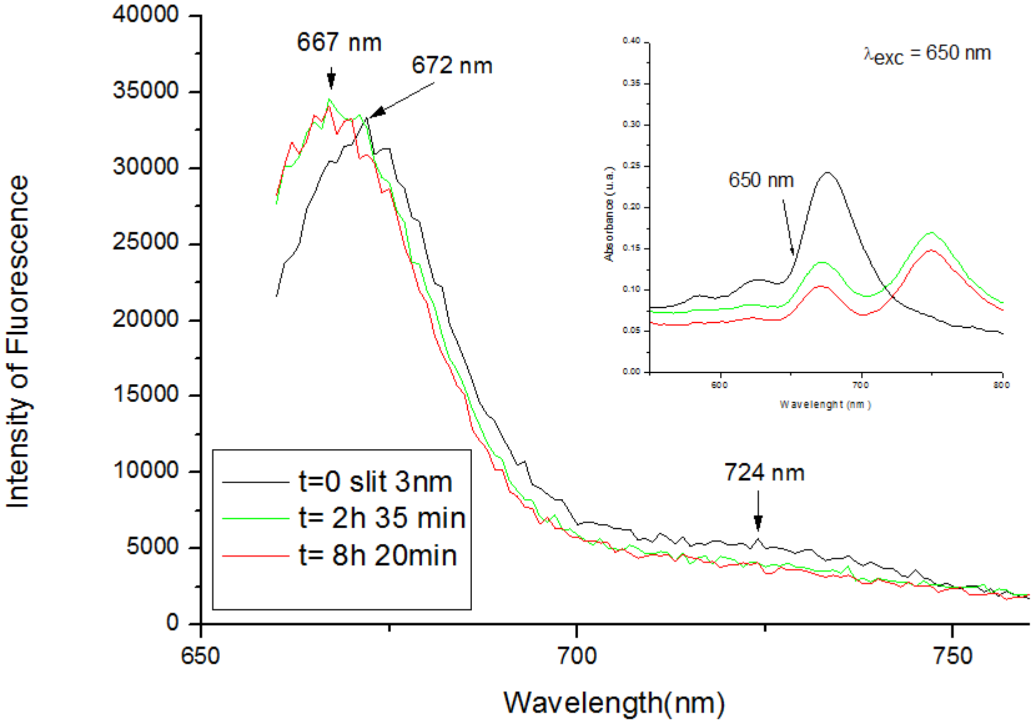

FIGURE 39 ON THE TOP RIGHT, IS INDICATED THE EXCITATION WAVELENGTH USED FOR THE SPECTRA OBTAINED. THE MAIN FIGURE SHOWS THE FLUORESCENCE SPECTRA FOR TIMES T = 0, T = 2H 35 MIN AND T = 8H 20 MIN.

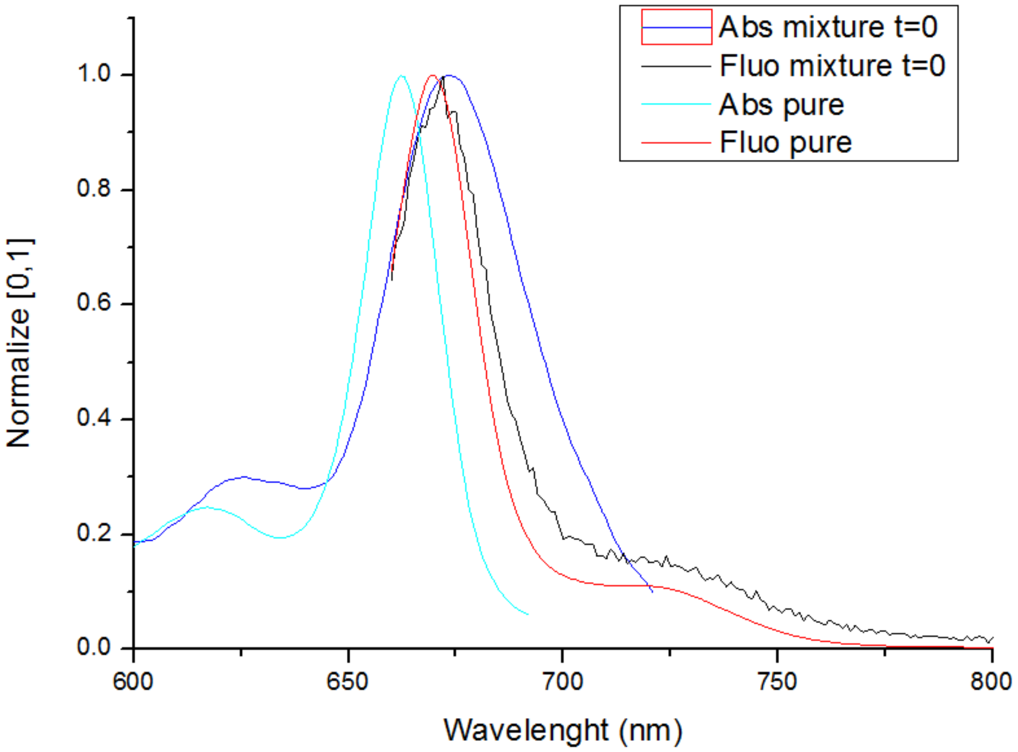

FIGURE 40 FLUORESCENCE SPECTRA OF ACETONITRILE MIXTURE AT T=0.

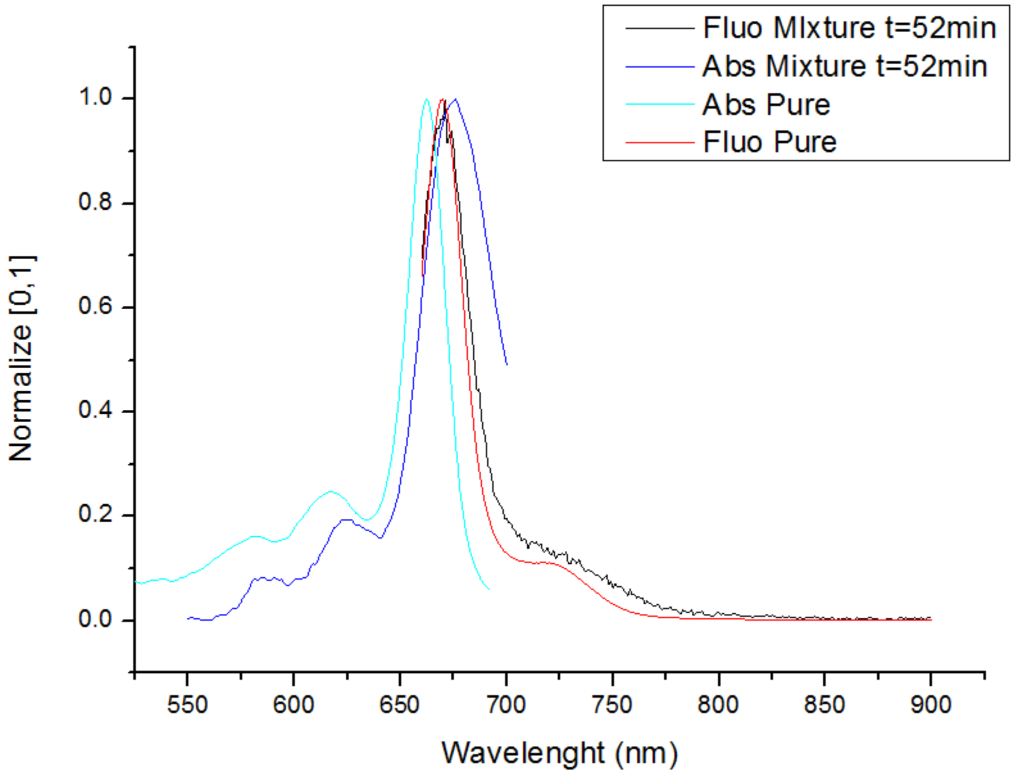

FIGURE 41 FLUORESCENCE SPECTRA OF ACETONITRILE MIXTURE AT T = 52 MINUTES.

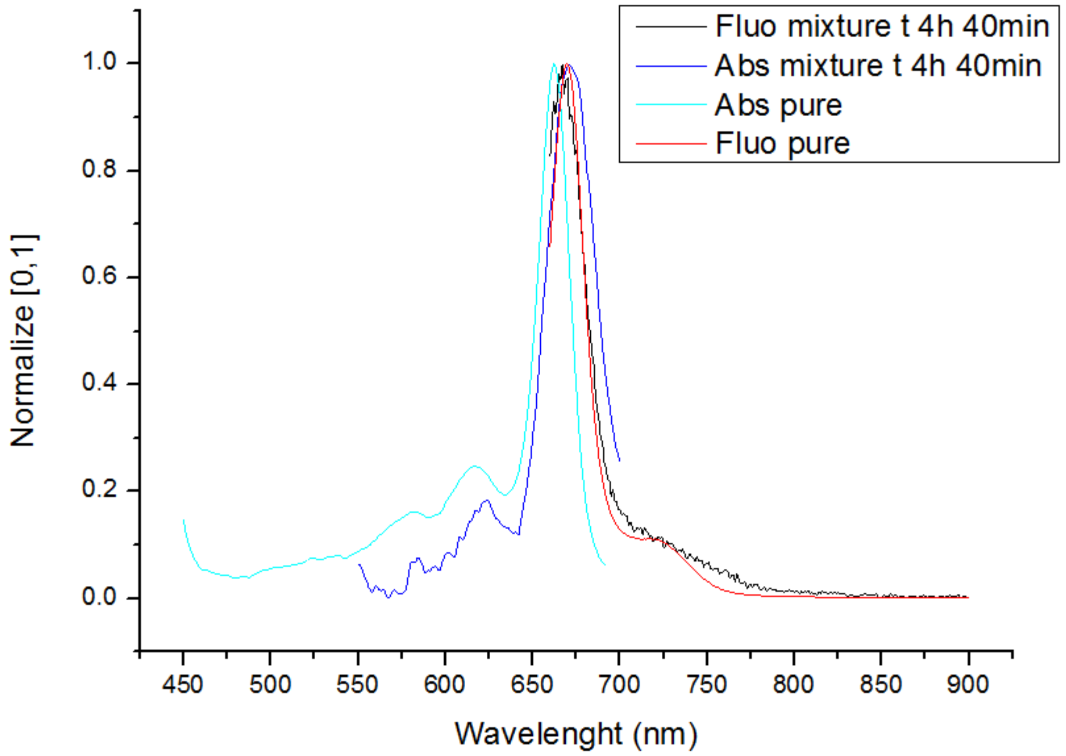

FIGURE 42 FLUORESCENCE SPECTRA OF ACETONITRILE MIXTURE AT T = 4H 40 MINUTES.

4.1.3 QUENCHING OF FLUORESCENCE

The quenching of fluorescence after the addition of water is a phenomenon present in both the mixtures examined. Agostiniano's and Vladkova groups have attributed this behavior to the equilibrium between the monomer and the dimer that shifts towards the dimer and then further aggregation with increasing percentage of water (73) (69). Thus, the quenching of the monomer band is due to the transition Chla → $(Chla2H_2O)_n$ for $n \geq 2$. To monitor this behavior the fluorescence of Chl a with different amounts of water was recorded for different organic solvents. In the plots comparing the fluorescence quantum yield and the molar fraction of water was found a sigmoidal dependence for all the solution studied (69). We present the study for the acetone mixture because of the strong presence of hydrated dimer that could be an interesting subject of further study.

The trend obtained has a good agreement with the previous measurement, having a midpoint of the transition monomer → aggregate occurring at the molar fraction of water equal to 0.76, while in literature it was reported at 0.8 (69). This result shows that a substantial fraction of water is required to stabilize the dimer. Unfortunately, in all cases these samples were observed to provide substantial scatter, suggesting that once dimers form large aggregates also begin to form. This precluded measurements of 2DES of the dimers. In the following section we instead investigate the the effect of non-aqueous solvents on the 2DES of Chl a monomers.

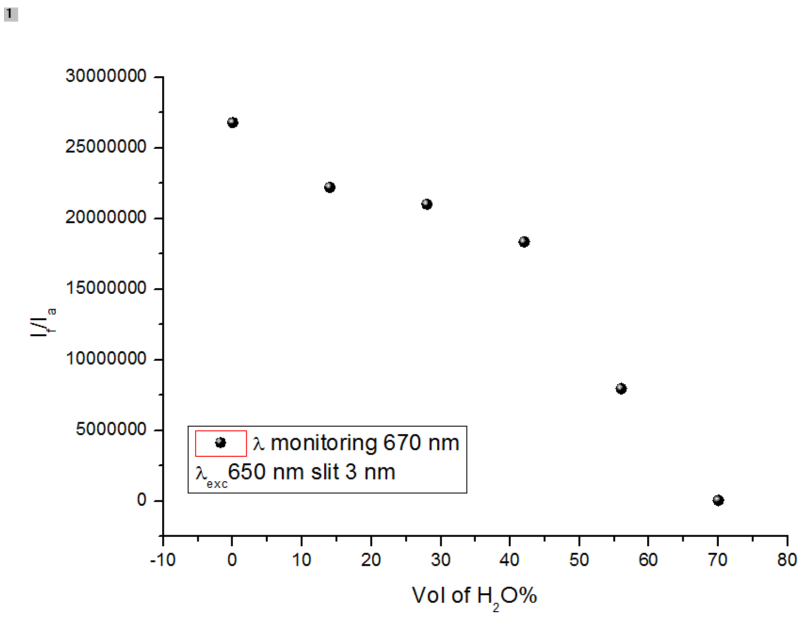

FIGURE 43 INTENSITY OF FLUORESCENCE (CORRECTED FOR ABSORBANCE AT EXCITATION WAVELENGTH OF 650 NM) WAS MONITORED AT 670NM FOR SOLUTIONS WITH DIFFERENT AMOUNTS OF WATER. THE MIDPOINT AT 55% VOLUME OF WATER (CIRCA X_{H2O}=0.76) COULD BE ROUGHLY COMPARED WITH THE ONE MEASURED PREVIOUSLY BY VLADKOVA ET AL (69). INCREASING THE PERCENTAGE OF WATER CAN BE SEEN A GRADUAL RED SHIFT OF THE MAXIMUM OF THE Q_Y BAND WITH A BROAD EFFECT.

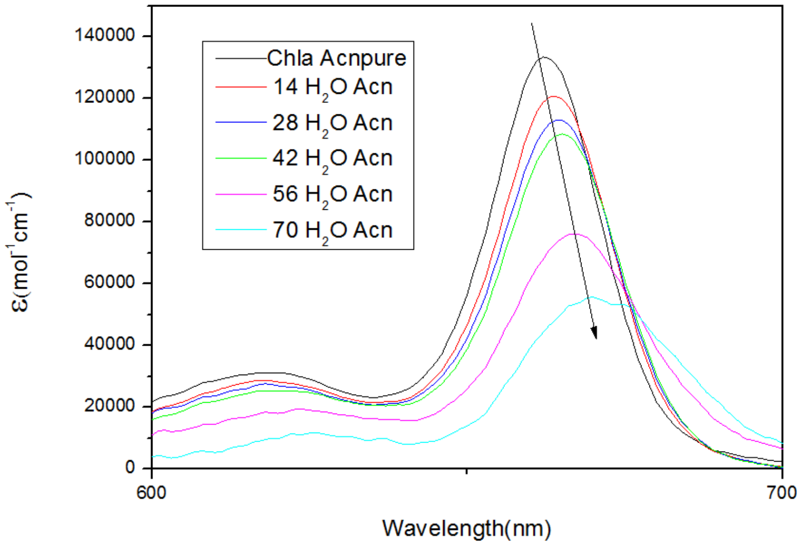

FIGURE 44 THE FIGURE SHOWS THE CHANGE OF ABSORPTION SPECTRA RELATED TO THE INCREMENT OF WATER IN THE SOLUTION OF CHL A IN ACETONITRILE (IN VOL %). AS THE AMOUNT OF WATER BECOMES LARGER, THE SPECTRA BECOME BROADER AND RED SHIFTED.

4.2. SOLVENT DEPENDENCE OF SPECTRAL DIFFUSION FOR THE MONOMER

This section aims to describe the effect of the medium for the monomeric form of Chl a probed by 2DES. The data obtained were further analyzed using the centre line slope (CLS) method previously used by Wells et al. in their 2DIR analysis. In this method, the slope of the 2D spectra is obtained by fitting the maxima of the response amplitude at each detection frequency. This analysis allows characterizing the spectral diffusion dynamics on the tens of picosecond timescale.

In this last part, we will discuss the oscillatory dynamics observed in our 2D spectra and their origin, then we will move on to discuss the analysis done applying the Brownian oscillator method.

4.2.1 VIBRATIONAL MODE

Underdamped oscillatory dynamics were observed in the 2D spectra. Looking at Figure 45, all the points in the 2D spectra A, B and C show a T dependent oscillating signal at 800 cm^{-1}. This mode is close to the one found by Du et al. for Chl a (743 cm^{-1}) in a 2D map. However, its presence across the 2D spectra makes more probable the hypothesis of a solvent Raman active mode. To confirm that the recorded frequency was due to the solvent, the measurement was repeated using the same solvent (cyclohexane) deuterated. The observation of an isotope shift confirmed the solvent contribution. Ziegler et al. have reported the presence of solvent modes in spectrally dispersed third order non-linear optical measurements, but also noted that net energy exchange with the electric field is absent. This leads to the predicted disappearance of the signal for the integration of the pump-probe response for any detected frequency (see figure 46). To confirm that result, we used a simpler porphyrin molecule in toluene solvent. The presence of a strong porphyrin vibronic signal at 380 cm^{-1} makes possible to compare this intermolecular mode with the ones present in the solvent. By integrating the pump-probe response over the probe frequency and then Fourier-transforming it, the only remaining response is the molecular one at $\bar{\nu}_{osc} = 380$ cm^{-1} (Figure 46). Furthermore, the signal completely disappears by applying the same procedure to only the pure solvent. Thus, these observation show that solvent vibrational modes can contribute to the oscillatory response of the 2D spectra. However, these modes can be easily distiguished and separated from the molecular ones by either changing the solvent or integration over the detection frequency.

Intermolecular modes have been found for the point in the 2D map corresponding to peak absorbance (point B figure 45) at 255 cm^{-1} and 345 cm^{-1} . These modes are absent in the other parts of the spectra where the molecular absorbance does not occur (points A and C figure 45).

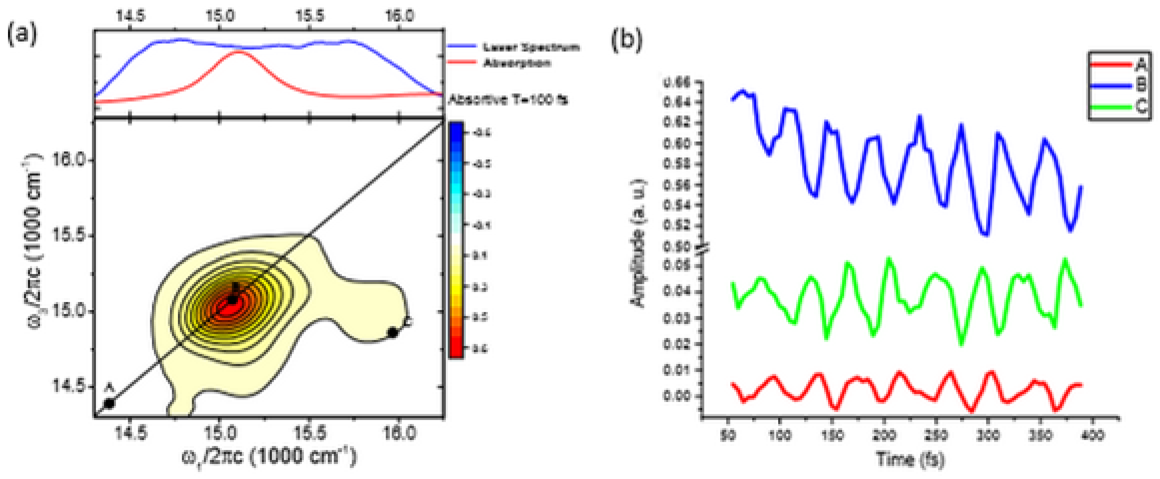

Figure 45 a) 2D spectrum of Chl a in acetone for population time T=100 fs. B) The graph shows the amplitude of points A,B and C for different population time. The oscillations show the same frequency, which means that the mode in not Chl a-dependent.

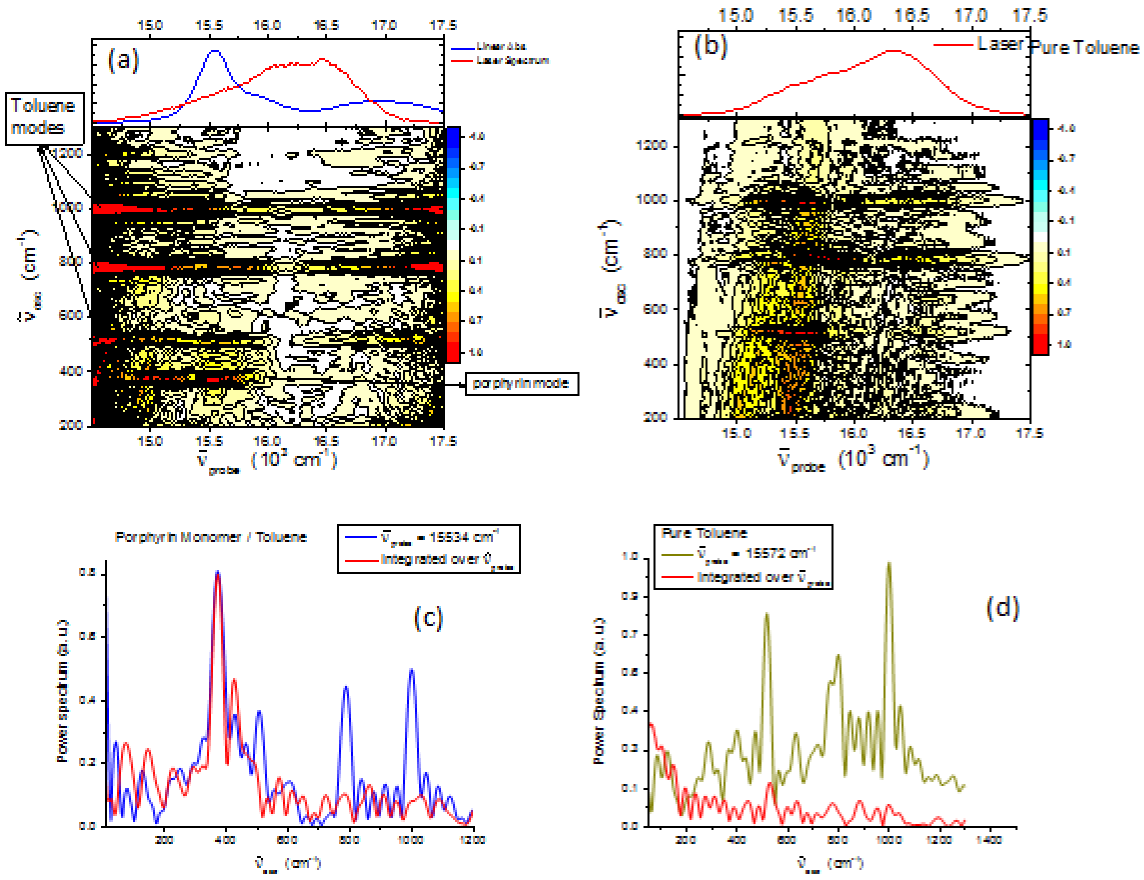

Figure 46 The graphs a) and b) show the Fourier transform of the pump-probe response versus the different probe-frequency, respectively for porphyrin in toluene and pure toluene. In figure a, it is indicated the vibronic signal at 380 cm^{-1} related to a porphyrin mode which is absent in the pump-probe graph b) of pure toluene. Graphs c) and d) exhibit the pump and probe response integrated over the probe pulse. The only pulse that does not disappear is the one related to the molecular mode figure c).

4.2.2 2D SPECTRA ANALYSIS

The following discussion is referred to the 2DES spectra in figure 47 for Chl a in acetone. The spectra are dominated by the electronic transition at 15100 cm^{-1}, corresponding to the Q_y (0-0) band. Its shape is elongated along the diagonal showing the inhomogeneity of the system at early population times. The plots become more circular for later times, reflecting an increase of the homogeneity due to spectral diffusion.

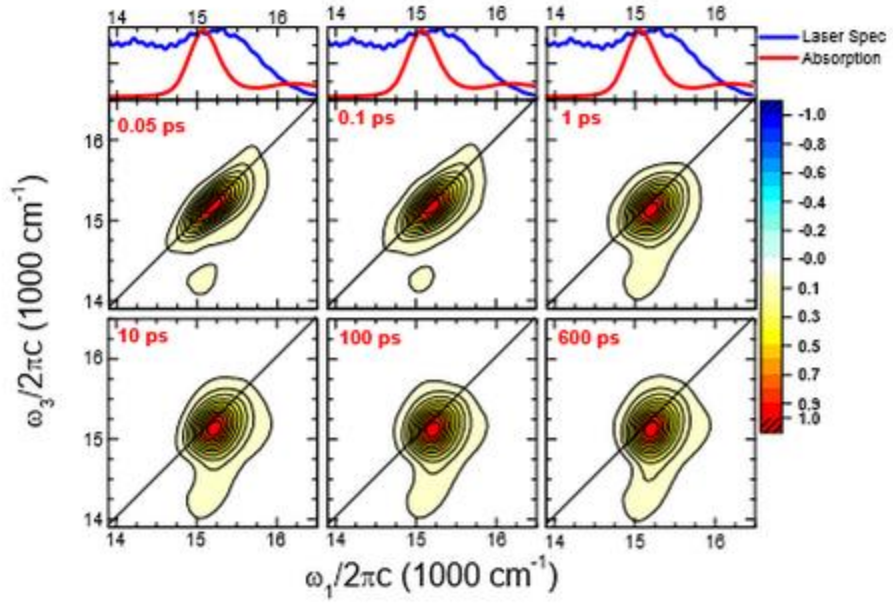

FIGURE 47 SET OF 2D SPECTRA FOR CHL A IN ACETONE. THE INHOMOGENEITY CONTRIBUTION BECOMES LESS RELEVANT WHEN POPULATION TIME INCREASES, SINCE THE MORE ROUNDED FEATURE OF THE 2D SPECTRA.

The evolution of the spectral shape from elongated to circular is an indication of a spectral diffusion that reflects the fluctuation of the Chl a environment (see sub-section 1.2.1.1). The use of D/A ratio (which is equal to the diagonal-oriented value divided by the orthogonal one; Figure 48 d) as a parameter to evaluate the ellipticity of the response is a good method to see the dependence between the frequency-frequency correlation function and the nature of the solvent. Thus, this measure of ellipticity was studied to probe spectral diffusion for Chl a in a variety of solvents.

Solvents were chosen by taking into account a range of viscosity, polarity and capability of H-bond formation. The spectral diffusion is observed to be much slower in viscous solvents such as ethylene glycol (EG). By comparing its D/A with the acetone one, it is apparent that its homogeneity lasts for much longer population times (see figure 48 c). The non-polar solvent cyclohexane (Cyh) on the other hand has a more circular response for earlier times than all the other solvents. Thus, the spectral diffusion is strongly dependent to the medium.

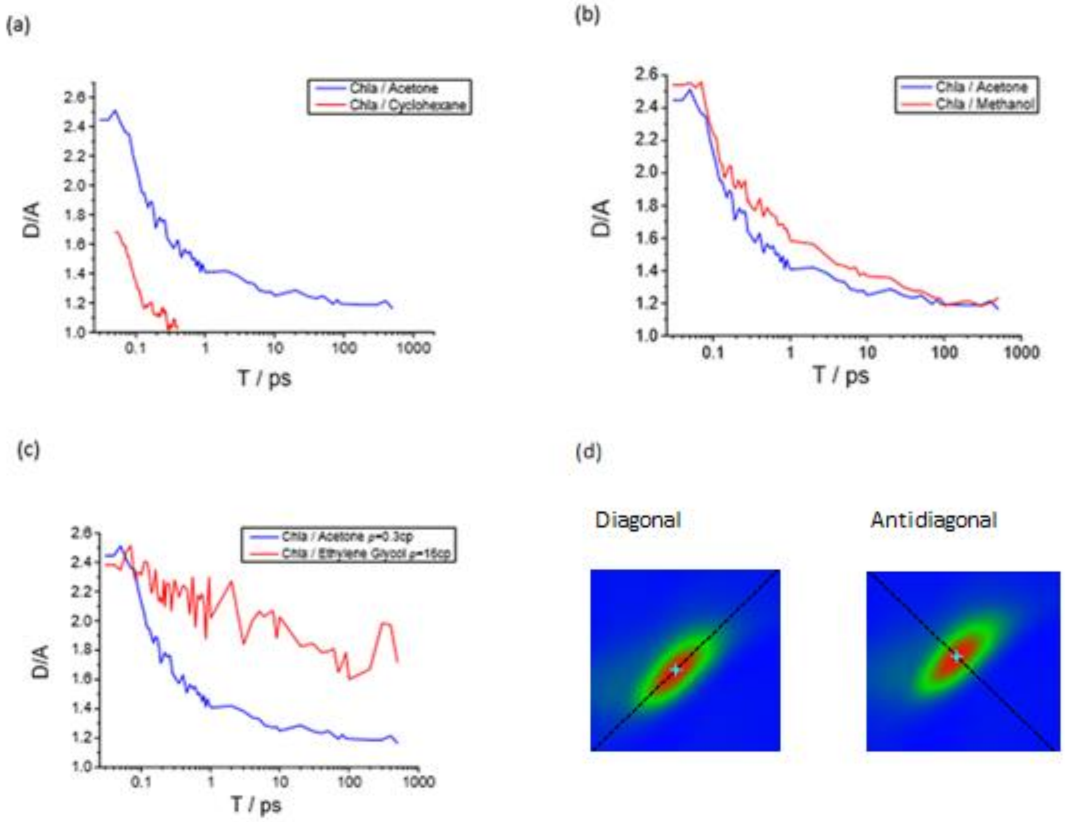

FIGURE 48 A), B) AND C) THE ELLIPTCITY OF THE 2D SPECTRA FOR DIFFERENT SOLVENTS. NOTE THE LOG T SCALE. D) THE PICTURES SHOW THE DIAGONAL AND ANTIDIAGONAL FEATURES USED FOR THE D/A RATIO ANALISIS.

In addition to the main transition Q_y (0-0), a shoulder appears within 50 fs at $\omega_1 \approx 15000\ cm^{-1}$, $\omega_2 \approx 14000\ cm^{-1}$. We can relate this feature to the stimulated emission and thus to the fluorescence spectra. The significant intensity of the laser spectrum covering this region might be responsible for the stimulated emission from the first excited state. Since the emission rises in early times (<50 fs), the stimulated emission may come from population via relaxation of a vibronic state higher than the 0-0 level.

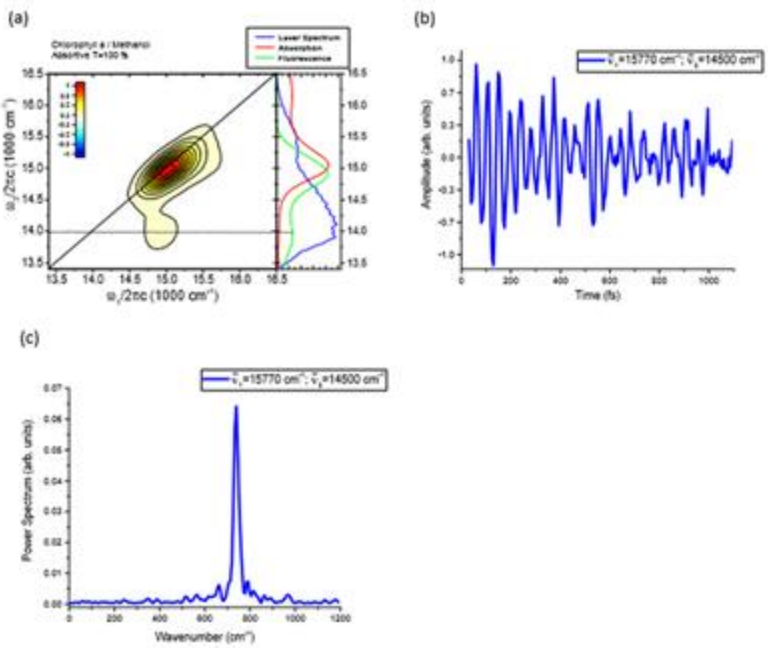

FIGURE 49 A) 2D SPECTRA OF CHL A IN MEOH INDICATING THE FEATURE CORRESPONDING TO AN EMISSION STIMULATED FROM AN EXCITED VIBRONIC STATE HIGHER THAN 0-0 TRANSITION. TRANSITIONS NON-EQUAL TO THE 0-0 ONE MIGHT SHOW FLUCTUATIONS FOR DIFFERENT POPULATION TIMES. THE GRAPH B) ILLUSTRATES THIS FLUCTUATION IN AMPLITUDE. BY FOURIER-TRANSFORMING GRAPH B) WE OBTAIN GRAPH C) THAT SHOWS THE PRESENCE OF ONE VIBRATIONAL MODE OF BCHL A.

4.2.3 SIMULATION OF 2DES SPECTRA.

Starting from the equation which correlates the line shape function *g(t)* with the spectral density $C(\omega)$ (eq 53), it has been possible - by using λ, Λ and ω as fitting parameters - to calculate third order signal which generates a set of modelling experimental data (see paragraph 2.5). The data obtained from these fittings has been used to obtain 2D and linear absorption spectra (see equations 60 and 52). The 2D spectra resulting from this calculation have a good agreement with the ones experimentally recorded. However, a careful analysis of the CLS plots and the linear absorption spectra obtained by theoretical calculations is required to understand the system evolution completely.

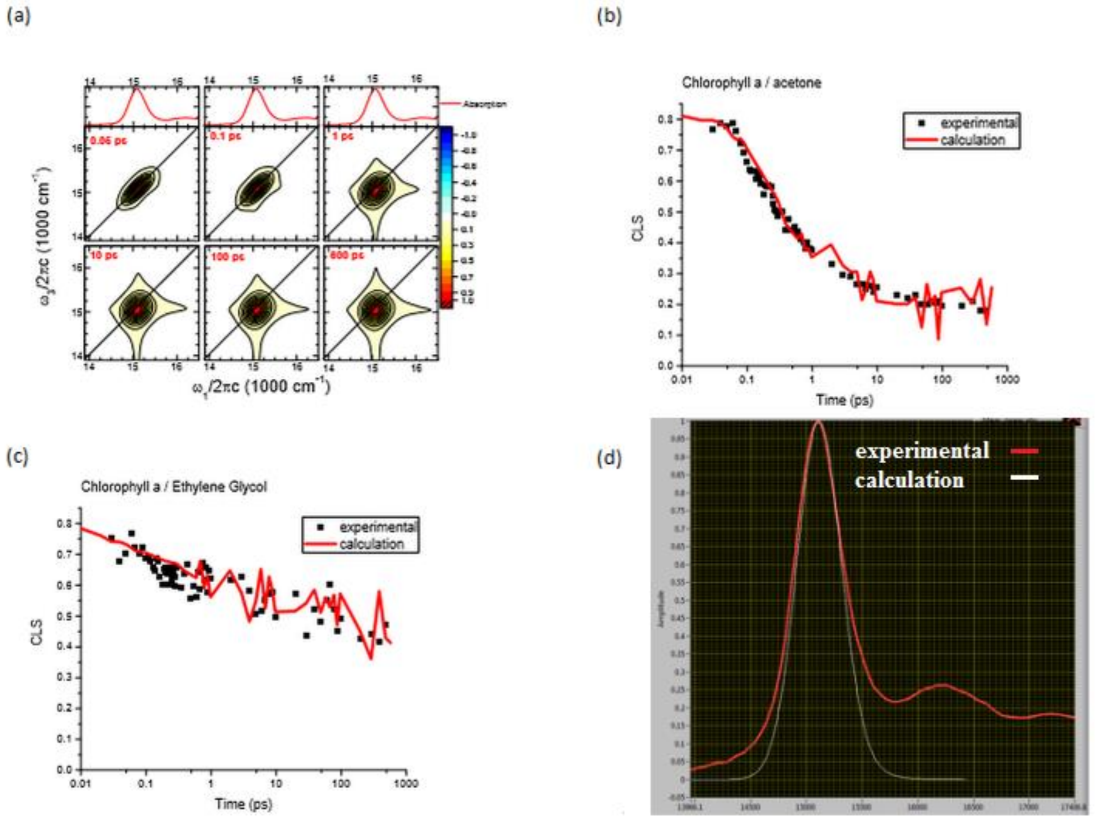

Figure 50 The graph A) compares real and simulated 2D spectra for different population times. The real and simulated spectra have a close trend, so this shows the goodness of the model applied. Plots B) and C)compare the CLS from experimental spectra and the ones calculated for Chl a in acetone and ethylene glycol. Figure D) shows how the BO model fits the linear absorption spectra.

The tables 1A and 1B show the fitting obtained by a sum of four over damped Lorenzian Brownian oscillator (BO, eq 57). This fit result was improved by the substitution of the most highly damped Lorenzian BO with a Gaussian function (eq 58) table 1B.

A)

	τ_1 (ps)	λ_1 (cm^{-1})	τ_2 (ps)	λ_2 (cm^{-1})	τ_3 (ps)	λ_3 (cm^{-1})	τ_4 (ns)	λ_4 (cm^{-1})
AC	0.03	43	1.5	48	40	18	10	19
CAN	0.03	39	1.0	52	20	21	10	15
MeOH	0.23	43	5.0	33	40	36	10	36
EG	0.19	80	5.0	16	32	8	10	95
Cyh	0.46	95	-	-	-	-	10	10

B)

	λ_G (cm^{-1})	ω_G (cm^{-1})	τ_2 (ps)	λ_2 (cm^{-1})	τ_3 (ps)	λ_3 (cm^{-1})	τ_4 (ns)	λ_4 (cm^{-1})
AC	128	48	3.7	26	30	26	10	18
CAN	180	54	1.6	10	30	33	10	21
MeOH	110	104	5.5	55	60	52	10	36
EG	105	170	5.9	29	60	19	10	85
Cyh	-	-	0.46	95	-	-	10	10

Table 1 A) Fits of the 2DES to a sum of four overdamped BOs. B) Fits of the 2DES to a sum of a Gaussian and three overdamped BOs.

The main character of this analysis is the presence of a persistent inhomogeneous broadening, corresponding to the lowest frequency response for longer detection times. The last BO has a relaxation time longer than the time range detected by our experiment (> 1ns) that does not allow us to record the complete relaxation. This residual inhomogeneity can be related to solvent parameters such as viscosity, polarity and H-bonding formation. The solvent with the greatest residual inhomogeneity is the viscous polar H-bonding EG. The reason of its high inhomogeneity is mainly due to its elevated value of viscosity, which slows down the exchange in the H-bonding structure associated to the Chl a pigment. In the other lower molecular weight solvents, such as the polar H-bonding methanol (MeOH), the inhomogeneity persists but its value is reduced. The residual inhomogeneity also seems to be less significant for the polar but non-H-bonding solvent Acetonitrile (ACN), and much smaller for the non-polar Cyclohexane (Cyh). This suggests that the inhomogeneity is related to specific and presumably long lived H-bonded structures between solvent and solute, and that these are stabilized in the diol EG.

Comparing the nonpolar cyclohexane to the polar solvents shows an additional relaxation dynamic on the 0-10 ps timescale in the polar solvents. This component can be tentatively assigned to a diffusive orientation dynamics of the solvent on the sub picosecond to many picoseconds time scale. Such liquid dynamics have been characterized by ultrafast optical Kerr effect measurements and by the study of high frequency dielectric relaxation (75) of the pure solvent. Apparently such dynamics may play a role in chl a spectral diffusion. However,, no one-to-one correlation has been found between the orientational dynamics of pure solvents and our measures times. Thus, we interpret our multiple timescale as a representation of the dynamics of solvent reorganiusation in the presence of the solute, possibly reflecting some specific solvent solute interactions.

5. CONCLUSIONS

This work aimed to contribute to a better understanding of the phenomena occurring in light harvesting pigments in nature. In plants, pigment-protein complexes fulfill this role with a quantum efficiency near to unity, 2DES offers an incisive tool to probe photosynthetic systems by monitoring energy transfer pathways, energy landscapes, vibronic and electronic coherences.

Chl a is well known for its role in light harvesting and so it was considered a good start for these studies. Because of its insolubility in water due to the hydrophobic tail, we decided to analyze Chl a in organic solvent-water mixtures, in order to investigate the possibility of studying both monomer and aggregate forms by 2DES. The organic solvents chosen for this purpose were acetone and acetonitrile, which reveal aggregation in mixtures with water. Both systems showed an aggregate absorbing at 750 nm formed by a solvent-structure-induced process. Systems were found to have the same equilibria behind the aggregation process but with quite different rate, due to the characteristics of the organic solvent. The mixture in acetone was the most interesting because of its higher presence of a dimer at 678 nm. An energy transfer by FRET mechanism between the monomer as a donor and the dimer as an acceptor seemed to be relevant in this particular system. Unfortunately, these two examined systems exhibit strong light scattering due to the high percentage of water and to the presence of the aggregate at 750 nm in colloidal form. This makes impossible a further study by 2DES technique.

Later, the Chl a monomer study has been conducted in different organic solvents by 2DES spectroscopy. The presence under high resolution of oscillatory dynamics due to solvent modes were observed for the cyclohexane solution across the 2D map. This fact confirms the presence of solvent contribution in third order nonlinear measurements. Although similar results were previously reported by Ziegler et al. in optical Kerr effect experiments it is the first time they have been characterized in 2DES. Although these modes could be mis-assigned as solute modes, fortunately, they can be easily recognized and separated from the more interesting molecular ones by using solvent isotope shift methods and by Fourier-transforming the pump-probe response integrated over the detection-frequency.

In the 2D spectra obtained, the dominant feature was the pure electronic transition corresponding to the Q_y band. An evolution of the shape of the 2DES from more elongated to circular has been observed, and assigned to spectral diffusion. However, an inhomogeneous broadening contribution was observed to persist for long population times. This inhomogeneity (which is not observed for simple porphyrins in similar solvents) was found to be more relevant in H-bounding and viscous media and smaller in nonpolar solvents. The details of the Chl a spectral diffusion has been analyzed by the Brownian oscillator model, which was shown to reproduce both the linear absorbance and the 2D spectra. By comparing theoretical and analytical data, we obtained a good agreement using a sum of four Brownian Oscillators. Good agreement was obtained between theory and experiment. The .parameters extracted suggested that the picosecond spectral diffusion may arise from solvent orientational relaxation in the presence of the solute.

To conclude, our studies enlightened some relevant aspects of Chl a aggregates and dimers in mixtures, as well as Chl a monomers in pure solution. However, further studies are required in order to identify a system which can give more exhaustive answers about the fascinating chl a aggregates which occur in nature.

Acknowledgements

I would like to thank Professor Steve Meech for his encouraging support during my project. He taught me to have a critical thinking toward scientific problems and I am very grateful to him for that. I also give my acknowledgements to the other members of his group Dr. Heisler, Dr. Laptenok and Mr Valduga for their company and help.

REFERENCES

1. **Demtr¨oder, W.** *Laser spectroscopy.* Berlin : Springer Verlag, 1991.

2. **Graham R. Fleming, Mino Yang, Ritesh Agarwal, Bradley S. Prall, Laura J. Kaufman and Fred Neuwahl.** Two Dimensional Electronic Spectroscopy. *Two Dimensional Electronic Spectroscopy.* 2003, Vol. 24, 1081-1090.

3. **Gabriela S. Schlau-Cohen, Akihito Ishizaki, Graham R. Flemming.** Two-dimensional electronic spectroscopy and photosynthesis: Fundamentals and applications to photosynthetic light-harvesting. *Chemical Physics* . 2011, Vol. 386, 1-22.

4. *Two-dimensional spectroscopy. application to nuclear magnetic resonance.* **W. P. Aue, E. Bartholdi, and R. R. Ernst.** 1976, Journal of Chemical Physics, p. 64(2229).

5. ***P., Hamm.*** *1998, J. Phys. Chem. B.*

6. ***D, Hybl J.*** *1998, Chem. Phys.Lett .*

7. ***Herbert Van Amerongen, Leonas Valkunas and Rienk Van Grondelle.*** *Photosynthetic excitons. Singapore : World Scientific Publishing Co. Pte. Ltd. , 2000.*

8. ***Pale, Ville.*** *Improving the optical properties of chlorophyll aggregates with. 2011.*

9. Solution structures of 132-methoxychlorophyll a epimers. ***J. Helaja, K. Hyv¨arinen, S. Heikkinen, I. Kilpelainen and P. H. Hynninen.*** *1995, Journal of Molecular, pp. Vol. 354, Issue 1, pp. 71,74-75,78.*

10. ***Sundholm., J. Jus´elius and D.*** *The aromatic pathways of porphins, chlorins and bacteriochlorins. Physical Chemistry Chemical Physics. 2000, Vol. 2, 2145-2151.*

11. Spectra of porphyrins. ***Gouterman, M.*** *1961, Journal of Molecular Spectroscopy, pp. Vol.6 pp.138-163.*

12. Spectra of porphyrins: Part III. Self-consistent molecular orbital calculations of porphyrin and related ring systems. ***Gouterman, M.*** *1965, Journal of Molecular Spectroscopy, pp. Vol. 16, Issue 2, pp. 415-450.*

13. Density functional theory calculations of the visible spectrum of chlorophyll a. ***Sundholm, D.*** *1999, Chemical Physics Letters, pp. Vol. 302, Issues 5-6, pp. 480-484.*

14. *Theoretical Study of the Excited States of Chlorin, Bacteriochlorin, Pheophytin a, and Chlorophyll a by the SAC/SAC−CI Method.* **J. Hasegawa, Y. Ozeki, K. Ohkawa, M. Hada and H. Nakatsuji.** *1998, The Journal of Physical Chemistry B, pp. Vol. 102 (7), pp. 1320-1326.*

15. **Milgrom, L. R.** *The colour of life: an introduction to Chemistry of porphyrins and relaten compound. United Staes : Oxford University Press, 1997.*

16. **B. Grimm, R. J. Porra, W. R¨udiger and H. Scheer.** *Chlorophylls and Bacteriochlorophylls. Netherlands : Springer, 2006.*

17. **Dolphin, D.** *The Porphyrins III, Physical Chemistry, Part A. New York : Academic Press, 1978.*

18. **Smith, M. Warren and A.** *Tetrapyrroles: Birth, Life and Death. s.l. : Springer, 2009.*

19. **B. Grimm, R. J. Porra, W. R¨udiger and H. Scheer.** *Chlorophylls and Bacteriochlorophylls. Netherlands : Springer, 2006.*

20. *Self-Assembly of an Artificial Light-Harvesting Antenna: Energy Transfer from a Zinc Chlorin to a Bacteriochlorin in a Supramolecular Aggregate.* **Prof. Dr. Hitoshi Tamiaki, Tomohiro Miyatake, Prof. Dr. Rikukei Tanikaga, Prof. Dr. Alfred R. Holzwarth and Prof. Dr. Kurt Schaffner.** *1996, Angewandte Chemie , pp. Volume 35, Issue 7, pages 772–774.*

21. **R. Blankenship, M. T. Madigan and C. E. Bauer.** *Anoxygenic Photosynthetic Bacteria. Dordrecht : Kluwer Academic Publishers, 1995.*

22. **Sund, G. Blauer and H.** *Optical Properties and Structure of Tetrapyrrols. London : De Gruyter, 1985.*

23. *Structure–Property Relationships for Self-Assembled Zinc Chlorin Light-Harvesting Dye Aggregates.* **Valerie Huber Dr., Sanchita Sengupta and Frank Würthner Prof. Dr.** *s.l. : Chemistry - A European Journal, 2008, Chemistry - A European Journal, pp. Volume 14, Issue 26, pages 7791–7807.*

24. *Ultrahigh Field MAS NMR Dipolar Correlation Spectroscopy of the Histidine Residues in Light-Harvesting Complex II from Photosynthetic Bacteria Reveals Partial Internal Charge Transfer in the B850/His Complex.* **Jörg Matysik, Claudia Soede-Huijbregts , Marc Baldus ,Jan Raap , Johan Lugtenburg , Peter Gast, Hans J. van Gorkom, Arnold J. Hoff and Huub J. M. de Groot.** *2001, J. Am. Chem. Soc., pp. 123 (20), pp 4803–4809.*

25. The Crystal and Molecular Structure of Ethyl Chlorophyllide a* 2HO and Its Relationship to the Structure and Aggregation of Chlorophyll a*. **STROUSE, CHARLES E.** 1973, Proc. Nat. Acad. Sci. USA, pp. Vol. 71, No. 2, pp. 325-328.

26. Molecular dynamics simulation study of chlorophyll a in different organic solvents. **Roccatano, Khadga Karki and Danilo.** 2011, Journal of chemical theory and computation, pp. 7,1131-1140.

27. **Seely., L. P. Vernon and G. R.** The Chlorophylls. New York : Academic Press, 1966.

28. Aggregation and fluorescence quenching of chlorophyll a of the light-harvesting complex II from spinach in vitro. **Helmut Kirchhoff, Hans-Jürgen Hinzb and Jörg Rösgenb.** 2003, Biochimica et Biophysica Acta (BBA) - Bioenergetics, pp. Volume 1606, Issues 1–3,Pages 105–116.

29. THE THEORY OF MOLECULAR EXCITONS. **Davydov., A. S.** 1964, Soviet Physics Uspekhi, pp. Vol.82, pp. 393-448.

30. The exciton model in molecular. **M. Kasha, H. R. Rawls and M. A. El-Bayoumi.** 1965, Pure and Applied Chemistry, pp. Vol. 11, No. 3-4, pp. 371-392.

31. **Maximilians, Julius.** Methods of Nonlinear Femtosecond Spectroscopy in the Visible and Ultraviolet Regime and their Application to Coupled Multichromophore Systems. Wu¨rzburg : s.n., 2012.

32. **Jackson., J. D.** Classical Electrodynamics. s.l. : John Wiley & Sons , 1998.

33. Fermion excited states in one-dimensional molecular aggregates with site disorder: Nonlinear optical response. **Spano, F. C.** 1991, Physical Review Letters, pp. 67, 3424–3427.

34. J-Aggregates. **Kobayashi, T.** 1996, World Scientific.

35. **E. E. Ostroumov, R. M. Mulvaney, J. M. Anna, R. J. Cogdell and G. D. Scholes.** 2013, J. Phys. Chem. B., pp. 117, 11349-11362.

36. Tracing exciton dynamics in molecular nanotubes with 2D electronic spectroscopy. **A. Nemeth, F. Milota, J. Sperling, D. Abramavicius, S. Mukamel, and H. F. Kauffmann.** 2009, Chem. Phys. Lett., pp. 469, 130.

37. **Nemeth, Mag. Alexandra.** Exploring the potential of two-dimensional electronic spectrocopy. Wien : 2010, 2010.

38. ***Kubarych, J. P. Ogilvie and K. J.*** *Multidimensional Electronic and Vibrational Spectroscopy: An Ultrafast Probe of Molecular Relaxation and Reaction Dynamics. Advances in Atomic, Molecular, and Optical Physics. s.l. : Elsevier, 2009.*

39. ***Zanni, Peter Hamm and Martin.*** *Concepts and methods of 2D infrared spectrocopy. Zurich : Cambridge.*

40. Investigation of electronic couplings in semiconductor double quantum wells using coherent optical twodimensional Fourier transform spectroscopy. . ***X. Li, T. Zhang, S. Mukamel, R. P. Mirin, and S. T. Cundiff.*** *2009, Solid State Communications, pp. 149, 361.*

41. Two-dimensional spectroscopy of electronic couplings in photosynthesis. ***T. Brixner, J. Stenger, H. M. Vaswani, M. Cho, R. E. Blankenship, and G. R. Fleming.*** *2005, Nature, pp. 434, 625.*

42. Pathways of Energy Flow in LHCII from Two-Dimensional Electronic Spectroscopy. ***G. S. Schlau-Cohen, T. R. Calhoun, N. S. Ginsberg, E. L. Read, M. Ballottari, R. Bassi, R. v. Grondelle, and G. R. Fleming.*** *2009, J. Phys. Chem. B, pp. 113, 15352.*

43. Two-dimensional Fouriertransform Spectroscopy of Potassium Vapor. ***X. Dai, A. D. Bristow, D. Karaiskaj, and S. T. Cundiff.*** *2010.*

44. ***Justin R., Caram, Andrew F. Fidler, and Gregory S. Engel.*** *Excited and ground state vibrational dynamics revealed by two-dimensional electronic spectroscopy. The journal of chemical physics. 2012, Vol. 137.*

45. ***Vytautas Butkus, Donatas Zigmantas, Leonas Valkunas and Darius Abramavicius.*** *Vibrational vs. ecectronic coherences in 2D spectrum of molecular system. Cham. Pys. Lett. 2012, Vol. 545, 40-43.*

46. ***P. F. Tekavec, J. A. Myers, K. L. M. Lewis, and J. P. Ogilvie.*** *Two-dimensional electronic spectroscopy with a continuum probe. Opt. Lett. 2009, Vol. 34, 1390.*

47. ***Jonas, S. M. Gallagher-Faeder and D. M.*** *Two-dimensional Electronic Correlation and Relaxation Spectra: Theory and Model Calculations. J. Phys. Chem. A. 1999, Vol. 103.*

48. ***T. Manˇcal, A. Nemeth, F. Milota, V. Lukeˇs, H. F. Kauffmann, and J. Sperling.*** *Vibrational wave packet induced oscillations in two-dimensional electronic spectra. II. Theory. J. Chem. Phys. 2010, Vol. 132, 184515.*

49. *A. Nemeth, F. Milota, T. Manˇcal, V. Lukeˇs, J. Hauer, H. F. Kauffmann, and J. Sperling.* *Vibrational wave packet induced oscillations in two-dimensional electronic spectra. I. Experiments. . J. Chem. Phys. 2010, Vol. 132, 184514.*

50. ***A. Nemeth, F. Milota, T. Manˇcal, V. Lukeˇs, H. F. Kauffmann, and J. Sperling.*** *Vibronic modulation of lineshapes in two-dimensional electronic spectra. Chem. Phys. Lett. 2008, Vol. 459, 94.*

51. **Hamm, Peter.** *Principles of Nonlinear Optical Spectroscopy: A Practical Approach . Zurich : 2005, 2005.*

52. **Mukamel, S.** *Principles of Nonlinear Optical Spectroscopy. New York : Oxford Press, 1995.*

53. *Molecular vibrations-induced quantum beats in two -dimensional electronic spectroscopy.* ***Vytautas Butkus, Leonas Valkunas and Darius Abramavicius.*** *2012, The journal of chemical physics, pp. 137,044513.*

54. *Coherent two-dimensional optical spectroscopy.* **Cho, M.** *2008, Chem. Rev., pp. 108,1331.*

55. *Nonlinear response function for time-domain and frequency-domain four-wave mixing.* **Loring, S. Mukamel and R. F.** *1986, J. Opt. Soc. Am, pp. 3,595.*

56. ***T. Brixner, T. Mancal, I. V. Stiopkin and G. R. Fleming.*** *2004, J. Chem. Phys, pp. 121, 4221-4236 .*

57. **H. van Amerogen, L. Valkunas, and R. van Grondelle.** *Photosynthetic Excitons. Singapore : World Scientific, 2000.*

58. **Kuhn, V. May and O.** *Charge and energy transfer dynamicsin molecular systems. Weinheim : Wiley-VCH, 2011.*

59. **Petruccione, H. P. Breuer and F.** *The theory of open quantum systems. New York : Oxford University Press, 2002.*

60. ***Tobias Brixner, Tomas Manca, Igor V. Stiopkin and Graham R. Flemming.*** *Phase-stabilized two-dimensional electronic spectroscopy. Journal of Chamical Physics. 2004, Vol. 121, 4221-4236.*

61. **M. L. Cowan, J. P. Ogilvie and R. J. D. Miller.** *2004, Chem. Phys. Lett. , pp. 184-189.*

62. Two-dimensional electronic spectroscopy based on conventional optics and fast dual chopper data acquisition. ***Ismael A. Heisler, Roberta Moca, Franco V. A. Camargo Stephen R- Meech.*** *2014, Review of Scientific Instruments.*

63. Inherently phase-stable coherent two-dimensional spectroscopy using only conventional optics. ***Ulrike Selig, Florian Langhojer, Frank Dimler, Tatjana Loehrig, Christoph Schwarz,.*** *2008, Optisc letter.*

64. ***V. I. Prokhorenko, A. Halpin and R. J. D. Miller.*** *2009, Optics Express.*

65. ***M. L. Cowan, J. P. Ogilvie and R. J. D. Miller.*** *2004, Chem. Phys. Lett.*

66. Two-dimensional electronic spectroscopy with double modulation lock-in detection: enhancement of sensitivity and noise res-. ***Zigmantas, Ramunas Augulis and Donatas.*** *2011, OPTICS EXPRESS, pp. 19(14):13126–13133.*

67. ***J, Brixner T.*** *2004, Chem. Phys., p. 121:4221.*

68. Chlorophyll a behavior in aqueous solvents: formation of nanoscale self-assembled complexes. **Autori: Agostiano A., Cosma P. , Trotta M. , Monsù-Scolaro L. , Micali N.** *2002, JOURNAL OF PHYSICAL CHEMISTRY B, pp. 106,12820-12829.*

69. Chlorophyll a Self-assembly in Polar Solvent–Water Mixtures. **R., Vladkova.** *2007, Photochemistry and Photobiology, pp. 71,71-83.*

70. The effects of hydrogen bonding and coordination interaction in visible absorption and vibrational spectra of chlorophyll a. **Krawczyk, Stanislaw.** *1989, Biochimica et Biophysica Acta, pp. 976,140- 149 .*

71. Theoretical Study of Chlorophyll a Hydrates Formation in Aqueous Organic Solvent. ***Ruiz-Lo´pez, Arij Ben Fredj and Manuel F.*** *2010, J. Phys. Chem. B , pp. 114, 681–687.*

72. ***A. Agostiano a, M. Caselli a, M. Delia Monica a A.J. Gotch b and F.K. Fong.*** *Polarographic studies of photocatalytic chlorophyll. Formation of chlorophyll a. Biochimica et Biophysica Acta. 1988, Vols. 936, 171-178 171.*

73. A. AGOSTIANO, K. A. BUTCHER, M. S. SHOWELL, A. J. GOTCH and F. K. FONG . ***EXCITATION, DIPOLE-DIPOLE TRANSFER BETWEEN ACETONE SOLVATES OF CHLOROPHYLL a AND CHLOROPHYLL a DIHYDRATE DIMERS IN***

WATER/ACETONE MIXTURES. A MODEL FOR P680 SENSITIZED. *1987, CHEMICAL PHYSICS LETTERS, pp. 137, 37- 41.*

74. Chlorophyll< i> a</i> auto-aggregation in water rich region. ***A Agostiano, M Della Monica, G Palazzo and M Trotta.*** *1993, Biophysical chemistry, pp. 47, 193-202.*

75. ***Maroncelli, E.W. Castner Jr. and Mark.*** *Solvent dynamics derived from optical Kerr effect, dielectric dispersion, and time-resolved stokes shift measurements: an empirical comparison. Journal of Molecular Liquids. 1998, Vol. 77, 1-36.*

76. ***E.L. Read, G.S. Engel, T.R. Calhoun, T. Mancal, T.K. Ahn, R.E. Blankenship and G.R. Flemming.*** *2007, Proc. Natl. Acad. Sci. .*

77. Excited singletstate lifetimes of hydrated chlorophyll aggregates. ***A. J. Alfano, F. E. Lytle, M. S. Showell, and F. K. Fong.*** *1985, The Journal of Chemical Physics.*

78. Excited And Ground state Vibrational dynamics Revealed by two- dimensional electronic spectroscopy. ***Justin R. Caram, Andrew F. Fidler, And Gregory S. Engel.*** *2012, The journal of chemical physics.*

79. Two-Dimensional Femtosecond Spectroscopy. ***Jonas, D. M.*** *2003, Annu. Rev. Phys. Chem.*

80. Ultrafast transient absorption spectroscopy: principles and application to photosynthetic systems. ***Rudi Berera, Rienk van Grondelle and John T. M. Kenniscorresponding.*** *2009, Photosynth Research.*

81. ***http://nobelprize.org. [Online]***

82. Molecular Dynamics Simulation Study of Chlorophyll a in Different Organic Solvents. Roccatano, K.Karki and D. 2011, JTCC, pp. 7, 1131–1140.